

The Modification of Porous Coordination Polymers or Metal- Organic Frameworks for Photocatalytic Applications

DISSERTATION

zur Erlangung des akademischen Grades eines
Doktors der Naturwissenschaften (Dr. rer. Nat.)
an der Fakultät für Biologie, Chemie und Geowissenschaften
der Universität Bayreuth

vorgelegt von

M.Sc. Dominic Tilgner

geboren in Hof

Bayreuth, 2017

Die vorliegende Arbeit wurde in der Zeit von März 2015 bis Dezember 2017 in Bayreuth am Lehrstuhl Anorganische Chemie II unter Betreuung von Herrn Professor Dr. Rhett Kempe angefertigt.

Vollständiger Abdruck der von der Fakultät für Biologie, Chemie und Geowissenschaften der Universität Bayreuth genehmigten Dissertation zur Erlangung des akademischen Grades eines Doktors der Naturwissenschaften (Dr. rer. nat.).

| | |
|---|------------|
| Dissertation eingereicht am: | 07.12.2017 |
| Zulassung durch die Promotionskommission: | 13.12.2017 |
| Wissenschaftliches Kolloquium: | 06.06.2018 |

Amtierender Dekan: Prof. Dr. Stefan Peiffer

Prüfungsausschuss:

| | |
|-----------------------------|-------------|
| Prof. Dr. Rhett Kempe | (Gutachter) |
| Prof. Dr. Jürgen Senker | (Gutachter) |
| Prof. Dr. Georg Papastavrou | (Vorsitz) |
| Prof. Dr. Matthias Breuning | |

Meiner Familie und meiner Juli in Dankbarkeit und Liebe gewidmet

Abbreviations

| | |
|--------------------|--|
| a.u. | arbitrary units |
| Cp | cyclopentadienyl |
| BET | Brunauer Emmett Teller |
| EDX | energy dispersive X-ray spectroscopy |
| FID | flame ionization detector |
| FTIR | fourier transform infrared spectroscopy |
| GC | gas chromatography |
| H ₂ BDC | benzene-1,4-dicarboxylic acid (terephthalic acid) |
| HAADF-STEM | high-angle annular dark-field scanning TEM |
| GC/MS | gas chromatography coupled with mass spectroscopy |
| HRTEM | high resolution transmission electron microscopy |
| ICP-OES | inductively coupled plasma optical emission spectrometry |
| LED | light-emitting diode |
| M@PCP/MOF | PCP/MOF supported metal |
| MIL | material of Institute Lavoisier (e.g. MIL-101) |
| MNP | metal nanoparticle |
| MOCVD | metal-organic chemical vapor deposition |
| MOF | metal-organic framework |
| NMR | nuclear magnetic resonance |
| PCP | porous coordination polymer |
| ppm | parts per million |
| rpm | rounds per minute |
| SEM | scanning electron microscopy |
| SSA | specific surface area |
| TEM | transmission electron microscopy |
| TGA | thermogravimetric analysis |
| UV | ultraviolet |
| Vis | visible |
| XPS | X-ray photoelectron spectroscopy |
| XRD | X-ray diffraction |

Table of Contents

| | |
|--|-----|
| Abbreviations..... | VII |
| 1 Summary / Zusammenfassung..... | 1 |
| 1.1 Summary..... | 1 |
| 1.2 Zusammenfassung..... | 5 |
| 2 Introduction..... | 9 |
| 3 Overview of Thesis Results..... | 19 |
| 3.1 Synopsis..... | 19 |
| 3.2 Individual Contribution to Joint Publications..... | 34 |
| 4 Titanium Dioxide Reinforced Metal-Organic Framework Pd Catalysts: Activity and Reusability Enhancement in Alcohol Dehydrogenation Reactions and Improved Photocatalytic Performance..... | 37 |
| 4.1 Introduction..... | 37 |
| 4.2 Results and Discussion..... | 38 |
| 4.3 Conclusions..... | 47 |
| 4.4 Experimental Section..... | 47 |
| 4.5 References..... | 51 |
| 4.6 Supporting Information..... | 56 |
| 5 A Plasmonic Colloidal Photocatalyst Composed of a Metal–Organic Framework Core and a Gold/Anatase Shell for Visible- Light-Driven Wastewater Purification from Antibiotics and Hydrogen Evolution..... | 71 |
| 5.1 Introduction..... | 71 |
| 5.2 Results and Discussion..... | 73 |
| 5.3 Conclusions..... | 81 |
| 5.4 Experimental Section..... | 82 |
| 5.5 References..... | 84 |
| 5.6 Supporting Information..... | 87 |
| 6 Visible Light-Driven Hydrogen Generation from Alcohols for C-N Multiple Bond Formation by a Metal-Organic Framework-Based Noble Metal-Free Photocatalyst 97 | |

| | |
|--|-----|
| 6.1 Introduction | 98 |
| 6.2 Results and Discussion | 99 |
| 6.3 Conclusions | 105 |
| 6.4 References | 106 |
| 6.5 Supporting Information | 108 |
| | |
| 7 A Metal-Organic Framework-Based Nonprecious Metal Photocatalyst for Visible Light-Driven Wastewater Treatment..... | 125 |
| 7.1 Introduction | 126 |
| 7.2 Results and Discussion | 127 |
| 7.3 Conclusions | 132 |
| 7.4 References | 132 |
| 7.5 Supporting Information | 134 |
| | |
| 8 List of Publications..... | 147 |
| | |
| 9 Acknowledgements / Danksagung | 149 |
| 9.1 Acknowledgements | 149 |
| 9.2 Danksagung | 150 |
| | |
| 10 (Eidesstattliche) Versicherungen und Erklärungen | 153 |

1 Summary / Zusammenfassung

1.1 Summary

The aim of this work was the tailored modification of porous coordination polymers (PCPs) or metal-organic frameworks (MOFs) for various catalytic applications with a focus on photocatalytic processes. The PCP/MOF MIL-101 (Cr) used was optimized regarding the catalytic activity and the reusability following a synthesis procedure developed at the Kempe group. The generation of titanium dioxide inside the pores of MIL-101 was achieved by gas phase loading with the precursor titanium(IV) isopropoxide and the subsequent decomposition to TiO₂. The remaining specific surface area of TiO₂@MIL-101 enabled the additional modification with Pd nanoparticles (Figure 1).

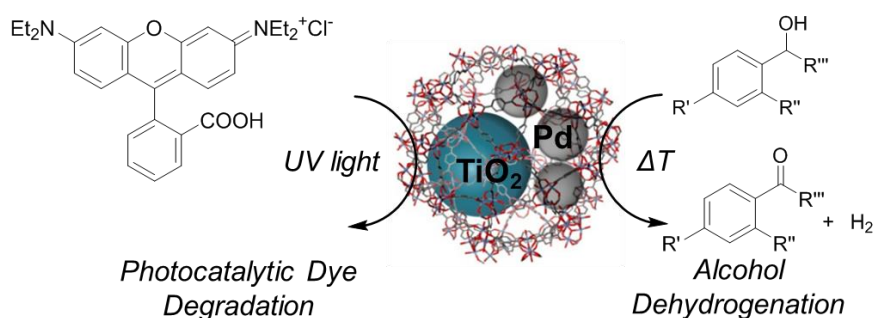


Figure 1. Schematic illustration of the Pd/TiO₂@MIL-101 catalyst with the utilization for the dehydrogenation of alcohols and the photocatalytic degradation of pollutants.

The formation of Pd and TiO₂ in the pores of the MIL-101 crystallites proved to be advantageous for two reasons. Firstly, a higher catalytic activity and an increased stability was observed in hydrogenation in dehydrogenation reactions compared to Pd@MIL-101 and commercial heterogeneous Pd catalysts. The dehydrogenation of alcohols to the corresponding carbonyl compounds liberating H₂ could be achieved under mild reaction conditions (base-free, 90 °C) and without an acceptor. Secondly, the photocatalytic activity of Pd/TiO₂@MIL-101 was significantly higher than for TiO₂@MIL-101 and MIL-101 under the illumination of UV light.

The development of PCP/MOF-based catalysts applicable in visible light-driven photocatalytic processes was realized based on the generation of crystalline TiO₂ and the subsequent modification with gold particles. The formation of crystalline TiO₂ particles

was achieved under mild hydrothermal reaction conditions at 150 °C. The TiO₂ was released from the pores forming larger particles on the surface of the MIL-101 crystallites. The multiple formation of TiO₂ inside the MIL-101 pores followed by the hydrothermal crystallization led to a homogeneous shell of TiO₂ around the MIL-101 crystallites. Plasmonic gold particles absorbing visible light were generated afterwards on the surface of the TiO₂ shell. The volatile Au precursor [Cl(Au)CO] was deposited on the TiO₂ surface through the gas phase and reduced under hydrogen atmosphere forming crystalline Au⁰ particles (Figure 2).

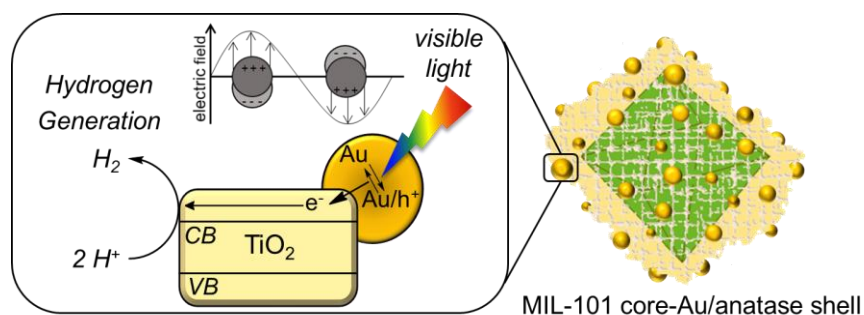


Figure 2. Schematic illustration of the MIL-101 core-Au/anatase shell photocatalyst applicable for hydrogen evolution under visible light illumination.

The generation of reactive electrons under visible light is ascribed to the plasmonic excitation of the gold particles of the MIL-101 core-Au/anatase shell material. The transfer of the electrons into the conduction band of the TiO₂ leads to an effective separation of the charge carriers (electron-hole pair). The MIL-101 core-Au/anatase shell material was investigated for the photocatalytic purification of wastewater. An increased activity was observed for the oxidative degradation of pollutants and antibiotics compared to other Au/TiO₂-based materials. The reusable core-shell photocatalyst was used additionally for the photocatalytic evolution of hydrogen from water.

The generation of photoactive semiconductor systems supported by MIL-101 was investigated in continuative studies to replace the rare and expensive noble metal gold as the light-absorbing component. The synthesis of crystalline TiO₂ around the MIL-101 crystallites represented the basis for further modifications with the semiconductor components CdS and Fe₂O₃ (Figure 3). Crystalline CdS was generated on the TiO₂ surface under solvothermal reaction conditions using cadmium acetate dihydrate as precursor. The photocatalytic activity of the CdS/TiO₂@MIL-101 material resulting

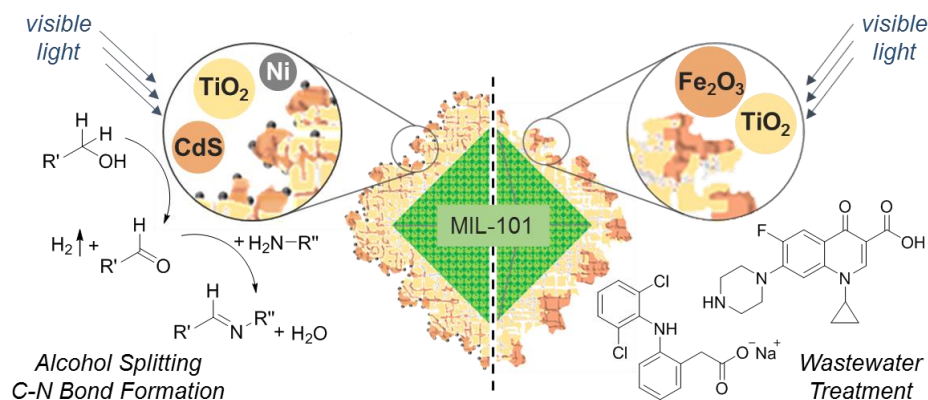


Figure 3. Schematic illustration of the Ni/CdS/TiO₂@MIL-101 photocatalyst for alcohol splitting and the consecutive synthesis of imines (left) and the Fe₂O₃/TiO₂@MIL-101 photocatalyst for the degradation of pharmaceutical substances (right).

could be increased by the final modification with nickel particles. The Ni/CdS/TiO₂@MIL-101 photocatalyst was investigated for the splitting of alcohols into the corresponding aldehydes or ketones and molecular hydrogen under visible light. The modification with Ni particles increased the photocatalytic activity significantly compared to the expensive noble metals Au, Pd, and Pt. The combination of the semiconducting materials CdS and TiO₂ and their arrangement on MIL-101 was beneficial regarding the photocatalytic activity in comparison to bare CdS and TiO₂. The synthesis of carbonyl compounds via alcohol splitting for consecutive C-N bond formation reactions is a promising strategy for the conservation of fossil carbon resources, since alcohols can be obtained from renewable biomass. The Ni/CdS/TiO₂@MIL-101 photocatalyst was used for the selective synthesis of imines from alcohols and amines in this context.

Iron and titanium are the two transition metals of the earth crust which appear most and the development of photocatalysts based on these elements represents a sustainable approach for the conservation of our metal resources. The formation of Fe₂O₃ upon the TiO₂-modified MIL-101 crystallites was investigated in this regard. The Fe precursor [Fe(CO)₅] was deposited through the gas phase and decomposed by oxygen forming iron oxide. Crystalline Fe₂O₃ particles were obtained under hydrothermal reaction conditions in analogy to the formation of TiO₂. The Fe₂O₃/TiO₂@MIL-101 material resulting was investigated for the treatment of clinical wastewater under visible light. The efficient oxidative degradation of the commercial antibiotics ciprofloxacin and levofloxacin and

the analgesic diclofenac as model substrates was achieved without further additives. The $\text{Fe}_2\text{O}_3/\text{TiO}_2@\text{MIL-101}$ catalyst additionally exhibited a higher photocatalytic activity compared to the bare metal oxides.

1.2 Zusammenfassung

Das Ziel dieser Arbeit war die anwendungsspezifische Modifizierung von porösen Koordinationspolymeren (PCPs) oder metallorganischen Gerüstverbindungen (MOFs) für diverse katalytische Anwendungen mit Fokus auf photokatalytische Prozesse. Das verwendete PCP/MOF MIL-101 (Cr) wurde hinsichtlich der katalytischen Aktivität sowie der Wiederverwendbarkeit in optimierter Kristallitgröße nach einer in der Arbeitsgruppe Kempe entwickelten Vorschrift synthetisiert. Die Generierung von Titandioxid in den Poren von MIL-101 wurde durch die kontrollierte Gasphasenbeladung mit dem Präkursor Titan(IV)isopropoxid und der anschließenden Zersetzung zu TiO_2 erreicht. Die verbliebene innere Oberfläche von TiO_2 @MIL-101 ermöglichte die weitere Modifikation mit Pd-Nanopartikeln (Abbildung 1).

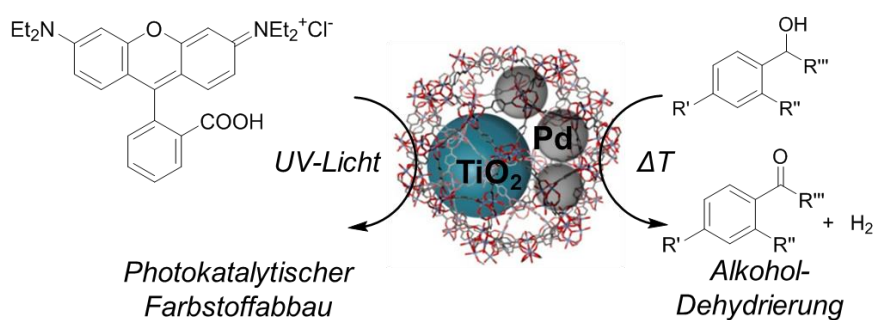


Abbildung 1. Schematische Darstellung des Pd/ TiO_2 @MIL-101 Katalysators mit Anwendung in der Dehydrierung von Alkoholen und dem photokatalytischen Abbau von Schadstoffen.

Die Generierung von Pd und TiO_2 in den Poren der MIL-101 Kristallite erwies sich in zweierlei Hinsicht als vorteilhaft. Zum Ersten konnte im Vergleich zu Pd@MIL-101 sowie kommerziellen heterogenen Pd-Katalysatoren eine höhere katalytische Aktivität sowie eine deutlich erhöhte Stabilität in Hydrierungs- und Dehydrierungsreaktionen beobachtet werden. Mit dem Pd/ TiO_2 @MIL-101 Katalysator konnten Alkohole bei milden Reaktionsbedingungen (basenfrei, 90 °C) sowie ohne Akzeptor unter Freisetzung von H_2 zu den entsprechenden Carbonylverbindungen dehydriert werden. Zum Zweiten lag die photokatalytische Aktivität von Pd/ TiO_2 @MIL-101 unter Einstrahlung von UV-Licht deutlich über der von TiO_2 @MIL-101 und MIL-101.

Basierend auf der Bildung von kristallinem TiO_2 und der nachfolgenden Modifizierung mit Goldpartikeln erfolgte die Entwicklung PCP/MOF-basierter Katalysatoren für

photokatalytische Prozesse unter sichtbarem Licht. Die Generierung von kristallinen TiO_2 -Partikeln wurde unter milden, hydrothermalen Reaktionsbedingungen bei $150\text{ }^\circ\text{C}$ erreicht. Dabei wurde das TiO_2 aus den Poren herausgelöst und bildete an der Oberfläche der MIL-101 Kristallite größere Partikel. Die mehrfache Generierung von TiO_2 in den MIL-101 Poren gefolgt von der hydrothermalen Kristallisation führte zur Bildung einer homogenen Schale aus kristallinem TiO_2 um die MIL-101 Kristallite. Auf der äußeren Oberfläche der TiO_2 -Schale wurden anschließend plasmonische Goldnanopartikel generiert, welche Licht im sichtbaren Wellenlängenbereich absorbieren. Hierfür wurde der sublimierbare Au-Präkursor $[\text{ClAu}(\text{CO})]$ über die Gasphase auf der TiO_2 -Oberfläche abgeschieden und unter Wasserstoffatmosphäre zu kristallinen Au^0 -Partikeln reduziert (Abbildung 2).

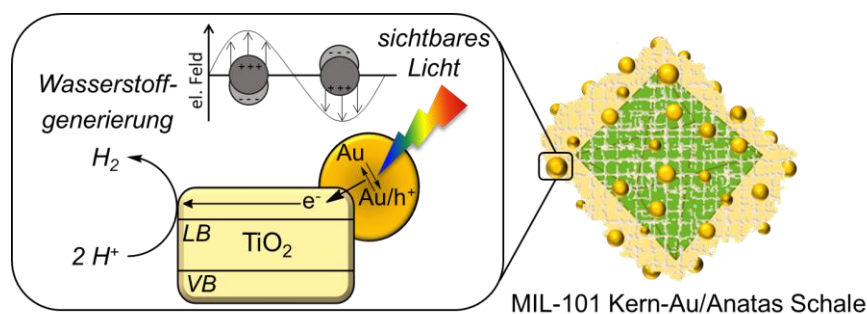


Abbildung 2. Schematische Darstellung des MIL-101 Kern–Au/Anatas Schale Photokatalysators mit Anwendung in der Generierung von Wasserstoff unter sichtbarem Licht.

Die Generierung reaktiver Elektronen unter sichtbarem Licht ist auf die plasmonische Anregung der Goldpartikel des MIL-101 Kern-Au/Anatas Schale Materials zurückzuführen. Die effektive Trennung der Ladungsträger (Elektron-Loch Paar) erfolgt durch den Übertrag der Elektronen in das Leitungsband von TiO_2 . Das MIL-101 Kern-Au/Anatas Schale Material wurde für die photokatalytische Reinigung von Abwässern unter sichtbarem Licht verwendet. Im Vergleich zu weiteren Au/ TiO_2 -basierten Materialien wurde eine höhere Aktivität für den oxidativen Abbau von Schadstoffen und Antibiotika beobachtet. Der wiederverwendbare Kern-Schale Katalysator wurde zudem für die Entwicklung von Wasserstoff durch photokatalytische Wasserspaltung untersucht.

In weiteren Arbeiten wurde die Generierung von photoaktiven Halbleitersystemen auf MIL-101 untersucht, um das seltene und teure Edelmetall Gold als lichtabsorbierende Komponente zu ersetzen. Grundlage dafür war die beschriebene Synthese von

kristallinem TiO_2 um die MIL-101 Kristallite. Als zusätzliche Halbleiterkomponenten wurden CdS und Fe_2O_3 gewählt (Abbildung 3).

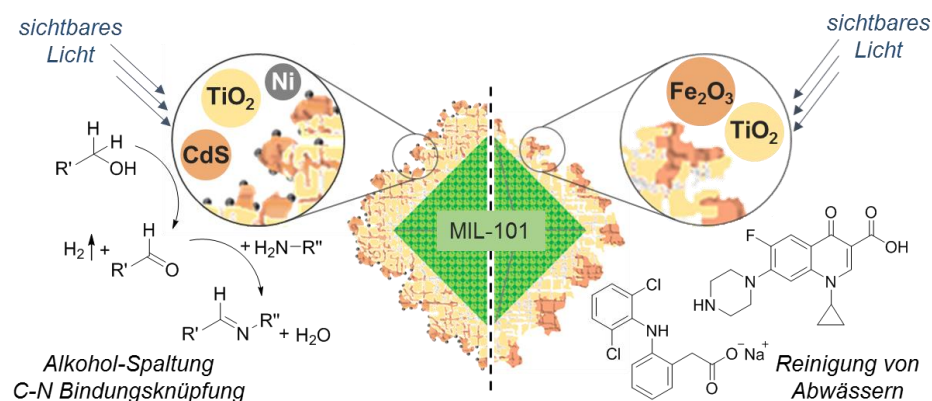


Abbildung 3. Schematische Darstellung des $\text{Ni}/\text{CdS}/\text{TiO}_2/\text{MIL-101}$ Photokatalysators für die Spaltung von Alkoholen und die konsekutive Synthese von Iminen (links) und des $\text{Fe}_2\text{O}_3/\text{TiO}_2/\text{MIL-101}$ Photokatalysators für den Abbau pharmazeutischer Wirkstoffe (rechts).

Kristallines CdS wurde unter solvothermalen Reaktionsbedingungen ausgehend von Cadmiumacetat Dihydrat auf der TiO_2 Oberfläche generiert. Die photokatalytische Aktivität des resultierenden $\text{CdS}/\text{TiO}_2/\text{MIL-101}$ Materials konnte durch die finale Modifizierung mit Nickelpartikeln deutlich erhöht werden. Der $\text{Ni}/\text{CdS}/\text{TiO}_2/\text{MIL-101}$ Photokatalysator wurde für die Spaltung von Alkoholen zu den jeweiligen Aldehyden oder Ketonen sowie molekularem Wasserstoff unter sichtbarem Licht untersucht. Die Modifikation mit Ni-Partikeln führte im Vergleich zu den teuren Edelmetallen Au , Pd und Pt zu der größten Aktivitätssteigerung. Die Kombination der halbleitenden Materialien CdS und TiO_2 sowie deren Trägerung auf MIL-101 beeinflusste die photokatalytische Aktivität im Vergleich zu reinem CdS und TiO_2 zudem positiv. Die Synthese von Carbonylverbindungen durch Alkohol-Spaltung stellt für die weiterführende Bildung von C-N Bindungen eine vielversprechende Möglichkeit dar, um fossile Kohlenstoffvorräte zu schonen, da Alkohole aus nachwachsender Biomasse erhalten werden können. In diesem Zusammenhang wurde der $\text{Ni}/\text{CdS}/\text{TiO}_2/\text{MIL-101}$ Photokatalysator für die selektive Synthese von Iminen ausgehend von Alkoholen und Aminen eingesetzt.

Die Entwicklung von Photokatalysatoren basierend auf den Elementen Fe und Ti stellt einen besonders ressourcenschonenden Ansatz dar, da es sich hierbei um die Übergangsmetalle mit dem größten Vorkommen in der Erdkruste handelt. In diesem

Kontext wurde die Generierung von Fe₂O₃ auf den mit TiO₂ modifizierten MIL-101 Kristalliten untersucht. Der Fe-Präkursor [Fe(CO)₅] wurde über die Gasphase abgeschieden und durch Sauerstoff zum Oxid zersetzt. Kristalline Fe₂O₃-Partikel wurden analog zur Bildung der TiO₂-Partikel unter hydrothermalen Reaktionsbedingungen erhalten. Das resultierende Fe₂O₃/TiO₂@MIL-101 Material wurde für die Behandlung von klinischen Abwässern unter sichtbarem Licht untersucht. Der effiziente oxidative Abbau der kommerziellen Antibiotika Ciprofloxacin und Levofloxacin sowie des Schmerzmittels Diclofenac als Modellsubstrate wurde ohne die Zugabe weiterer Additive erreicht. Zudem wurde im Vergleich zu den reinen Metalloxiden eine erhöhte photokatalytische Aktivität durch die Trägerung von Fe₂O₃ und TiO₂ auf MIL-101 beobachtet.

2 Introduction

Porous coordination polymers (PCPs)^[1] or metal-organic frameworks (MOFs)^[2] are highly porous crystalline materials built up of inorganic building units (metal ions/metal ion clusters generally designated as secondary building units (SBUs)) connected by multidentate organic linkers. The structural diversity resulting from the variation of the linkers or the metal centers lead to a permanently increasing number of PCP/MOFs.^[3] The purposive design of PCP/MOFs in combination with the high specific surface areas, the well-defined pore geometries, and the versatile modifiability resulted in a wide range of applications including gas storage and separation, drug delivery, bioimaging, sensing, and catalysis.^[4] The use in heterogeneous catalysis was one of the earliest applications demonstrated for PCP/MOFs.^[5] Active reaction sites of the PCP/MOF catalysts can be located at the linking organic molecules incorporating functional groups or at the central metal ion clusters. Another effective strategy for the generation of active reaction sites is the modification of the PCP/MOFs with catalytically active metal complexes or metal nanoparticles (MNP).^[6] The generation of MNP@PCP/MOF materials can be achieved following two different strategies (Figure 1).

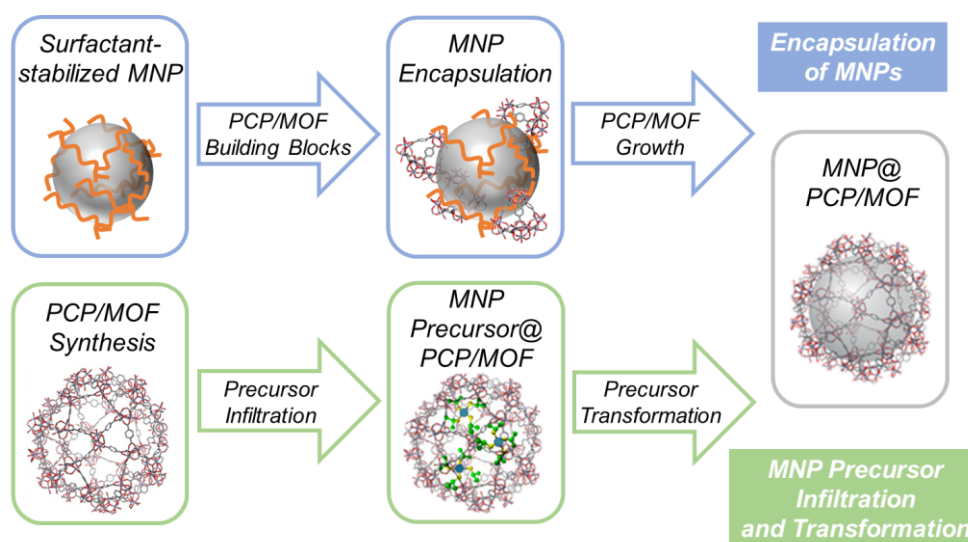


Figure 1. Schematic illustration of the two different synthesis strategies for the generation of MNP@PCP/MOF materials.

The first strategy describes the encapsulation of pre-synthesized MNPs in a PCP/MOF by the addition of the MNPs to into a synthetic solution containing the molecular building

blocks of the PCP/MOF. The size and the morphology of the MNPs is not limited by the pore geometry of the PCP/MOF enabling the encapsulation of individually shaped MNPs. To avoid the agglomeration of the MNPs, they need to be capped by stabilizing agents, which also promotes the connection to the PCP/MOF building blocks.^[7] The encapsulation of MNPs is restricted to a comparably small number of PCP/MOFs and a homogeneous particle distribution inside the framework is hard to obtain. The complete synthesis of the PCP/MOFs before the modification with MNPs is required regarding the second synthesis strategy. Afterwards, precursor compounds of the MNPs are infiltrated into the PCP/MOF structure followed by the transformation of the precursor to the MNP desired. The uptake of the precursors is facilitated strongly by the unique adsorption properties and the large specific surface areas of the PCP/MOFs.^[8] Many processes are known for the precursor infiltration including solution infiltration, solid grinding, microwave irradiation, surface grafting, and the chemical vapor deposition of metal-organic compounds (MOCVD).^[9] The solvent-free infiltration of volatile precursors through the gas phase developed by Fischer and co-workers offers high metal loadings up to 50 wt% in combination with a uniform particle distribution and a good reaction control.^[10] The synthesis of various elemental nanoparticles including Au, Cu, Fe, Ir, Mg, Ni, Pd, Pt, and Ru is described in the literature following the MOCVD technique. In addition to the generation of monometallic MNPs, the MOCVD procedure represents an elegant method for the formation of bimetallic MNPs in the frameworks of PCP/MOFs. The quantitative composition of the bimetallic MNPs can be adjusted precisely by the amounts of the metal precursors. The combination of two metals in the confined space of the PCP/MOF structure is described to be beneficial for catalytic applications because of synergistic effects.^[11] The modification of PCP/MOFs with mono- or bimetallic MNPs using the MOCVD procedure is well-established at the Kempe group and the hybrid materials resulting were investigated for hydrogen storage and liquid-phase catalysis.^[10b,12] Beside the modification with mono- or bimetallic MNPs described, PCP/MOFs are suitable support materials for metal oxides, quantum dot materials, biomolecules, ionic liquids, polymers, dyes, carbon materials, or polyoxometalates.^[13] Regarding the support of metal oxide particles, the synthesis of TiO₂@PCP/MOF materials represents a promising approach for the generation and the stabilization of well-defined TiO₂ particles. The generation of TiO₂ in a PCP/MOF was described first by the gas phase infiltration of titanium(IV) isopropoxide into MOF-5.^[14] Based on these results,

other examples of TiO₂@PCP/MOF materials were reported for photocatalytic processes among other applications.^[15]

While TiO₂ is a semiconducting material widely investigated for various photocatalytic applications in environmental and energy-related fields,^[16] the use of PCP/MOFs for the generation of photocatalysts is a relatively young field of research. Solar energy is proposed as a sustainable alternative energy source for human consumption regarding the increasing global energy demand and the limited availability of fossil fuel supplies. The general principle for the conversion of light into chemical energy in heterogeneous semiconductor photocatalysis can be described as follows: the absorption of light by the semiconducting material results in the photoexcitation of the charge carriers, if the absorbed photon energy (E_{ph}) equals or exceeds the band gap energy (E_g) of the semiconductor. Electrons are transferred from the valence band (VB) into the conduction band (CB), which leads to the separation of the charge carriers forming electron-hole pairs (e^-h^+). The separation of the charge carriers via the migration to the semiconductor surface offers chemical transformations in oxidation and reduction reactions (Figure 2).^[17]

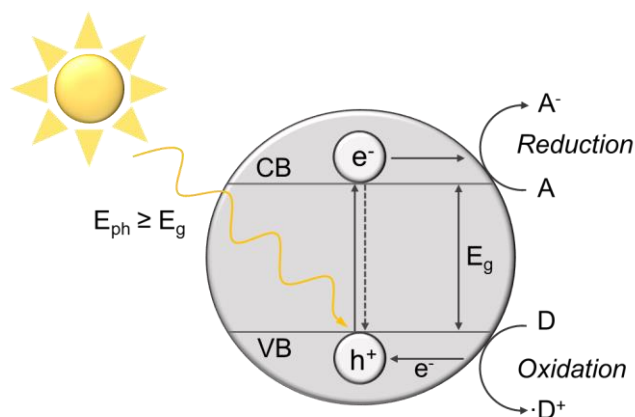


Figure 2. Basic process of light-induced charge carrier generation in semiconductor materials for photocatalytic reactions.

The recombination of the charge carriers reduces the photocatalytic efficiency significantly. The recombination of electrons and holes can occur directly after the excitation, at grain boundaries, and because of defects in the crystal structure of the semiconductor material.^[18] Several strategies have been developed to suppress the recombination of the charge carriers and to increase the efficiency of semiconductor

photocatalysts. Scavenger molecules (sacrificial molecules) are used to remove either the electrons or the holes increasing the efficiency for one half reaction of the system. The morphology of the photocatalyst has a strong influence on the photocatalytic activity. Consequently, various attempts have been reported to shorten the diffusion pathways of the charge carriers modifying the semiconductor morphology or crystallinity. The strategy most promising for the efficient separation of electrons and holes is the generation of composite materials via the modification of the semiconductor with MNPs or additional semiconducting materials to generate heterojunction systems.^[19]

In this context, PCP/MOFs provide a promising platform for the generation of photocatalysts applicable for the conversion of solar energy into chemical energy due to the highly crystalline structure and the specific modifiability. Several PCP/MOFs have been reported to show photocatalytic activity. The energy transfer can be explained by localized linker-to-metal charge transfers, metal-to-linker charge transfers, or $\pi\text{-}\pi^*$ transitions of aromatic linkers.^[20] The modification of PCP/MOFs with organic or metal-organic photosensitizers as well as photoactive nanostructures is used to improve the activity under light illumination or to generate photoactive systems using the PCP/MOFs as co-catalysts or as porous support materials (Figure 3).^[21]

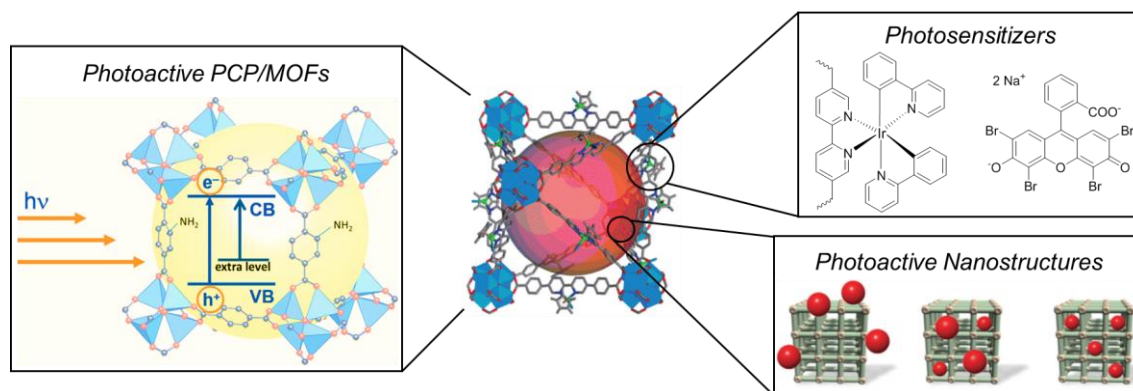


Figure 3. PCP/MOFs built up of suitable combinations of SBUs and linkers are described to be applicable in photocatalytic processes. The modification of PCP/MOFs with appropriate photosensitizers or photoactive nanostructures can be used to increase the photocatalytic activity or to generate PCP/MOF-supported photocatalysts.^[21]

The PCP/MOF composite materials resulting from the versatile possibilities of construction offer the application in several photocatalytic processes. Herein, the photocatalytic reduction of water was investigated intensively to generate H_2 , which is

regarded as a hopeful way to convert and store solar energy in a sustainable energy carrier. Beside the H₂ generation performed by PCP/MOFs composed of the metals Cr, Cu, Ti, or Zr, modified hybrid materials comprised of PCP/MOFs and photosensitizers or MNPs were investigated intensively for the manipulation of the light absorption behavior or to increase the H₂ generation.^[22] The other half reaction of water splitting, the evolution of O₂ by the oxidation of water, was also investigated employing PCP/MOF-based materials.^[23] The conversion of CO₂ into valuable chemicals by solar energy is a promising method for the reduction of the green-house effect. PCP/MOFs materials have been studied extensively for CO₂ adsorption and capture^[24] and showed great potential for the photocatalytic conversion of CO₂ also.^[25] Another application of PCP/MOF photocatalysts in environmental science is the oxidative decomposition of organic pollutants for light-driven wastewater treatment.^[26] Finally, the utilization of PCP/MOF-based photocatalysts in photooxidation or -reduction reactions is of great importance regarding the development of sustainable concepts for organic synthesis.^[27] Herein, the activation of alcohols is an environmentally friendly approach for the subsequent synthesis of fine chemicals, because alcohols can be obtained from lignocellulose, an indigestible biomass abundantly available.^[28] The splitting of alcohols without acceptor molecules leads to reactive carbonyl compounds and the likewise generation of H₂, an important energy carrier.^[29] The use of photocatalysts for alcohol splitting represents an interesting strategy for the sustainable generation of H₂ and the activation of alcohols for subsequent condensation reactions. Few examples are presented in the literature for the visible light-driven splitting of alcohols under water- and acceptor-free reaction conditions. Ruberu *et al.* described the splitting of benzyl alcohol using CdS_xSe_y modified with Pd or Pt nanoparticles.^[30] The photocatalytic splitting of benzyl alcohol was reported also by Mitkina *et al.* in limited selectivity using CdS.^[31] The modification of CdS with Ni particles to enhance the photocatalytic activity for alcohol splitting was reported by Xu and co-workers.^[32] Some reports additionally describe the visible-light driven splitting of alcohols in aqueous media using additives.^[33] The development of photocatalysts for alcohol splitting under visible light and water-free conditions represents a highly desirable strategy for the selective synthesis of fine chemicals via further condensation steps of the carbonyl compounds forming C-N or C-C bonds.

References

- [1] a) B. F. Hoskins, R. Robson, *J. Am. Chem. Soc.* **1989**, *111*, 5962–5964; b) B. F. Abrahams, B. F. Hoskins, D. M. Michail, R. Robson, *Nature* **1994**, *369*, 727–729.
- [2] a) O. M. Yaghi, H. Li, *J. Am. Chem. Soc.* **1995**, *117*, 10401–10402; b) H. Li, M. Eddaoudi, M. O’Keeffe, O. M. Yaghi, *Nature* **1999**, *402*, 276–279.
- [3] a) H. Furukawa, K. E. Cordova, M. O’Keeffe, O. M. Yaghi, *Science* **2013**, *341*, 1230444; b) W. Lu, Z. Wei, Z.-Y. Gu, T.-F. Liu, J. Park, J. Park, J. Tian, M. Zhang, Q. Zhang, T. Gentle Iii, M. Bosch, H.-C. Zhou, *Chem. Soc. Rev.* **2014**, *43*, 5561–5593.
- [4] a) J. Liu, L. Chen, H. Cui, J. Zhang, L. Zhang, C.-Y. Su, *Chem. Soc. Rev.* **2014**, *43*, 6011–6061; b) L. E. Kreno, K. Leong, O. K. Farha, M. Allendorf, R. P. Van Duyne, J. T. Hupp, *Chem. Rev.* **2012**, *112*, 1105–1125; c) J.-R. Li, R. J. Kuppler, H.-C. Zhou, *Chem. Soc. Rev.* **2009**, *38*, 1477–1504; d) A. Morozan, F. Jaouen, *Energy Environ. Sci.* **2012**, *5*, 9269–9290; e) P. Horcajada, R. Gref, T. Baati, P. K. Allan, G. Maurin, P. Couvreur, G. Férey, R. E. Morris, C. Serre, *Chem. Rev.* **2012**, *112*, 1232–1268.
- [5] M. Fujita, Y. J. Kwon, S. Washizu, K. Ogura, *J. Am. Chem. Soc.* **1994**, *116*, 1151–1152.
- [6] a) Y.-B. Huang, J. Liang, X.-S. Wang, R. Cao, *Chem. Soc. Rev.* **2017**, *46*, 126–157; b) Q. Yang, Q. Xu, H.-L. Jiang, *Chem. Soc. Rev.* **2017**, *46*, 4774–4808.
- [7] G. Lu, S. Li, Z. Guo, O. K. Farha, B. G. Hauser, X. Qi, Y. Wang, X. Wang, S. Han, X. Liu, J. S. DuChene, H. Zhang, Q. Zhang, X. Chen, J. Ma, S. C. J. Loo, W. D. Wei, Y. Yang, J. T. Hupp, F. Huo, *Nature Chem.* **2012**, *4*, 310–316.
- [8] J.-R. Li, J. Sculley, H.-C. Zhou, *Chem. Rev.* **2012**, *112*, 869–932.
- [9] H. R. Moon, D.-W. Lim, M. P. Suh, *Chem. Soc. Rev.* **2013**, *42*, 1807–1824.
- [10] a) S. Hermes, M.-K. Schröter, R. Schmid, L. Khodeir, M. Muhler, A. Tissler, R. W. Fischer, R. A. Fischer, *Angew. Chem. Int. Ed.* **2005**, *44*, 6237–6241; b) J. Hermannsdörfer, R. Kempe, *Chem. Eur. J.* **2011**, *17*, 8071–8077.
- [11] C. Rösler, R. A. Fischer, *CrystEngComm* **2015**, *17*, 199–217.
- [12] a) S. Proch, J. Hermannsdörfer, R. Kempe, C. Kern, A. Jess, L. Seyfarth, J. Senker, *Chem. Eur. J.* **2008**, *14*, 8204–8212; b) J. Hermannsdörfer, M. Friedrich, N. Miyajima, R. Q. Albuquerque, S. Kümmel, R. Kempe, *Angew. Chem. Int. Ed.*

- 2012**, *51*, 11473–11477; c) J. Hermannsdörfer, M. Friedrich, R. Kempe, *Chem. Eur. J.* **2013**, *19*, 13652–13657.
- [13] L. Chen, R. Luque, Y. Li, *Chem. Soc. Rev.* **2017**, *46*, 4614–4630.
- [14] M. Müller, X. Zhang, Y. Wang, R. A. Fischer, *Chem. Commun.* **2009**, 119–121.
- [15] a) M. Müller, S. Turner, O. I. Lebedev, Y. Wang, G. van Tendeloo, R. A. Fischer, *Eur. J. Inorg. Chem.* **2011**, *2011*, 1876–1887; b) Y. Hu, Z. Huang, L. Zhou, D. Wang, G. Li, *J. Sep. Sci.* **2014**, *37*, 1482–1488; c) C. R. Kim, T. Uemura, S. Kitagawa, *Microporous Mesoporous Mater.* **2014**, *195*, 31–35; d) S. Abedi, A. Morsali, *ACS Catal.* **2014**, *4*, 1398–1403; e) R. Li, J. Hu, M. Deng, H. Wang, X. Wang, Y. Hu, H.-L. Jiang, J. Jiang, Q. Zhang, Y. Xie, Y. Xiong, *Adv. Mater.* **2014**, *26*, 4783–4788; f) N. Chang, D.-Y. He, Y.-X. Li, Z.-W. Tang, Y.-F. Huang, *RSC Adv.* **2016**, *6*, 71481–71484; g) X. Li, Y. Pi, Q. Xia, Z. Li, J. Xiao, *Appl. Catal. B: Environ.* **2016**, *191*, 192–201; h) P. C. Lemaire, D. T. Lee, J. Zhao, G. N. Parsons, *ACS Appl. Mater. Interfaces* **2017**, *9*, 22042–22054; i) X. Li, Y. Mao, K. Leng, G. Ye, Y. Sun, W. Xu, *Microporous Mesoporous Mater.* **2017**, *254*, 114–120; j) J. Huang, H. Song, C. Chen, Y. Yang, N. Xu, X. Ji, C. Li, J.-A. You, *J. Environ. Chem. Eng.* **2017**, *5*, 2579–2585; k) A. Crake, K. C. Christoforidis, A. Kafizas, S. Zafeiratos, C. Petit, *Appl. Catal. B: Environ.* **2017**, *210*, 131–140.
- [16] a) H. Chen, C. E. Nanayakkara, V. H. Grassian, *Chem. Rev.* **2012**, *112*, 5919–5948; b) J. Schneider, M. Matsuoka, M. Takeuchi, J. Zhang, Y. Horiuchi, M. Anpo, D. W. Bahnemann, *Chem. Rev.* **2014**, *114*, 9919–9986.
- [17] a) J. C. Colmenares, R. Luque, *Chem. Soc. Rev.* **2014**, *43*, 765–778; b) J. Low, J. Yu, M. Jaroniec, S. Wageh, A. A. Al-Ghamdi, *Adv. Mater.* **2017**, *29*, 1601694.
- [18] R. Marschall, *Adv. Funct. Mater.* **2014**, *24*, 2421–2440.
- [19] S. J. A. Moniz, S. A. Shevlin, D. J. Martin, Z.-X. Guo, J. Tang, *Energy Environ. Sci.* **2015**, *8*, 731–759.
- [20] T. Zhang, W. Lin, *Chem. Soc. Rev.* **2014**, *43*, 5982–5993.
- [21] a) K. Meyer, M. Ranocchiari, J. A. van Bokhoven, *Energy Environ. Sci.* **2015**, *8*, 1923–1937; b) C. R. Kim, T. Uemura, S. Kitagawa, *Chem. Soc. Rev.* **2016**, *45*, 3828–3845; c) A. Dhakshinamoorthy, A. M. Asiri, H. García, *Angew. Chem. Int. Ed.* **2016**, *55*, 5414–5445.
- [22] a) C. Gomes Silva, I. Luz, F. X. Llabrés i Xamena, A. Corma, H. García, *Chem. Eur. J.* **2010**, *16*, 11133–11138; b) C. Wang, K. E. deKrafft, W. Lin, *J. Am. Chem.*

- Soc.* **2012**, *134*, 7211–7214; c) Y. Horiuchi, T. Toyao, M. Saito, K. Mochizuki, M. Iwata, H. Higashimura, M. Anpo, M. Matsuoka, *J. Phys. Chem. C* **2012**, *116*, 20848–20853; d) M. Wen, K. Mori, T. Kamegawa, H. Yamashita, *Chem. Commun.* **2014**, *50*, 11645–11648; e) R. Lin, L. Shen, Z. Ren, W. Wu, Y. Tan, H. Fu, J. Zhang, L. Wu, *Chem. Commun.* **2014**, *50*, 8533–8535; f) J. He, J. Wang, Y. Chen, J. Zhang, D. Duan, Y. Wang, Z. Yan, *Chem. Commun.* **2014**, *50*, 7063–7066; g) M. A. Nasalevich, R. Becker, E. V. Ramos-Fernandez, S. Castellanos, S. L. Veber, M. V. Fedin, F. Kapteijn, J. N. H. Reek, J. I. van der Vlugt, J. Gascon, *Energy Environ. Sci.* **2015**, *8*, 364–375.
- [23] a) C. Wang, Z. Xie, K. E. deKrafft, W. Lin, *J. Am. Chem. Soc.* **2011**, *133*, 13445–13454; b) C. Wang, J.-L. Wang, W. Lin, *J. Am. Chem. Soc.* **2012**, *134*, 19895–19908; c) B. Nepal, S. Das, *Angew. Chem. Int. Ed.* **2013**, *52*, 7224–7227.
- [24] K. Sumida, D. L. Rogow, J. A. Mason, T. M. McDonald, E. D. Bloch, Z. R. Herm, T.-H. Bae, J. R. Long, *Chem. Rev.* **2012**, *112*, 724–781.
- [25] a) Y. Fu, D. Sun, Y. Chen, R. Huang, Z. Ding, X. Fu, Z. Li, *Angew. Chem. Int. Ed.* **2012**, *51*, 3364–3367; b) D. Wang, R. Huang, W. Liu, D. Sun, Z. Li, *ACS Catal.* **2014**, *4*, 4254–4260; c) H. Fei, M. D. Sampson, Y. Lee, C. P. Kubiak, S. M. Cohen, *Inorg. Chem.* **2015**, *54*, 6821–6828.
- [26] a) F. Wang, Z.-S. Liu, H. Yang, Y.-X. Tan, J. Zhang, *Angew. Chem. Int. Ed.* **2011**, *50*, 450–453; b) X. Zhao, S. Liu, Z. Tang, H. Niu, Y. Cai, W. Meng, F. Wu, J. P. Giesy, *Sci. Rep.* **2015**, *5*, 11849; c) L. Qin, Z. Li, Z. Xu, X. Guo, G. Zhang, *Appl. Catal. B: Environ.* **2015**, *179*, 500–508; d) Y. Zhao, Y. Dong, F. Lu, C. Ju, L. Liu, J. Zhang, B. Zhang, Y. Feng, *J. Mater. Chem. A* **2017**, *5*, 15380–15389.
- [27] a) M.-H. Xie, X.-L. Yang, C. Zou, C.-D. Wu, *Inorg. Chem.* **2011**, *50*, 5318–5320; b) P. Wu, C. He, J. Wang, X. Peng, X. Li, Y. An, C. Duan, *J. Am. Chem. Soc.* **2012**, *134*, 14991–14999; c) L. Shen, S. Liang, W. Wu, R. Liang, L. Wu, *J. Mater. Chem. A* **2013**, *1*, 11473–11482; d) T. Toyao, M. Saito, Y. Horiuchi, K. Mochizuki, M. Iwata, H. Higashimura, M. Matsuoka, *Catal. Sci. Technol.* **2013**, *3*, 2092–2097.
- [28] a) T. P. Vispute, H. Zhang, A. Sanna, R. Xiao, G. W. Huber, *Science* **2010**, *330*, 1222; b) C. O. Tuck, E. Pérez, I. T. Horváth, R. A. Sheldon, M. Poliakoff, *Science* **2012**, *337*, 695.
- [29] C. Gunanathan, D. Milstein, *Science* **2013**, *341*.

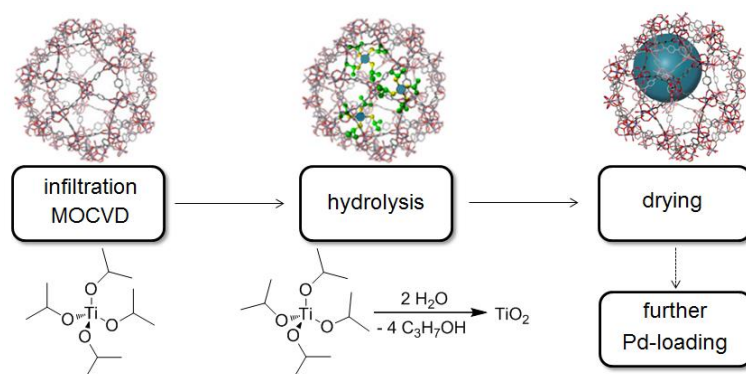
- [30] T. P. A. Ruberu, N. C. Nelson, I. I. Slowing, J. Vela, *J. Phys. Chem. Lett.* **2012**, *3*, 2798–2802.
- [31] T. Mitkina, C. Stanglmair, W. Setzer, M. Gruber, H. Kisch, B. König, *Org. Biomol. Chem.* **2012**, *10*, 3556–3561.
- [32] Z. Chai, T.-T. Zeng, Q. Li, L.-Q. Lu, W.-J. Xiao, D. Xu, *J. Am. Chem. Soc.* **2016**, *138*, 10128–10131.
- [33] a) W. Zhai, S. Xue, A. Zhu, Y. Luo, Y. Tian, *ChemCatChem* **2011**, *3*, 127–130; b) S. Higashimoto, Y. Tanaka, R. Ishikawa, S. Hasegawa, M. Azuma, H. Ohue, Y. Sakata, *Catal. Sci. Technol.* **2013**, *3*, 400–403; c) Z. Liu, J. Caner, A. Kudo, H. Naka, S. Saito, *Chem. Eur. J.* **2013**, *19*, 9452–9456; d) A. Tanaka, S. Sakaguchi, K. Hashimoto, H. Kominami, *ACS Catal.* **2013**, *3*, 79–85; e) H. Kasap, C. A. Caputo, B. C. M. Martindale, R. Godin, V. W.-h. Lau, B. V. Lotsch, J. R. Durrant, E. Reisner, *J. Am. Chem. Soc.* **2016**, *138*, 9183–9192; f) L. M. Zhao, Q. Y. Meng, X. B. Fan, C. Ye, X. B. Li, B. Chen, V. Ramamurthy, C. H. Tung, L. Z. Wu, *Angew. Chem. Int. Ed.* **2017**, *56*, 3020–3024; g) G. Han, Y.-H. Jin, R. A. Burgess, N. E. Dickenson, X.-M. Cao, Y. Sun, *J. Am. Chem. Soc.* **2017**, *139*, 15584–15587.

3 Overview of Thesis Results

The thesis consists of four publications, which are presented in the chapters 4 to 7. The topics of the publications and their correlation is summarized in chapter 3.1. The individual contributions to joint publications are specified in chapter 3.2.

3.1 Synopsis

Since the discovery of PCP/MOFs more than 20 years ago, this versatile class of highly porous materials has been used for the generation of heterogeneous catalysts via the stabilization of diverse MNPs among many other interesting applications. In this context, the Kempe group contributed to the development of novel catalysts based on the modification of selected PCP/MOFs with several MNPs employing gas phase loading procedures. The resulting M@PCP/MOF materials were proven to be suitable catalysts for the oxidation of alcohols or the reduction of ketones. However, the application of these materials at temperatures $> 100\text{ }^{\circ}\text{C}$ was limited due to the low thermal stability. Herein, the first work of this thesis focused on synthesis strategies to improve the overall stability of the M@PCP/MOF materials in catalysis. The additional incorporation of a thermally and chemically robust metal oxide seemed to be a promising approach for the stabilization of the PCP/MOF network. The generation of TiO_2 inside the cavities of the PCP/MOF MIL-101 was investigated in order to increase the stability of the established Pd@MIL-101 system and is described in chapter four. MIL-101 is stable to water and air and it can be synthesized in small crystallite sizes, which was optimized at the Kempe group regarding the catalytic performance. The solvent-free loading of MIL-101 with TiO_2 was adopted from the formation of elemental MNPs using the volatile TiO_2 precursor titanium(IV) isopropoxide $[\text{Ti}(\text{O}i\text{Pr})_4]$. The precursor was decomposed to TiO_2 and 2-propanol under water atmosphere after the infiltration (Scheme 1). The resulting TiO_2 @MIL-101 material was further modified with Pd particles using $[(\eta^5\text{-C}_5\text{H}_5)\text{Pd}(\eta^3\text{-C}_3\text{H}_5)]$ as precursor. The MOCVD procedure enables the controlled infiltration of metal or metal oxide precursors in well-defined amounts. The loading of MIL-101 with Ti contents $> 30\text{ wt}\%$ resulted in the formation of undefined TiO_2 agglomerates outside the MIL-101 crystallites. Lower Ti contents between 15 and



Scheme 1. Preparation of TiO₂@MIL-101. The Ti-precursor [Ti(OiPr)₄] was infiltrated into MIL-101 by MOCVD infiltration procedures and decomposed to titania under water atmosphere. The dry TiO₂@MIL-101 material enabled further metal loading with Pd.

20 wt% were appropriate to ensure the homogeneous distribution of TiO₂ and Pd inside the MIL-101 crystallites. X-ray powder diffraction (XRD) analysis of the TiO₂@MIL-101 material supported the integrity of MIL-101 after the incorporation of TiO₂. No peaks were found at the calculated reflex positions for crystalline TiO₂, which can be attributed to a small particle size or the formation of amorphous TiO₂. The modification of TiO₂@MIL-101 with palladium led to Pd/TiO₂@MIL-101 and regularly arranged Pd particles with a mean diameter of 2.2 nm and a narrow particle-size distribution. Cubic Pd was observed based on the distance of 0.224 nm between adjacent lattice planes of the particles (Figure 1).

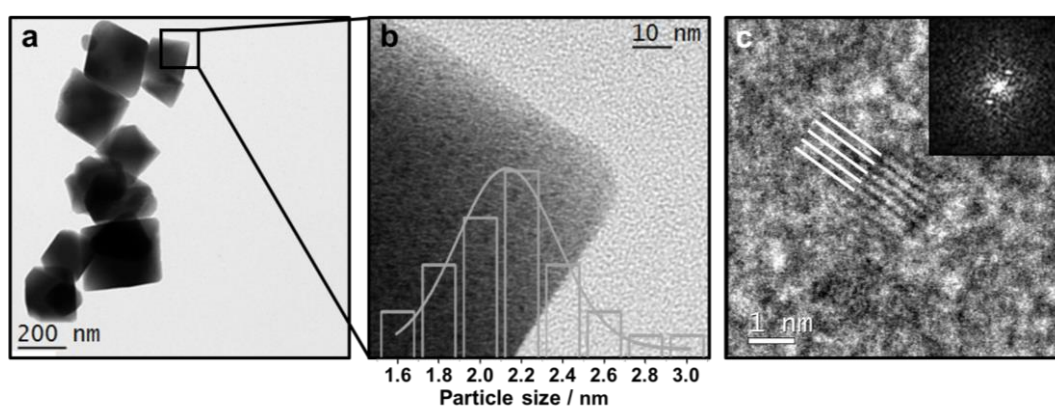


Figure 1. a) Transmission electron microscopy (TEM) images of Pd/TiO₂@MIL-101 (10 wt% Pd, 20 wt% Ti) confirm the integrity of the metal-organic host system and the absence of larger titanium dioxide aggregates outside the MIL-101 crystallites. b) The highly controlled Pd loading of TiO₂@MIL-101 enabled narrow Pd NP size distributions. c) Characteristic Pd lattice planes marked by white lines. The inset shows the diffractogram.

After the implementation of the synthesis protocol for Pd/TiO₂@MIL-101, the catalytic performance of the material was investigated for hydrogenation and dehydrogenation reactions with a specific attention regarding the activity and the reusability at reaction temperatures above 100 °C. The reduction of benzophenone under H₂ atmosphere was performed at 140 °C for five successive runs without a significant loss of activity for the TiO₂-stabilized materials with different TiO₂ contents. The catalytic activity of Pd@MIL-101 decreased continuously in contrast (Figure 2a).

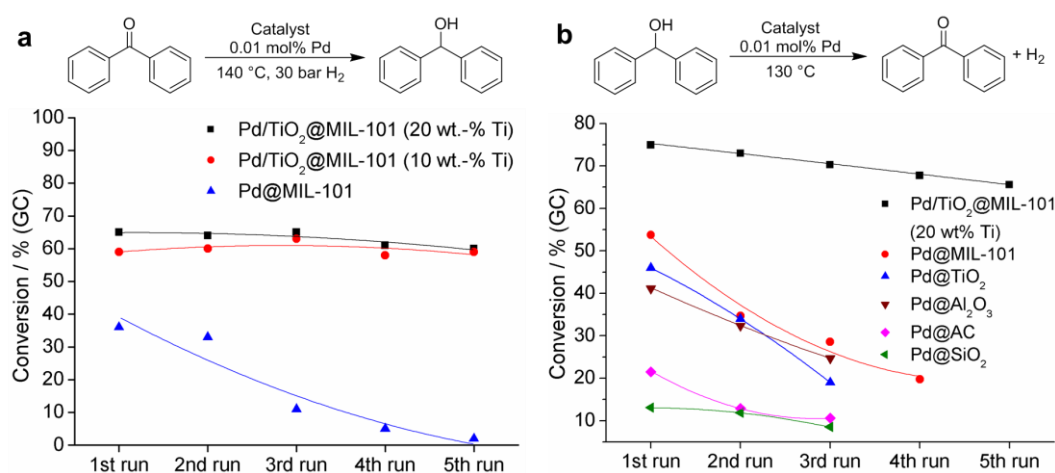


Figure 2. a) Reduction of benzophenone and b) oxidation of diphenylmethanol with a superior activity and reusability of Pd/TiO₂@MIL-101 in comparison to Pd@MIL-101 and other commercial Pd catalysts.

The Pd/TiO₂@MIL-101 material was compared additionally to Pd@MIL-101 and to commercially available Pd catalysts for the dehydrogenation of diphenylmethanol at 130 °C. Again, a superior reusability and a higher activity were observed for Pd/TiO₂@MIL-101 (Figure 2b). The structural integrity of the catalyst reused was verified by XRD analysis. The good catalytic activity of Pd/TiO₂@MIL-101 provoked the investigation of the acceptorless dehydrogenation of alcohols at lower temperatures (90 °C), which has been observed for homogeneous catalysts mainly. Diverse functional substituents were well tolerated observing excellent yields (Figure 3a). Finally, the photocatalytic properties of the Pd/TiO₂@MIL-101 material were investigated due to the utilization of the semiconducting metal oxide TiO₂ for the stabilization of the M@PCP/MOF catalysts. TiO₂ is used widely for various photocatalytic applications and the incorporation in MIL-101 or Pd@MIL-101 also resulted in an increased activity for

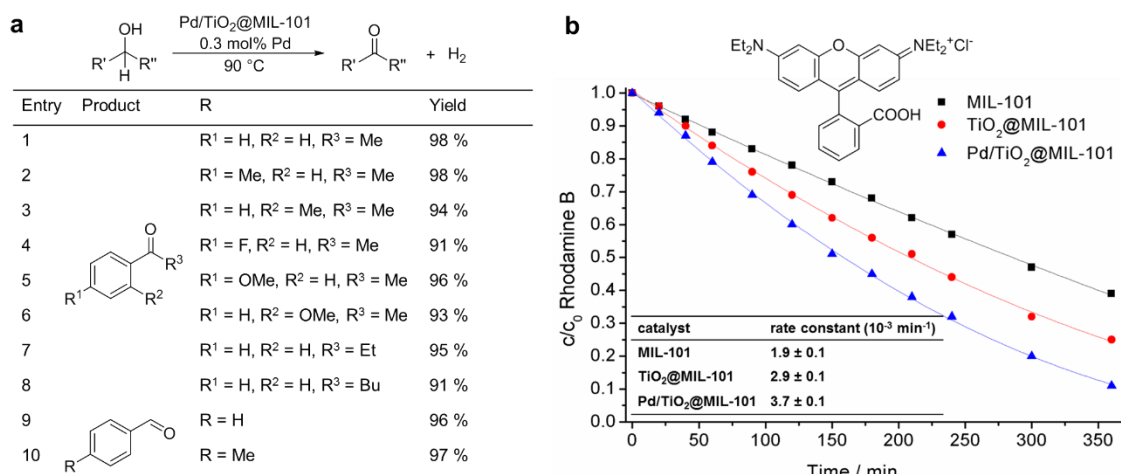
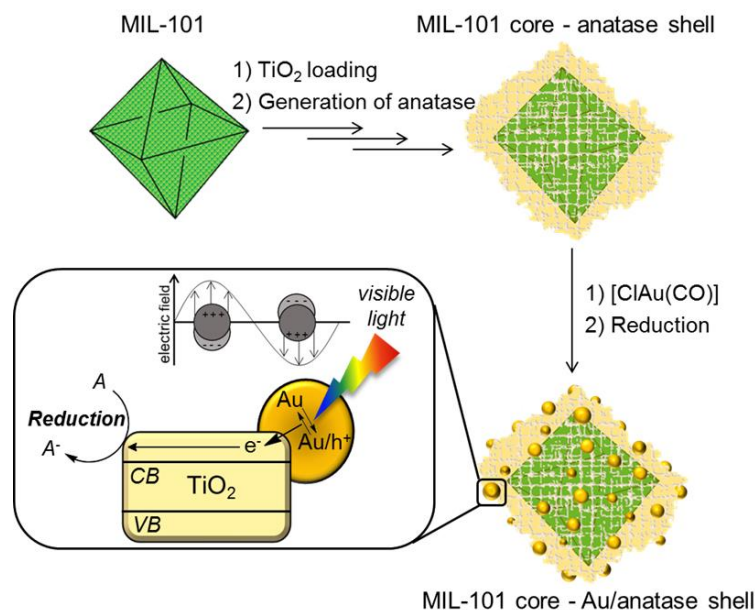


Figure 3. a) Acceptorless dehydrogenation of primary and secondary alcohols with the Pd/TiO₂@MIL-101 catalyst at 90 °C. b) Photocatalytic degradation of rhodamine B under UV light illumination using MIL-101, TiO₂@MIL-101, and Pd/TiO₂@MIL-101 (20 wt% Ti).

the degradation of the organic dye rhodamine B under UV light illumination (Figure 3b). The Pd/TiO₂@MIL-101 catalyst could be reused without a loss of photocatalytic activity.

The first photocatalytic results regarding the rhodamine B degradation provoked the further development of the TiO₂@MIL-101 material for applications under visible light illumination. Several requirements needed to be achieved therefore, including the formation of crystalline TiO₂ on the surface of the MIL-101 crystallites under mild conditions and the introduction of gold particles as the visible light-absorbing component. The incorporated TiO₂ could be assembled on the MIL-101 crystallite surface in a hydrothermal procedure at 150 °C, which is described in detail in chapter five. The selective formation of crystalline TiO₂ (anatase) was possible under mild conditions necessary for the preservation of the PCP/MOF structure. The anatase synthesis procedure described was repeated multiple times in order to generate a dense anatase shell around the MIL-101. The resulting material was denoted as MIL-101 core-anatase shell therefore. Due to the light absorption of the crystalline anatase exclusively in the UV light region, the TiO₂ surface was decorated with gold nanoparticles. Gold particles have been studied intensively for the generation of excited electrons under visible light illumination resulting from the localized surface-plasmon resonance effect. The electrons are supposed to be separated from the corresponding holes via the conduction band of TiO₂ to enhance the charge carrier separation and the photocatalytic activity (Scheme 2). [Ti(O*i*Pr)₄] and [ClAu(CO)] were used as the volatile precursors for the generation of TiO₂ and Au



Scheme 2. Schematic illustration of the synthesis procedure of the first example of a core-shell material combining a PCP/MOF core and a shell of Au and TiO₂. A possible explanation for the generation of electron-hole pairs is the plasmonic excitation of the gold particles under visible light illumination.

following MOCVD procedures. A dense shell comprised of TiO₂ and smaller Au particles was observed in TEM analysis, while the octahedral shape of the MIL-101 crystallites was still maintained (Figure 4a,b). The crystallinity of the components was verified by XRD measurements. The characteristic reflexes of anatase, cubic gold particles, and the structural integrity of the MIL-101 crystallites were identified (Figure 4c).

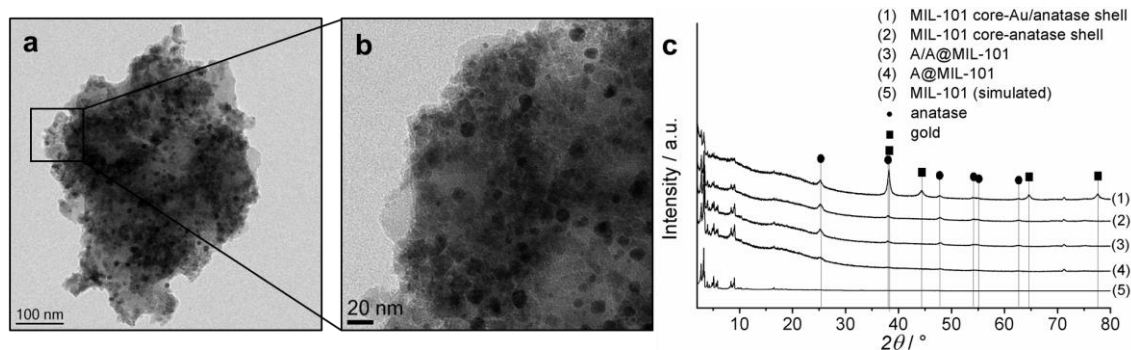


Figure 4. a,b) TEM micrographs of the MIL-101 core-Au/anatase shell material. c) XRD analysis of different MIL-101 core-shell materials.

The importance of the MIL-101 crystallites as the support for the Au/anatase shell was investigated by the controlled decomposition of the PCP/MOF. The removal of the

MIL-101 cores by calcination or etching under alkaline conditions induced the collapse of the core-shell material.

The photocatalytic activity of the novel MIL-101 core-Au/anatase shell material was investigated for wastewater treatment procedures regarding the visible light-driven degradation of the antibiotic ciprofloxacin and the toxic dyes rhodamine B, methyl orange, and methylene blue. The photocatalyst could be reused for five times with an almost constant photocatalytic activity (Figure 5a).

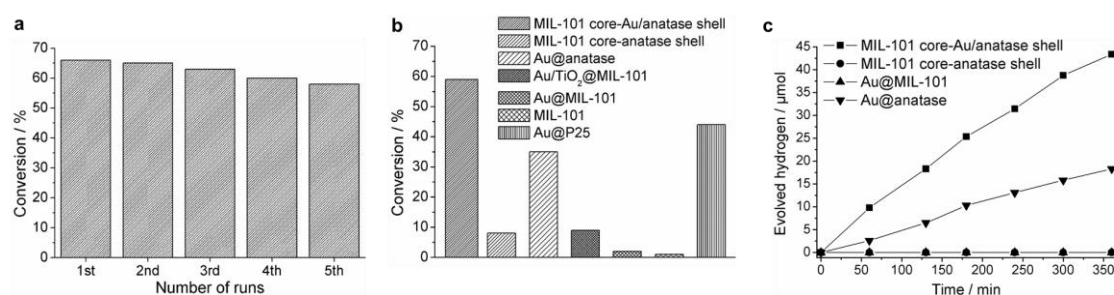
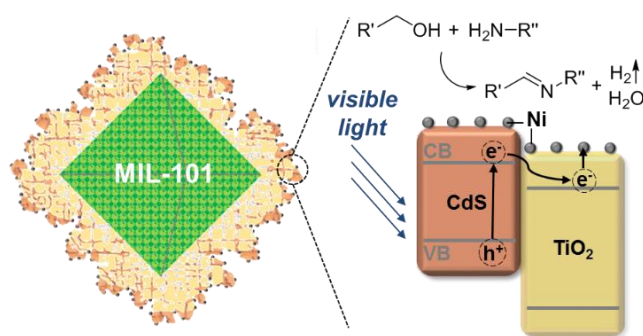


Figure 5. a) Reusability of the MIL-101 core-Au/anatase shell catalyst and b) comparison of catalysts for the photocatalytic degradation of rhodamine B. c) Photocatalytic hydrogen evolution from a water/methanol solution with the MIL-101 core-Au/anatase shell catalyst.

The decoration of the anatase shell with the Au particles increased the photocatalytic activity of the core-shell material significantly, which supports the plasmon mediated generation of reactive electrons (Figure 5b). The degradation of rhodamine B additionally proceeded faster using the MIL-101 core-Au/anatase shell catalyst in comparison to other materials containing Au and TiO₂ including Au@P25. The core-shell material was investigated for the visible light-driven hydrogen generation from water beside the photocatalytic wastewater purification described (Figure 5c). A water/methanol mixture was used for these experiments and the suspensions were purged with argon to remove the oxygen prior to the illumination with visible light. Methanol served as electron donor molecule to react irreversible with positive charged holes. A hydrogen evolution rate of 903 μmol h⁻¹ g⁻¹ was achieved for the MIL-101 core-Au/anatase shell photocatalyst. Lower rates were observed for MIL-101 core-anatase shell, Au@MIL-101, and Au@anatase, which underlines the beneficial arrangement of Au and anatase on MIL-101 in a core-shell morphology.

The use of the expensive and rare noble metal Au as an essential part of the MIL-101 core-Au/anatase shell material provoked the search for an alternative light-absorbing component with regard to a more sustainable development of the MIL-101-supported photocatalyst. The generation of a classic heterojunction system between two semiconducting materials was a promising approach in this context. The procedure for the formation of crystalline anatase on the surface of the MIL-101 crystallites in hand, the modification of TiO₂@MIL-101 with CdS was performed under solvothermal conditions to generate a CdS/TiO₂ junction system on a highly porous support material, which is described in detail in chapter six. Small Ni particles were generated on top of the CdS/TiO₂ shell of the CdS/TiO₂@MIL-101 material additionally to increase the photocatalytic activity for the visible light-driven splitting of alcohols into the corresponding aldehydes or ketones and hydrogen. The generation of carbonyl compounds via the dehydrogenation of alcohols for further C-N or C-C bond formation reactions is an elegant way to conserve our fossil carbon resources, since alcohols can be obtained from indigestible and abundantly available biomass. The junction system of the noble metal-free Ni/CdS/TiO₂@MIL-101 catalyst is promising for the efficient separation of the charge carriers generated under visible light. The material was investigated for the photocatalytic dehydrogenation of alcohols and the related imine synthesis consequently (Scheme 3).



Scheme 3. Illustration of the Ni/CdS/TiO₂@MIL-101 material with a core-shell morphology. The MIL-101-supported Ni/CdS/TiO₂ heterojunction system is an efficient photocatalyst for the dehydrogenative coupling of alcohols and amines under visible light illumination.

The crystallinity of the different components of Ni/CdS/TiO₂@MIL-101 was verified by XRD analysis. The characteristic reflexes for MIL-101 from 2° to 20° (2 θ) were observed, which indicated the structural integrity of the MIL-101 cores. The distinctive

reflex pattern of crystalline TiO_2 (anatase) and CdS (cubic) was observed. The size and the shape of the $\text{Ni/CdS/TiO}_2\text{@MIL-101}$ catalyst was investigated by TEM and high-angle annular dark-field scanning TEM (HAADF-STEM) analysis (Figure 6).

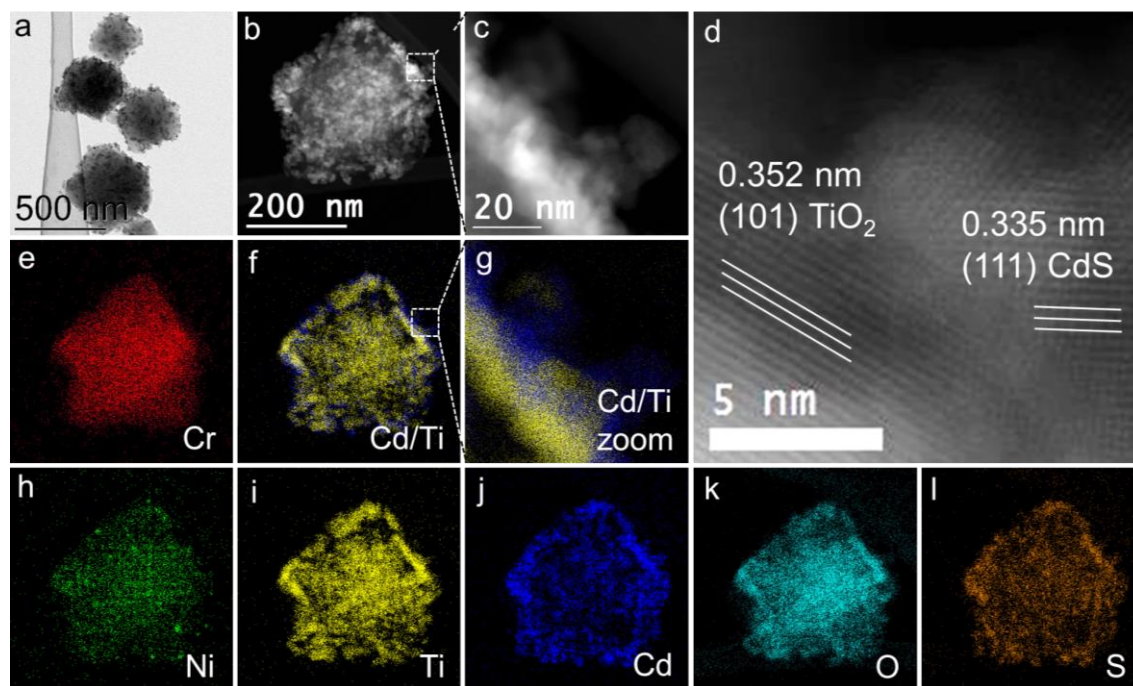


Figure 6. a) TEM micrograph of $\text{Ni/CdS/TiO}_2\text{@MIL-101}$. b-l) HAADF-STEM analysis of $\text{Ni/CdS/TiO}_2\text{@MIL-101}$ with representative energy-dispersed X-ray (EDX) element maps and characteristic lattice planes for crystalline CdS and TiO_2 .

The characteristic octahedral shape and the narrow size distribution of the MIL-101 crystallites was also observed for the $\text{Ni/CdS/TiO}_2\text{@MIL-101}$ material. The homogeneous arrangement of Ni , CdS , and TiO_2 around the MIL-101 crystallites was verified by the EDX mappings of the respective elements. Ni showed a marginal tendency for agglomeration and was proven to be located homogeneously on CdS and TiO_2 . The direct interface between crystalline CdS and TiO_2 was demonstrated by the characteristic lattice planes of anatase and cubic CdS .

The photocatalytic activity of $\text{Ni/CdS/TiO}_2\text{@MIL-101}$ was investigated first for the splitting of alcohols. The dehydrogenation of benzyl alcohol was chosen as a test reaction under Ar atmosphere at 27°C and without the addition of further electron donor molecules or additives. A 50 W blue LED (470 nm) was used as the visible light source and acetonitrile was identified as the solvent most suitable. The $\text{Ni/CdS/TiO}_2\text{@MIL-101}$ catalyst was compared to other $\text{CdS/TiO}_2\text{@MIL-101}$ catalysts, which were modified with

the noble metals Pd, Pt, and Au respectively. The noble metal-free material containing Ni clearly showed the highest activity (Figure 7a).

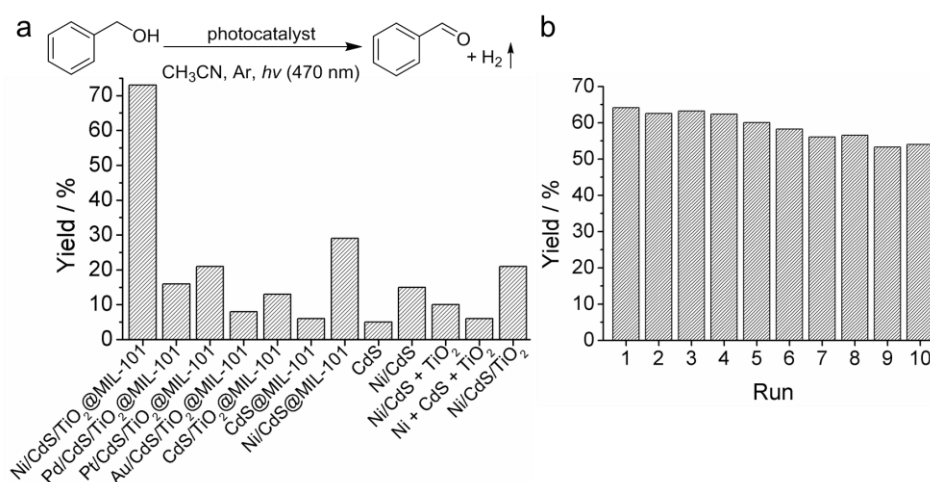
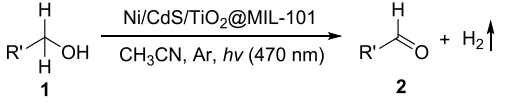
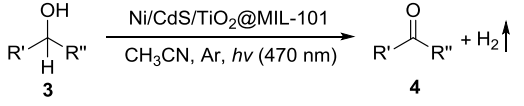
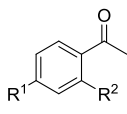
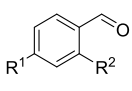
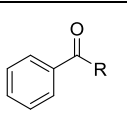
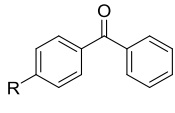
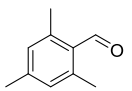
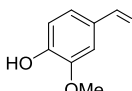
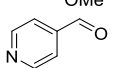
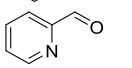
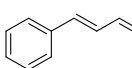


Figure 7. a) Comparison of different catalysts for the photocatalytic dehydrogenation of benzyl alcohol. The yields were determined by gas chromatography (GC) using n-dodecane as internal standard. b) Reusability of the Ni/CdS/TiO₂@MIL-101 catalyst with an activity decrease of less than 10 % after ten runs.

The beneficial effect of the CdS/TiO₂ junction system was demonstrated by the comparison of CdS/TiO₂@MIL-101 and CdS@MIL-101. All materials investigated without CdS as the visible light-responsive component (e.g. TiO₂@MIL-101, TiO₂, P25, Ni@TiO₂) showed no photocatalytic activity. The favorable effect resulting from the arrangement of Ni/CdS/TiO₂ on the MIL-101 crystallites was also demonstrated in comparison to pure Ni, CdS, and TiO₂ or Ni/CdS/TiO₂. The Ni/CdS/TiO₂@MIL-101 catalyst could be reused for ten runs for the photocatalytic dehydrogenation of benzyl alcohol without a significant decrease of activity (Figure 7b). The structural integrity of the photocatalyst reused was proven by TEM and XRD measurements. A light on/off experiment was performed and the generation of hydrogen from the dehydrogenation of benzyl alcohol proceeded only under the LED illumination. The Ni/CdS/TiO₂@MIL-101 photocatalyst offered the formation of aldehydes as well as aryl-alkyl, diaryl, and dialkyl ketones via the dehydrogenation of the corresponding alcohols. A variety of functional groups was well tolerated including halogens, methoxy, hydroxyl, trifluoromethyl, and amino groups. Hydrogenation-sensitive functional groups, such as nitrile and nitro groups, and C=C bonds were tolerated selectively. A total of 38 primary (**1**) and

secondary alcohols (**3**) was converted selectively to the respective carbonyl compounds in good to excellent yields (Table 1).

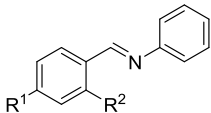
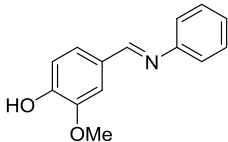
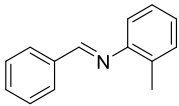
Table 1. Photocatalytic dehydrogenation of aryl, aryl-alkyl, diaryl, and dialkyl alcohol compounds.^[a]

|  | |  | | | |
|---|---|---|---|---------------------|---------------------|
| 2a R ¹ = H, R ² = H | >99 % | 4a R ¹ = H, R ² = H | 97 % | | |
| 2b R ¹ = OMe, R ² = H | 93 % | 4b R ¹ = OMe, R ² = H | 96 % | | |
| 2c R ¹ = H, R ² = OMe | >99 % | 4c R ¹ = Me, R ² = H | 92 % | | |
| 2d R ¹ = Me, R ² = H | 82 % |  | 4d R ¹ = H, R ² = Me | 81 % | |
| 2e R ¹ = H, R ² = Me | 87 % | | 4e R ¹ = Me, R ² = Me | 83 % ^[b] | |
| 2f R ¹ = F, R ² = H | >99 % | | 4f R ¹ = F, R ² = H | 71 % ^[c] | |
| 2g R ¹ = Cl, R ² = H | 87 % | | 4g R ¹ = Cl, R ² = H | 97 % | |
| 2h R ¹ = H, R ² = Cl | 96 % ^[b] | 4h R ¹ = Br, R ² = H | 96 % | | |
|  | 2i R ¹ = Br, R ² = H | 83 % ^[b] |  | 4i R = Et | 93 % |
| | 2j R ¹ = OH, R ² = H | 87 % ^[b] | | 4j R = Bu | 83 % ^[b] |
| 2k R ¹ = H, R ² = OH | 93 % | 4k R = CH ₂ OH | | 90 % ^[b] | |
| 2l R ¹ = CN, R ² = H | 93 % ^[c] |  | 4l R = H | 88 % | |
| 2m R ¹ = NO ₂ , R ² = H | 88 % ^[c] | | 4m R = Me | 91 % | |
| 2n R ¹ = H, R ² = NO ₂ | 71 % ^[c] | | 4n R = OMe | 82 % | |
| 2o R ¹ = H, R ² = NH ₂ | 96 % |  | 4o | 86 % ^[c] | |
| 2p R ¹ = CF ₃ , R ² = H | 70 % | |  | 4p | 64 % ^[d] |
| 2q R ¹ = H, R ² = CF ₃ | 89 % ^[c] | <p>[a] 0.1 mmol alcohol, 0.6 mg Ni/CdS/TiO₂@MIL-101, Ar, 0.3 mL CH₃CN, 27 °C, 24 h, 470 nm blue LED 50 W. Yields were determined by GC using n-dodecane as internal standard. [b] 1.2 mg Ni/CdS/TiO₂@MIL-101. [c] 1.2 mg Ni/CdS/TiO₂@MIL-101, 48 h. [d] Without solvent, 72 h, determined by the amount of H₂ evolved using methane as internal.</p> | | | |
|  | 2r | 78 % ^[b] | | | |
|  | 2s | 85 % | | | |
|  | 2t | 92 % ^[c] | | | |
|  | 2u | 83 % ^[c] | | | |
|  | 2v | 70 % ^[c] | | | |

The equimolar release of hydrogen during the photocatalytic dehydrogenation was verified for several substrates using methane as an internal standard. The anaerobic reaction conditions without the requirement of aqueous media is beneficial for selective

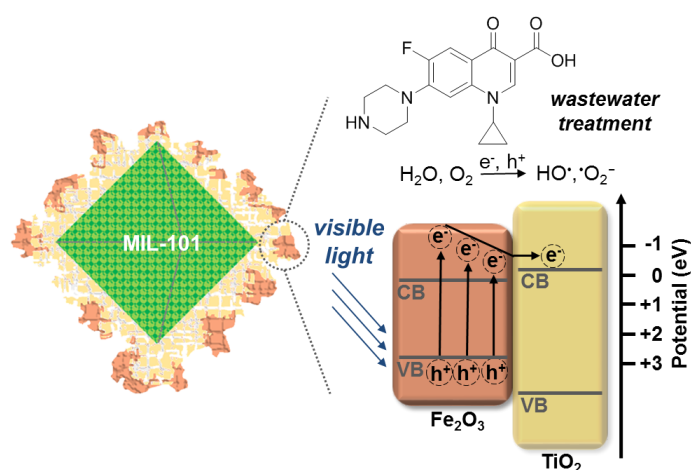
C-N multiple bond formation reactions involving condensation reactions. Herein, the photocatalytic synthesis of imines from alcohols and amines was investigated. The conditions were optimized regarding the reaction of benzyl alcohol and aniline. The release of hydrogen was surveyed again and amines formed via hydrogenation of the imines were not observed. Imines (**7**) were obtained in good to excellent yields observing a notable functional group tolerance for the variation of the alcohol and the amine component (Table 2).

Table 2. Selective photocatalytic synthesis of imines from primary alcohols and amines.^[a]

| $\text{R}'\text{-CH}_2\text{-OH} + \text{H}_2\text{N-R}'' \xrightarrow[\text{-H}_2, \text{-H}_2\text{O}]{\text{Ni/CdS/TiO}_2\text{@MIL-101, CH}_3\text{CN, Ar, } h\nu (470 \text{ nm})} \text{R}'\text{-CH=N-R}''$ | | |
|--|--|----------|
| 5 | 6 | 7 |
| | 7a R ¹ = H, R ² = H | 92 % |
| | 7b R ¹ = Me, R ² = H | 86 % |
| | 7c R ¹ = H, R ² = Me | 80 % |
|  | 7d R ¹ = OMe, R ² = H | 92 % |
| | 7e R ¹ = F, R ² = H | 76 % |
| | 7f R ¹ = Cl, R ² = H | 88 % |
| | 7g R ¹ = Br, R ² = H | 53 % |
| | 7h | 72 % |
|  | 7i R = Me | 88 % |
| | 7j R = Cl | 77 % |
| | 7k R = OMe | 93 % |
|  | 7l | 62 % |
| | 7m | 87 % |

[a] Reaction conditions: 0.1 mmol amine, 0.13 mmol alcohol, 1.5 mg Ni/CdS/TiO₂@MIL-101, Ar, 0.15 mL CH₃CN, 27 °C, 48 h, 470 nm blue LED 50 W. The yields were determined by GC using n-decane as internal standard.

The facile formation procedure of the MIL-101-supported CdS/TiO₂ heterojunction system represented a valuable basis for the generation of other junction systems on the PCP/MOF surface. The replacement of rare elements by abundantly available elements in catalytic processes is a promising option regarding the conservation of rare element sources. Fe and Ti are the two transition metals of the earth crust which appear most and their combination to accomplish efficient visible light-responsive photocatalysts is highly desirable. Therefore, the generation of a semiconductor junction system around the MIL-101 crystallites based on Fe and Ti was an interesting purpose. The formation of crystalline Fe₂O₃ on the MIL-101 crystallites was investigated starting from the TiO₂@MIL-101 core-shell material again. The volatile Fe precursor iron(0) pentacarbonyl was used for the generation of the Fe₂O₃/TiO₂@MIL-101 material employing the MOCVD procedure, which is described in detail in chapter seven. The crystallization of Fe₂O₃ on the surface of TiO₂@MIL-101 was accomplished under mild hydrothermal conditions in analogy to the formation of the crystalline TiO₂. The resulting Fe₂O₃/TiO₂@MIL-101 material is the first example of Fe₂O₃/TiO₂ generated on a PCP/MOF. Fe₂O₃ was incorporated as the visible light-absorbing component. It is well described that the excited electrons of Fe₂O₃ can be transferred into the conduction band of TiO₂ via higher energy level positions of the Fe₂O₃ conduction band to ensure the efficient charge carrier separation beneficial for photocatalytic reactions (Scheme 4).



Scheme 4. Illustration of the Fe₂O₃/TiO₂@MIL-101 photocatalyst with a core-shell morphology. The MOF-supported Fe₂O₃/TiO₂ junction system is an efficient material for visible light-driven wastewater purification.

The crystallinity of the MIL-101 cores and the semiconducting materials Fe_2O_3 and TiO_2 was investigated by XRD analysis. The reflex pattern of MIL-101 and the characteristic reflexes for crystalline Fe_2O_3 ($\alpha\text{-Fe}_2\text{O}_3$, hematite) and TiO_2 (anatase) were identified. The $\text{Fe}_2\text{O}_3/\text{TiO}_2@\text{MIL-101}$ material was analyzed by TEM and HAADF-STEM measurements to survey the morphology and the arrangement of the metal oxides (Figure 8).

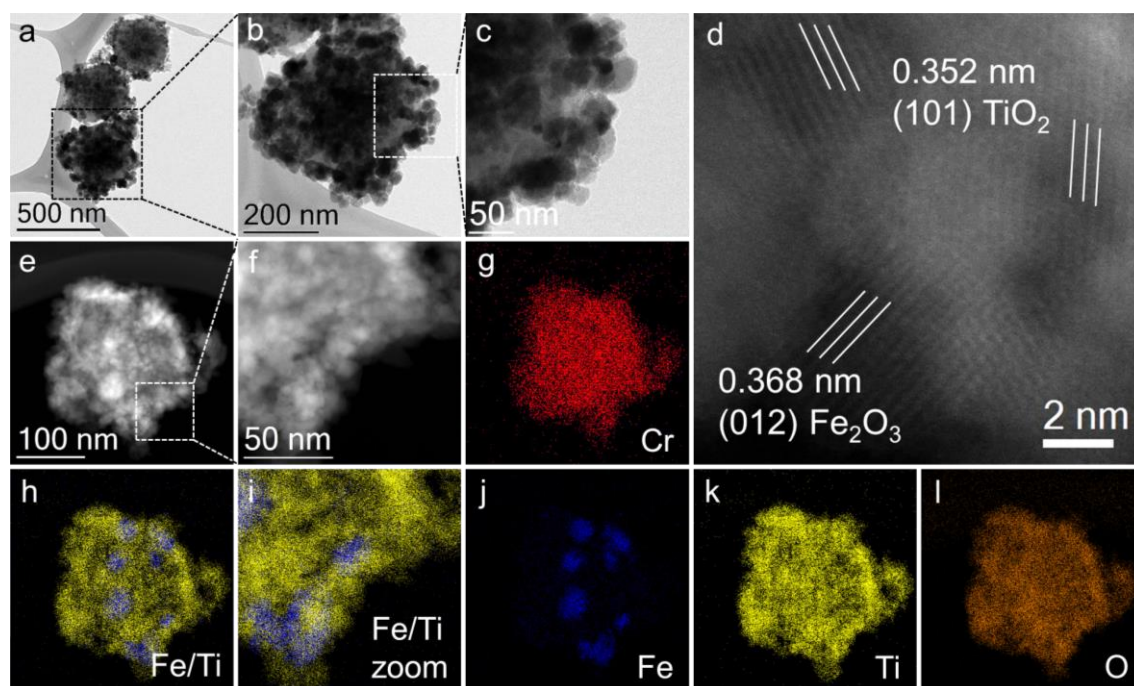


Figure 8. a-c) TEM micrographs of $\text{Fe}_2\text{O}_3/\text{TiO}_2@\text{MIL-101}$. The surface of the octahedral-shaped MIL-101 crystallites is covered entirely with Fe_2O_3 and TiO_2 particles. d-l) HAADF-STEM analysis of $\text{Fe}_2\text{O}_3/\text{TiO}_2@\text{MIL-101}$ with the characteristic lattice planes for crystalline Fe_2O_3 (hematite) and TiO_2 (anatase) and the representative EDX element maps.

The core-shell particles still exhibited an octahedral shape after the generation of Fe_2O_3 and TiO_2 . The MIL-101 surface was covered entirely with the metal oxides in a core-shell morphology, while Fe_2O_3 formed agglomerates more differentiated compared to TiO_2 . The direct interface between the $\text{Fe}_2\text{O}_3/\text{TiO}_2$ junction system could be verified by the identification of the characteristic lattice planes.

The novel $\text{Fe}_2\text{O}_3/\text{TiO}_2@\text{MIL-101}$ catalyst was investigated regarding the photocatalytic treatment of clinical wastewater. The development of sustainable technologies for wastewater recycling is of high significance due to the increasing demand for clean water and the utilization of sunlight for the oxidative decontamination of harmful organic

compounds represents an appealing approach herein. The $\text{Fe}_2\text{O}_3/\text{TiO}_2/\text{MIL-101}$ photocatalyst was investigated for the visible light-driven degradation of common pharmaceutical substances and dyes in aqueous solution. The degradation experiments were performed under air atmosphere and without the requirement of any additives at 27 °C using a 50 W blue LED (470 nm) as the visible light source. The suspensions were stirred under exclusion of light for 2 h prior to the degradation experiments to achieve the adsorption/desorption equilibrium between the contaminative compounds and the catalyst. The photocatalytic degradation of ciprofloxacin was surveyed first to evaluate the activity of the MOF-supported photocatalyst in comparison to commercially available Fe_2O_3 and TiO_2 (Figure 9).

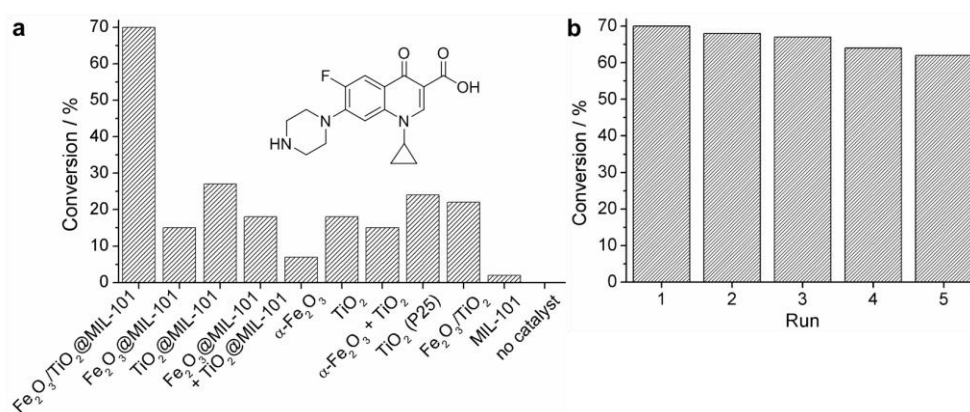


Figure 9. a) Comparison of different photocatalysts for the degradation of ciprofloxacin under visible light illumination. The conversions were determined by UV/Vis spectroscopy analysis. b) Reusability of the $\text{Fe}_2\text{O}_3/\text{TiO}_2/\text{MIL-101}$ photocatalyst.

A higher degradation efficiency was observed for the $\text{Fe}_2\text{O}_3/\text{TiO}_2/\text{MIL-101}$ photocatalyst compared to $\text{Fe}_2\text{O}_3/\text{MIL-101}$ and $\text{TiO}_2/\text{MIL-101}$, which highlights the beneficial arrangement of the two semiconducting materials on the PCP/MOF surface. The $\text{Fe}_2\text{O}_3/\text{TiO}_2$ system supported on the MIL-101 crystallites showed a higher photocatalytic activity than Fe_2O_3 (hematite), TiO_2 (anatase), and $\text{Fe}_2\text{O}_3/\text{TiO}_2$ or the commercially available TiO_2 (P25) photocatalyst. $\text{Fe}_2\text{O}_3/\text{TiO}_2/\text{MIL-101}$ could be reused for the degradation of ciprofloxacin for five successive runs with a hardly decreasing activity (Figure 9b) while the structural integrity of the catalyst was verified by TEM and XRD analysis afterwards. The degradation of the antibiotic levofloxacin and the analgesic diclofenac was investigated as further model substrates for the photocatalytic treatment of clinical wastewater (Figure 10).

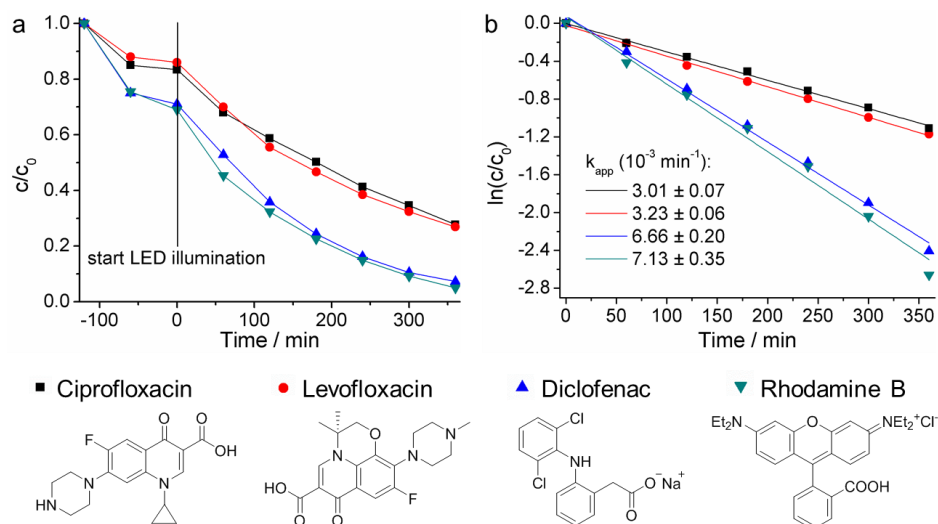


Figure 10. a) The decreasing concentrations of ciprofloxacin, levofloxacin, diclofenac, and rhodamine B during the photocatalytic degradation with $\text{Fe}_2\text{O}_3/\text{TiO}_2@\text{MIL-101}$. The adsorption/desorption equilibria between the organic compounds and the photocatalyst were maintained prior to the LED illumination. b) Kinetic degradation rates determined from $\ln(c/c_0)$ as a function of time.

The degradation of the xanthene dye rhodamine B was performed additionally to amplify the general applicability of the photocatalyst for wastewater purification. Control experiments were performed to ensure the requirement of the photocatalyst and the visible light illumination for the water decontamination experiments. Therefore, the concentrations of the four model substrates were investigated under LED illumination without catalyst and without light in presence of catalyst. Constant substrate concentrations were observed for all control experiments suggesting the wastewater treatment experiments presented to be photocatalytic processes.

3.2 Individual Contribution to Joint Publications

The results presented in this thesis were achieved in collaboration with others and are published or submitted as indicated below. The contributions of all co-authors to the respective publications are specified and the corresponding author is denoted by an asterisk.

Chapter 4

This work is published in *ChemCatChem* **2015**, 7, 3916–3922 with the title **“Titanium Dioxide Reinforced Metal-Organic Framework Pd Catalysts: Activity and Reusability Enhancement in Alcohol Dehydrogenation Reactions and Improved Photocatalytic Performance”**

Dominic Tilgner, Martin Friedrich, Justus Hermannsdörfer, and Rhett Kempe*

I synthesized and characterized all compounds, carried out the catalytic experiments and the related analytics and wrote the manuscript. Martin Friedrich performed the HRTEM and the TGA measurements. Martin Friedrich and Justus Hermannsdörfer were involved in scientific discussions. Rhett Kempe supervised this work, was involved in scientific discussions and the correction of the manuscript.

Chapter 5

This work is published in *Chem. Eur. J.* **2017**, 23, 3184–3190 with the title **“A Plasmonic Colloidal Photocatalyst Composed of a Metal-Organic Framework Core and a Gold/Anatase Shell for Visible-Light-Driven Wastewater Purification from Antibiotics and Hydrogen Evolution”**

Dominic Tilgner and Rhett Kempe*

I synthesized and characterized all compounds, carried out the catalytic experiments and the related analytics and wrote the manuscript. Rhett Kempe supervised this work, was involved in scientific discussions and the correction of the manuscript.

Chapter 6

This work is to be submitted with the title

“Visible Light-Driven Hydrogen Generation from Alcohols for C-N Multiple Bond Formation by a Metal-Organic Framework-Based Noble Metal-Free Photocatalyst”

Dominic Tilgner, Martin Friedrich, Andreas Verch, Niels de Jonge, and Rhett Kempe*

I synthesized and characterized all compounds, carried out the catalytic experiments and the related analytics and wrote the manuscript. Martin Friedrich, Andreas Verch, and Niels de Jonge performed the HAADF-STEM measurements and were involved in scientific discussions. Rhett Kempe supervised this work, was involved in scientific discussions and the correction of the manuscript.

Chapter 7

This work is submitted to *ChemPhotoChem* with the title

“A Metal-Organic Framework-Supported Nonprecious Metal Photocatalyst for Visible Light-Driven Wastewater Treatment”

Dominic Tilgner, Martin Friedrich, Andreas Verch, Niels de Jonge, and Rhett Kempe*

I synthesized and characterized all compounds, carried out the catalytic experiments and the related analytics and wrote the manuscript. Martin Friedrich performed the TGA measurements. Martin Friedrich, Andreas Verch, and Niels de Jonge performed the HAADF-STEM measurements and were involved in scientific discussions. Rhett Kempe supervised this work, was involved in scientific discussions and the correction of the manuscript.

Now this work is published as:

D. Tilgner, M. Friedrich, A. Verch, N. de Jonge, R. Kempe, *ChemPhotoChem* **2018**, *2*, 349–352.

4 Titanium Dioxide Reinforced Metal-Organic Framework Pd Catalysts: Activity and Reusability Enhancement in Alcohol Dehydrogenation Reactions and Improved Photocatalytic Performance

Dominic Tilgner, Martin Friedrich, Justus Hermannsdörfer,⁺ and Rhett Kempe^{*[a]}

[a] Anorganische Chemie II – Catalyst Design, Universität Bayreuth, Universitätsstraße 30, 95440 Bayreuth (Germany).

[⁺] Current Affiliation: INM – Leibniz-Institut für Neue Materialien, Stuhlsatzenhausweg 3, 66123 Saarbrücken (Germany).

Published in *ChemCatChem* **2015**, 7, 3916–3922.

Keywords: dehydrogenation; metal-organic framework; nanoparticles; palladium; photocatalysis

Abstract: Porous coordination polymers or metal–organic frameworks have been proposed as promising catalyst materials since their discovery. A fundamental problem associated with MOF-based catalysts is the stability during their catalytic performance, especially in liquid-phase catalysis. Herein, we report on the controlled incorporation of nanoscale palladium and titanium dioxide inside MIL-101 (Cr). The introduction of the metal species was accomplished by metal–organic chemical vapor deposition and can be varied over a large weight-percentage range. The enhanced catalytic activity and the improved reusability of the resulting Pd/TiO₂@MIL-101 composite materials were demonstrated in hydrogenation and dehydrogenation reactions. Furthermore, the presence of TiO₂ (amorphous) allowed observing an enhanced photocatalytic activity.

4.1 Introduction

Porous coordination polymers (PCP)^[1] or metal–organic frameworks (MOF)^[2] are highly ordered crystalline materials built from multidentate ligands (linkers) and metal ions or clusters (connectors). The coexistence of large specific surface areas, well defined pore

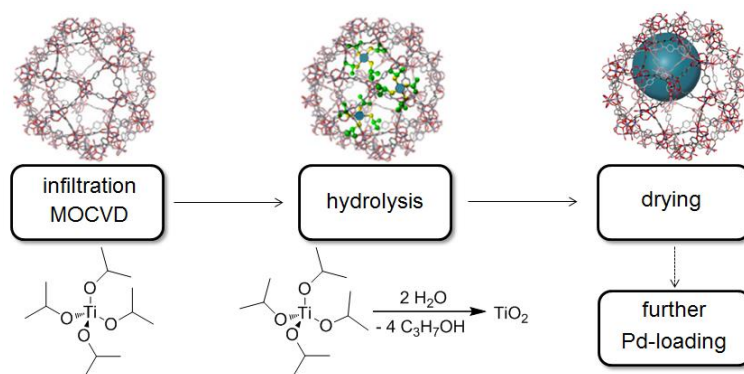
or cavity structures, and variable functionalities enables the application of MOFs in a variety of fields such as gas storage and separation, drug delivery, bioimaging, electrochemistry, sensing, and catalysis.^[3] With regard to catalytic applications, PCP/MOFs are diversely used. Catalytically active sites can result from the connectors (metal complex catalysis), from organic functionalities of the linkers (organo catalysis), or from the introduction of (well defined) metal nanoparticles (MNP).^[4] The solvent-free loading by metal-organic chemical vapor deposition (MOCVD) is an elegant method for the introduction of such MNPs.^[5] It offers a high degree of control, the addressing of broad MNP weight contents and has been used intensively in recent years to design MNP@PCP/MOF catalysts.^[5, 6] Beside the generation of highly active MNP inside the cavities of MOFs, the additional incorporation of a nanoscale semiconducting material such as titanium dioxide seems to be a promising goal with regard to (i) the outstanding photoelectric properties of titania^[7] and (ii) a potential stabilizing effect of the catalyst by the metal oxide. The incorporation of titanium dioxide in PCP/MOFs has already been reported for a few examples.^[8] To the best of our knowledge, the selective loading of PCP/MOFs with TiO₂ and noble MNPs is a not yet solved problem.^[6h]

We have a rather long ongoing interest^[6f,j,m,n, 9] in PCP/MOF synthesis and catalysis and report here on the combined incorporation of titanium dioxide and palladium nanoparticles into MIL-101 (Cr). The Pd/TiO₂@MIL-101 composite materials are highly efficient catalysts in hydrogenation and dehydrogenation reactions. A superior performance in comparison to classic Pd catalysts like Pd@AC (AC=activated carbon), Pd@Al₂O₃, or Pd@SiO₂ has been observed. Besides the very good activity, stability, and reusability, an enhanced photocatalytic activity has been noticed for Pd/TiO₂@MIL-101. MIL-101[10] was chosen as host material because of its stability towards moisture and its impressive use in liquid-phase catalysis aroused from different incorporated monometallic species (Au,^[11] Cu,^[12] Fe₂O₃/Fe₃O₄,^[13] Pd,^[6j,m,n, 14] Pt,^[6f, 14o, 15] and Rh^[16]), bimetallic alloys,^[17] or MNP-free functional sites.^[18]

4.2 Results and Discussion

The loading of the Ti precursor titanium(IV) isopropoxide [Ti(OiP)₄] into MIL-101 was accomplished by sublimation.^[8a] The size of the synthesized MIL-101 crystallites was adjusted by the amount of HF and repetitive centrifugation steps to obtain a narrow size

range centered at a diameter of 180 nm (Supporting Information, Figure S1). Such crystallite size is optimal with regard to activity (preferred as small as possible) and easy separation of the catalyst (preferred as large as possible).^[6n] A specific surface area of 2900 m²g⁻¹ and the characteristic cavities of MIL-101 were observed for these crystallites (Figure S2). The general synthesis strategy for TiO₂@MIL-101 is illustrated in Scheme 1.



Scheme 1. Preparation of TiO₂@MIL-101. The Ti-precursor [Ti(O-iP)₄] was infiltrated into MIL-101 by MOCVD and thermally decomposed to titania under water atmosphere. The dry TiO₂@MIL-101 materials enabled further metal loading with Pd.

The volatile Ti-precursor titanium(IV) isopropoxide was infiltrated into MIL-101 under dynamic vacuum (10⁻⁴ mbar) at 35 °C for 20 h. The gas-phase loading procedure enabled the homogeneous disposition of the precursor inside the porous structure of the metal-organic host system. The hydrolysis of [Ti(O-iP)₄] led to the disposal of 2-propanol and the formation of TiO₂. The removal of precursor recesses and adsorbed water under vacuum resulted in titania-loaded MIL-101 that permitted the further incorporation of palladium nanoparticles (*vide infra*). The amount of titanium(IV) isopropoxide was varied for several gas-phase loadings to find the maximal loading capacity. Loading of MIL-101 with Ti contents ≥ 30 wt% led to the formation of titania agglomerates outside the PCP/MOF crystallites (Figure S6). To achieve a homogeneous dispersion of TiO₂ inside the MIL-101 crystallites, Ti loadings of 20 wt% and lower seemed appropriate. The subsequent generation of noble MNPs was also accomplished by gas-phase loading. The infiltration of volatile [(η⁵-C₅H₅)Pd(η³-C₃H₅)] was followed by the hydrogenolysis of the Pd precursor at 70 °C and 50 bar H₂ and led to Pd/TiO₂@MIL-101^[6j,m,n] with approximately 10 wt% of Pd. The incorporation of TiO₂ resulted in the reduction of the specific surface area of the composites. TiO₂@MIL-101 materials with Ti contents of

10 wt% and 20 wt% exhibited surface-area decreases of 38 % and 59 %, respectively. It indicates a precursor deposition in the cavities of MIL-101. Further loading of TiO₂@MIL-101 with Pd decreased the remaining specific surface area of the composite materials as well (Supporting Information, Table S1). Inductively coupled plasma optical emission spectroscopy (ICP–OES) provides insight into the exact metal contents of TiO₂ and Pd nanoparticles. The theoretical metal contents (assuming all precursor material is incorporated) are consistent with the measured values for titanium and palladium with minor deviations (Table 1).

Table 1. ICP-OES analysis of TiO₂@MIL-101 and Pd/TiO₂@MIL-101 compounds with different metal contents (wt%). The adjusted Pd and Ti contents achieved by MOCVD loading of the MOF MIL-101 were conform to the theoretical adjusted contents of 10, 15, 20, or 30 wt%.

| Sample | Pd content [wt%] | Ti content [wt%] |
|------------------------------|------------------|------------------|
| TiO ₂ @MIL-101 | - | 20.2 |
| TiO ₂ @MIL-101 | - | 33.5 |
| Pd/TiO ₂ @MIL-101 | 9.8 | 15.3 |
| Pd/TiO ₂ @MIL-101 | 11.4 | 20.2 |

X-ray powder diffraction analysis (XRD) of the TiO₂@MIL-101 materials with Ti contents from 5 wt% to 30 wt% displays the characteristic pattern of MIL-101 from 2 to 20° (2 θ), which supports the integrity of the metal-organic host structure after the incorporation of TiO₂. No peaks were found at the calculated reflex positions for crystalline titanium dioxide (anatase or rutile) indicating the presence of amorphous TiO₂. The compounds with high Ti contents exhibited intensified noise signals caused by the amorphous TiO₂ (Figure 1). The hydrolysis of pure [Ti(O-iP)₄] in analogy to the preparation procedure of TiO₂@MIL-101 resulted in the formation of amorphous TiO₂, too (Figure S9). The unsupported amorphous titanium dioxide generated this way has a specific surface area of 500 m²g⁻¹ (Figure S7 a,b). The additional incorporation of palladium into TiO₂@MIL-101 led to regularly arranged Pd particles with a mean diameter of 2.2 nm and a narrow particle-size distribution as visualized by transmission electron microscopy (TEM). High-resolution transmission electron microscopy

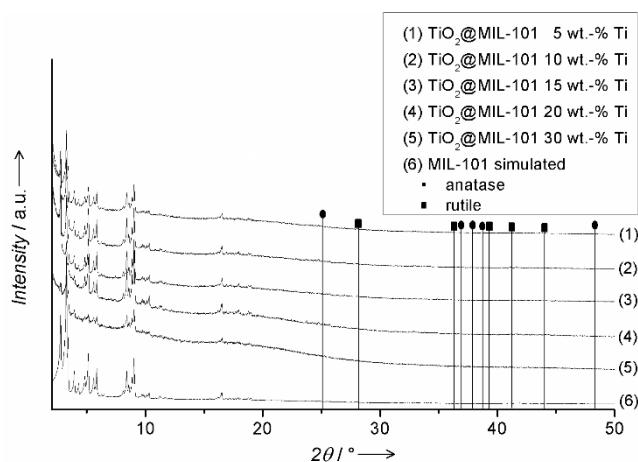


Figure 1. XRD analysis of $\text{TiO}_2\text{@MIL-101}$ with different Ti contents (5, 10, 15, 20, and 30 wt%) in comparison to MIL-101. The intensified noise signal of crystalline MIL-101 in the range from 2 to 30° (2θ) caused by infiltrated amorphous titanium dioxide correlates with rising Ti contents.

(HRTEM) indicates the presence of Pd nanoparticles based on a distance of 0.224 nm between adjacent lattice planes, which is the characteristic value for the (111) planes of cubic Pd (Figure 2).

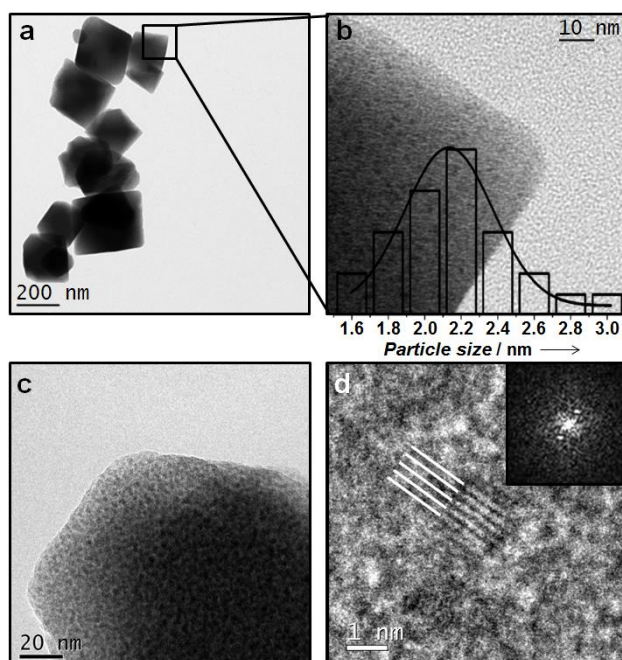


Figure 2. a) TEM images of $\text{Pd/TiO}_2\text{@MIL-101}$ (10 wt% Pd, 20 wt% Ti) confirm the integrity of the metal–organic host system and the absence of larger titanium dioxide aggregates outside the MIL-101 crystallites. b) The highly controlled Pd loading of $\text{TiO}_2\text{@MIL-101}$ enabled narrow Pd NP size distributions. c,d) Homogeneous palladium loading can additionally be illustrated by HRTEM analysis including the characteristic Pd lattice planes marked by white lines in (d). The inset in (d) shows the diffractogram.

Electron energy loss spectroscopy (EELS) analysis of $\text{TiO}_2@\text{MIL-101}$ (20 wt% Ti) shows the characteristic energy loss peaks for incorporated titanium, chromium, and oxygen corresponding to the composition of MIL-101 (Figure 3a).

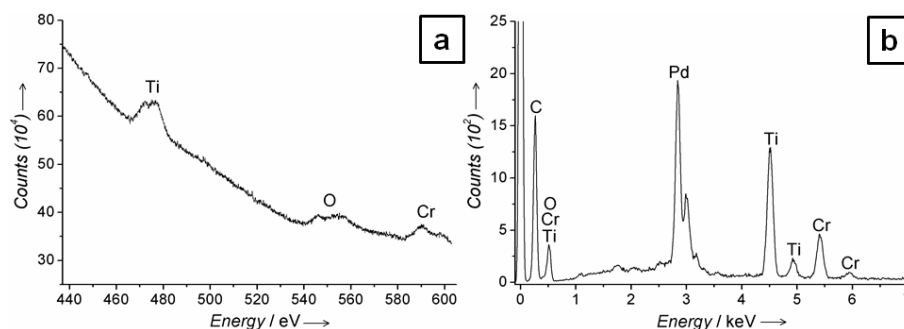


Figure 3. a) EELS analysis of $\text{TiO}_2@\text{MIL-101}$ (20 wt% Ti) with characteristic energy loss peaks for Ti, O, and Cr indicates the incorporation of Ti. b) EDX analysis of $\text{Pd}/\text{TiO}_2@\text{MIL-101}$ with characteristic element peaks for Pd and Ti incorporated in MIL-101.

A qualitative investigation of the chemical composition was also performed by energy-dispersive X-ray spectroscopy (EDX) analysis. The signals of Pd and Ti, as well as the element signals of the metal-organic framework (Cr, C, and O), were identified by the characteristic elemental peaks (Figure 3b). The incorporation of Pd and TiO_2 in MIL-101 affects the light absorption behavior of the MOF. The UV-light absorption of $\text{TiO}_2@\text{MIL-101}$ was enhanced compared to pure MIL-101 (Figure S4). Pure amorphous TiO_2 prepared in analogy to the synthesis protocol of $\text{TiO}_2@\text{MIL-101}$ resulted in a colorless powder and featured light absorption in the UV-light range from 200 to 380 nm. Additional loading of $\text{TiO}_2@\text{MIL-101}$ with palladium nanoparticles resulted in gray to black materials (depending on the Pd content) with almost constant light absorption over the entire irradiated range from 200 to 800 nm (Figure S5).

The combined introduction of nanoscale Pd and TiO_2 into MIL-101 led to a multifunctional catalyst material. A preliminary investigation of the photocatalytic activity was performed by the decoloration of the organic dye rhodamine B (RhB). The increased photoactivity of $\text{TiO}_2@\text{MIL-101}$ and $\text{Pd}/\text{TiO}_2@\text{MIL-101}$ in comparison to the activity of pure MIL-101 could be verified by the rate constants for the degradation of RhB in aqueous solution in the presence of external irradiated UV light (Figure 4). The decrease of the dye concentration determined by UV/Vis measurements at 552 nm approximately followed pseudo-first-order kinetics. $\text{Pd}/\text{TiO}_2@\text{MIL-101}$ offered the

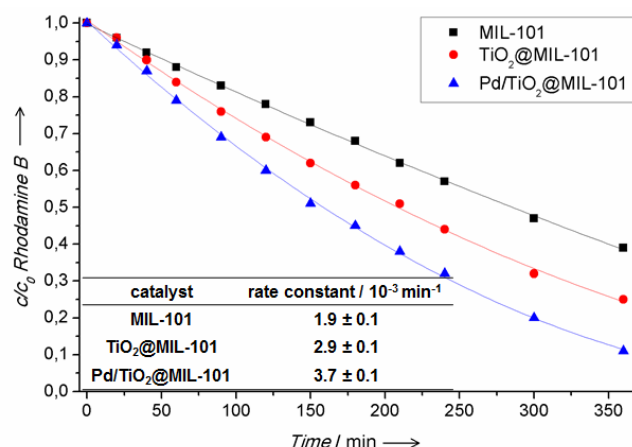


Figure 4. Degradation of RhB by MIL-101, TiO₂@MIL-101 (20 wt% Ti) and Pd/TiO₂@MIL-101 (10 wt% Pd, 20 wt% Ti) under irradiation of UV light with normalized catalyst loading referred to the MIL-101 amount. c and c_0 are the intensities of the absorbance peak at 552 nm at the reaction time and the initial time, respectively.

largest rate constant of 3.7 ± 0.1 ($\times 10^{-3} \text{ min}^{-1}$) and a half-life time of 185 min. TiO₂@MIL-101 [2.9 ± 0.1 ($\times 10^{-3} \text{ min}^{-1}$)] also showed faster degradation of RhB than MIL-101 [1.9 ± 0.1 ($\times 10^{-3} \text{ min}^{-1}$)]. The adsorption of the dye molecule inside the porous structure of the used MIL-101 based photocatalysts reduced the concentration of the RhB solution. To distinguish between the photochemically induced degradation of RhB and the reduction of the dye concentration through adsorption by the porous hosts, the reaction mixture was stirred for 2 h under exclusion of light prior to photocatalysis. Significant dye adsorption was observed during this pretreatment. The degradation of the RhB concentration was also measured without UV-light irradiation to prove the stability of the dye under the reaction conditions. No degradation of RhB was observed (Figure S11). Furthermore, no decrease of the RhB concentration was determined if it was exposed to UV light in the absence of the catalyst materials (Figure S12). The photochemically induced degradation of RhB was also investigated in presence of amorphous TiO₂ and Pd@TiO₂ as photocatalysts. These TiO₂ based materials showed a significantly slower degradation of the dye. The reduction of the RhB concentration under the same conditions as applied above was 29 % for TiO₂ and 45 % for Pd@TiO₂ (Figure S14). The reusability of Pd/TiO₂@MIL-101 was investigated for two additional runs pointing out the stability of the catalyst system under the UV-light conditions (Figure S15). Steady rate constants and conversions were observed.

In addition to the photocatalytic activity, the performance of Pd/TiO₂@MIL-101 in

hydrogenation and dehydrogenation reactions was investigated. We were especially interested in analyzing the long-time stability and the reusability of the novel catalysts introduced here. First, the hydrogenation of acetophenone in combination with a thermal treatment was investigated. Pd/TiO₂@MIL-101 (20 wt% Ti) and Pd@MIL-101 were thermally treated at 150 °C for 20 h prior to each catalytic run and reused several times. A stable conversion was observed for Pd/TiO₂@MIL-101 for five runs. In contrast, Pd@MIL-101, showing the same conversion for the first run, continuously decomposes indicated by lower conversion numbers from run to run (Supporting Information and Figure 5).

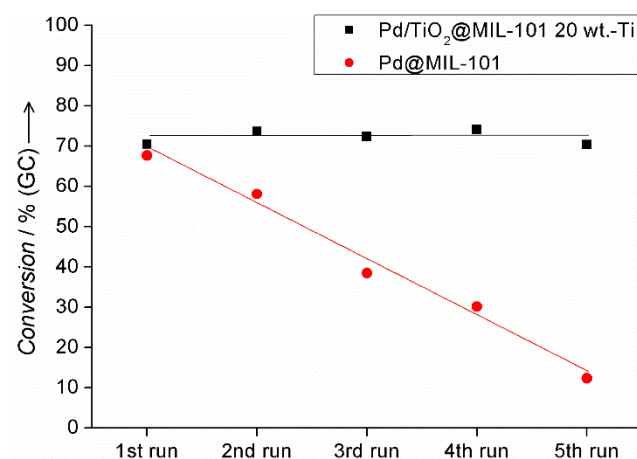


Figure 5. Conversion for the reduction of acetophenone to 1-phenylethanol (50 °C, 30 bar H₂, 20 h, 600 rpm, 0.05 mol% Pd) with thermal treatment of the two catalysts before each catalytic run (150 °C, 20 h).

Second, Pd/TiO₂@MIL-101 and Pd@MIL-101 were used as catalysts for the hydrogenation of benzophenone at 140 °C. Pd/TiO₂@MIL-101 with 10 wt% and 20 wt% of Ti were compared with Pd@MIL-101. A very good long-time stability and reusability was observed for the TiO₂-loaded catalysts. The catalytic activity of Pd@MIL-101 clearly decreases over five runs (Figure 6). The structural integrity of the Pd/TiO₂@MIL-101 catalyst with 20 wt% Ti after five runs of hydrogenation of benzophenone at 140 °C was demonstrated by XRD analysis displaying the representative reflexes of MIL-101 (Figure S10). Third, we investigated our catalysts in dehydrogenation reactions. The acceptor-

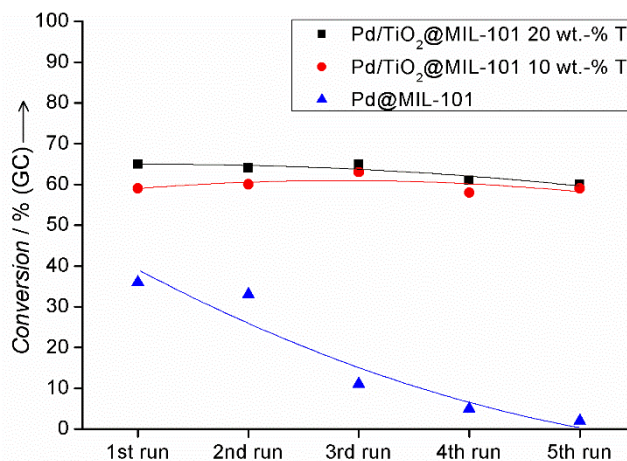


Figure 6. Conversion for the reduction of benzophenone to diphenylmethanol (140 °C, 30 bar H₂, 5 h, 600 rpm, 0.01 mol% Pd) in the presence of Pd/TiO₂@MIL-101 for two different TiO₂ loadings with constant conversions and excellent recyclability of the stabilized catalysts in comparison to Pd@MIL-101.

less dehydrogenation of alcohols generating reactive carbonyl groups and dihydrogen is an attractive reaction in terms of organic synthesis and hydrogen production.^[19] The dehydrogenation of diphenylmethanol to benzophenone using Pd/TiO₂@MIL-101 could be performed with considerably higher conversions than using Pd@MIL-101 (Figure 7).

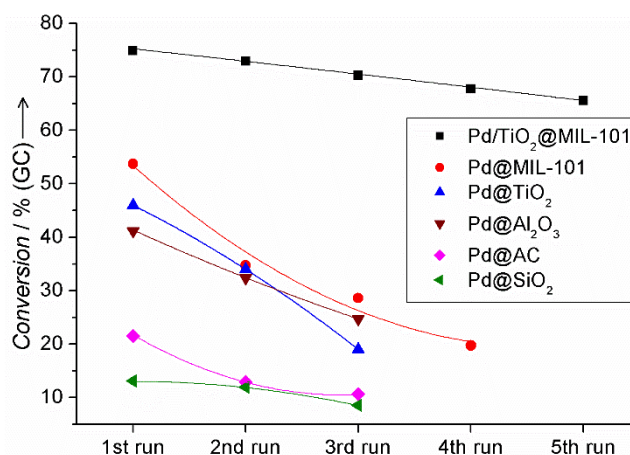


Figure 7. Conversion for the dehydrogenation of diphenylmethanol to benzophenone (130 °C, 60 h, 600 rpm, 0.3 mol% Pd) in the presence of Pd/TiO₂@MIL-101 (20 wt% Ti), unstabilized Pd@MIL-101, Pd@TiO₂, and commercial available Pd-catalysts (Pd@Al₂O₃, Pd@AC, and Pd@SiO₂).

In addition, Pd/TiO₂@MIL-101 showed only a slightly decrease of the activity over five runs. Pd@MIL-101 decomposes significantly faster. Furthermore, the

Pd/TiO₂@MIL-101 catalyst system enabled a higher catalytic activity and considerable better reusability than Pd@TiO₂ or the commercially available Pd catalysts such as Pd@AC, Pd@Al₂O₃, and Pd@SiO₂. Finally, the dehydrogenation of several alcohols was performed by using Pd/TiO₂@MIL-101 at the relatively low temperature of 90 °C in combination with small catalyst loadings (0.3 mol% Pd). Efficient acceptor-less alcohol dehydrogenation under neutral conditions and below 100 °C is rare and has been observed for homogenous catalysts mainly.^[20] Very good conversions and selectivities have been observed for secondary alcohols (Table 2).

Table 2. Acceptor-less dehydrogenation of aromatic alcohols through C–H activation by Pd/TiO₂@MIL-101 (90 °C, 0.3 mol% Pd).

| Entry | Substrate | Product | Conversion [%] ^[a] | Selectivity [%] ^[a] |
|-------------------|---|---|-------------------------------|--------------------------------|
| 1 ^[b] |  |  | 98 | 97 |
| 2 ^[c] |  |  | 98 | > 99 |
| 3 ^[c] |  |  | 94 | > 99 |
| 4 ^[d] |  |  | 91 | > 99 |
| 5 ^[b] |  |  | 96 | 97 |
| 6 ^[b] |  |  | 93 | 92 |
| 7 ^[c] |  |  | 95 | > 99 |
| 8 ^[d] |  |  | 91 | > 99 |
| 9 ^[b] |  |  | 96 | 58 ^[e] |
| 10 ^[c] |  |  | 97 | 67 ^[f] |

[a] Determined by GC. [b] 24 h. [c] 40 h. [d] 48 h. [e] Byproduct benzyl benzoate.

[f] Byproduct 4-methylbenzyl 4-methylbenzoate.

4.3 Conclusions

We generated multifunctional metal-organic framework (MOF) catalysts by incorporating noble-metal nanoparticles (Pd) and nanoscale TiO₂. The volatile precursor titanium(IV) isopropoxide was sublimed into MIL-101 in different amounts. Subsequent hydrolysis led to the formation of TiO₂@MIL-101. Further quantitative gas-phase loading of [(C₅H₅)Pd(C₃H₅)] gave rise (after reduction by hydrogen) to Pd/TiO₂@MIL-101 composite materials. Pd/TiO₂@MIL-101 materials are efficient catalysts in hydrogenation and dehydrogenation reactions. A superior activity and a very good reusability were observed for Pd/TiO₂@MIL-101 in comparison to Pd@MIL-101, Pd@TiO₂, and commercially available Pd-catalysts such as Pd@Al₂O₃, Pd@AC, and Pd@SiO₂. The relevance for catalysis in general is the superior performance (activity and reusability) of the catalyst system introduced here in comparison to classic Pd catalysts. The MOF–TiO₂ host combines excellent and stable Pd dispersion as well as an efficient accessibility of the active sites. Furthermore, Pd/TiO₂@MIL-101 is an efficient photocatalyst.

4.4 Experimental Section

Reactants and Solvents

All manipulations of air-sensitive products were performed under dry and oxygen-free argon atmosphere (Schlenk techniques) or in a nitrogen-filled glovebox (mBraun) with a high-capacity recirculator (below 0.1 ppm of oxygen and water). Manipulations with light sensitive substances were carried out under exclusion of light. n-hexane and THF were distilled from sodium benzophenone ketyl. 1-Phenylethanol C₈H₁₀O, 1-(2-methoxyphenyl)ethanol C₉H₁₂O₂, 1-(2-methylphenyl)ethanol C₉H₁₂O, 1-(4-fluorophenyl)ethanol C₈H₈FO, 1-(4-methoxyphenyl)ethanol C₉H₁₂O₂, 1-(4-methylphenyl)ethanol C₉H₁₂O, 1-phenyl-1-pentanol C₁₁H₁₆O, 1-phenyl-1-propanol C₉H₁₂O, 4-methylbenzyl alcohol C₈H₁₀O, acetophenone C₈H₈O, allylpalladium(II) chloride dimer [(C₃H₅)₂Pd₂Cl₂], benzophenone C₁₃H₁₀O, benzyl alcohol C₇H₈O, chromium(III) nitrate nonahydrate [Cr(NO₃)₃·9H₂O], diphenylmethanol C₁₃H₁₂O, ethanol C₂H₆O, hydrofluoric acid HF, n-dodecane C₁₂H₂₆, Pd@AC, Pd@Al₂O₃, Pd@SiO₂, rhodamine B C₂₈H₃₁ClN₂O₃, sodium cyclopentadienide NaC₅H₅, terephthalic acid C₆H₄(COOH)₂, and titanium(IV)

isopropoxide $[\text{Ti}(\text{OCH}(\text{CH}_3)_2)_4]$ were obtained commercially from Sigma-Aldrich, ABCR or Acros Organics and used without further purification. The products $[(\eta^5\text{-C}_5\text{H}_5)\text{Pd}(\eta^3\text{-C}_3\text{H}_5)]^{[21]}$ and MIL-101 (Cr)^[6n] were prepared according to published procedures.

Characterization

¹H NMR spectra were recorded with a Varian Unity 300 MHz spectrometer. Chemical shifts given in ppm were recorded at 25 °C and are referenced using CDCl₃ as internal standard. EDX measurements were performed with a Zeiss 1540 EsB Cross beam, equipped with a Thermo Noran System Six EDX-system. Elemental analysis was performed by standard protocols employing microwave assisted digestion in HNO₃/HCl/H₃PO₄/(BF₄)⁻H⁺ and inductively coupled plasma optical emission spectrometry using a Varian Vista-Pro radial. FTIR measurements were performed at a Perkin-Elmer FTIR-Spectrum 100 over a range from 4000 cm⁻¹ to 500 cm⁻¹. GC analyses were performed using an Agilent Technologies 6850 gas chromatograph equipped with a flame ionization detector (FID) and a MN Optima 17 capillary column (30.0 m × 0.32 mm × 0.25 μm) using n-dodecane as internal standard and THF as solvent. Gas mixtures were analyzed using a Agilent special Plot and Molsieve capillary column (30.0 m × 0.32 mm × 0.25 μm). GC-MS analyses were performed using an Agilent Technologies 6890 gas chromatograph with a MN-MS HP-5 capillary column (30.0 m × 0.32 mm × 0.25 μm) and a coupled mass spectrometer as detector. Nitrogen physisorption isotherms were determined at -196 °C using a Quantachrome Nova 2000e apparatus. Specific surface areas were calculated by using p/p₀-values from 0.05-0.25 by the BET method. Specific total pore volumes were measured by the DFT calculations (N₂ at -196 °C on silica (cylindr. pore, NLDFT equilibrium model)). TEM measurements were conducted by using a LEO 9220 (Carl Zeiss, 200 kV). The samples were suspended in chloroform and sonicated for 5 min. A volume of 2 μL of the suspension was placed on a CF200-Cu-grid (Electron Microscopy Sciences) and allowed to dry. HRTEM measurements were performed by using a CM 300 UT (Philips, 300 kV). The samples were suspended in chloroform and sonicated for 5 min. A volume of 2 μL of the suspension was placed on a CF200-Cu-grid with a lacey carbon film (Electron Microscopy Sciences) and allowed to dry. TGA analysis were performed from 30 °C to 450 °C (5 °C min⁻¹) using a Mettler TGA/SDTA 85 under air. UV/Vis spectra (liquid)

were taken for supernatants of the reaction solutions in the range of 400-600 nm using a CARY 300 (Agilent Technologies) with Scan-software and PS-cuvettes (12.5 mm × 12.5 mm × 45 mm). Solid-state UV/Vis spectra were measured using a CARY 300 with an Ulbricht sphere in the range of 200 nm to 800 nm. XRD diffractograms were recorded by using a STOE STADI-P-diffractometer (Cu κ α radiation, 1.54178 Å) in Θ -2 Θ -geometry with a position sensitive detector.

Syntheses and Reactions

Synthesis of MIL-101: [Cr(NO₃)₃·9H₂O] (640 mg, 1.60 mmol), H₂BDC (265 mg, 1.60 mmol), HF 40 wt% (10 mL, 0.228 mmol) and deionized H₂O (8.00 mL) were combined and sealed in a 23 mL Teflon-lined hydrothermal autoclave. The mixture was heated for 1 h at 80 °C (heating rate: 2.7 °C min⁻¹) and for 7.45 h at 220 °C (4.7 °C min⁻¹). The reaction mixture was cooled down fast to 160 °C and slowly to 30 °C (cooling rate: 5.4 °C h⁻¹). Excessively crystallized H₂BDC was removed by filtration over a pore 3 filter. The green product was separated from the reaction solution by centrifugation (2000 rpm, 45 min). The MIL-101 was heated to reflux in ethanol/water (90/10 vol.%) for 14 h and centrifuged (1800 rpm, 45 min) three times to remove grimaldiite (α -CrOOH) impurities. Repetitive differential centrifugation in ethanol/water (1800 rpm, 5 min) was also used to separate MIL-101 crystals with different size distribution. The different MIL-101 fractions were dried under vacuum (10⁻⁴ mbar, 85 °C). (BET: 2900 m² g⁻¹; XRD (2 Θ (°), intensity (%)): 2.78 (56), 3.26 (100), 3.41 (44), 3.94 (19), 4.30 (11), 4.84 (16), 5.13 (32), 5.59 (16), 5.85 (22), 6.24 (5), 6.48 (5), 8.10 (7), 8.40 (22), 8.58 (11), 8.86 (15), 9.02 (28), 9.71 (5), 9.86 (5), 10.30 (6), 11.22 (4), 16.50 (6)).

Synthesis of [(η^5 -C₅H₅)Pd(η^3 -C₃H₅)]: A solution of NaCp (1.50 g, 17.1 mmol) in 40 mL of THF was added dropwise to a solution of [(C₃H₅)₂Pd₂Cl₂] (2.50 g, 6.83 mmol) in 50 mL of THF at -78 °C. The reaction mixture was stirred for 10 min at -78 °C, warmed up to room temperature and stirred for another 15 min at room temperature. The solvent was removed under vacuum and the resulting residue was dissolved in n-hexane. The NaCl was removed by cannula filtration and the solvent was removed under vacuum. The red residue was sublimated under vacuum (10⁻⁴ mbar) and the obtained red crystals were stored under exclusion of light and air at -30 °C. (Yield 2.50 g, 11.76 mmol (86 %)). ¹H NMR (300 MHz, CDCl₃): δ = 1.74 (d, ³J_{HH} = 9.83 Hz, 2H, CH₂), 3.11 (d, ³J_{HH} = 6.10 Hz,

2H, CH₂), 4.47 (m, 1H, CH), 5.23 ppm (s, 5H, C₅H₅).

Synthesis of amorphous TiO₂: The precursor compound [Ti(O-iP)₄] was processed in hydrolysis to yield amorphous TiO₂. The hydrolysis of [Ti(O-iP)₄] was performed by thermal treatment under H₂O atmosphere at 80 °C. The material was evacuated (10⁻⁴ mbar) at 85 °C for 18 h to remove former metal ligand recess and water.

Synthesis of TiO₂@MIL-101: MIL-101 powder and [Ti(O-iP)₄] were placed into a two-chamber-tube separated by a glass frit. The gas-phase loading occurred at 35 °C in a 10⁻⁴ mbar (diffusions pump) dynamic vacuum for 16 h. The resulting bright green powder was instantly processed in hydrolysis to yield TiO₂@MIL-101. The hydrolysis of [Ti(O-iP)₄] was performed by thermal treatment under H₂O atmosphere at 80 °C. The material was evacuated (10⁻⁴ mbar) at 85 °C for 18 h to remove former metal ligand recess and water.

Synthesis of Pd@TiO₂, Pd@MIL-101, and Pd/TiO₂@MIL-101: Amorphous TiO₂, MIL-101, or TiO₂@MIL-101 powder and [(η⁵-C₅H₅)Pd(η³-C₃H₅)] were placed into a two-chamber-tube separated by a glass frit. The gas-phase loading occurred at 25 °C in a 10⁻⁴ mbar (diffusions pump) dynamic vacuum for 16 h. The resulting dark green to black powder (depending on the metal content) was instantly processed in hydrogenolysis to yield Pd@MIL-101 or Pd/TiO₂@MIL-101. The reduction of [(η⁵-C₅H₅)Pd(η³-C₃H₅)] to Pd⁰ was performed under hydrogen atmosphere (50 bar H₂) at 70 °C for 18 h in a Parr Instruments steel autoclave. The material was evacuated (10⁻⁴ mbar) at 85 °C for 18 h to remove former metal ligand recess.

Degradation of RhB: TiO₂ (3.00 mg), Pd@TiO₂ (3.30 mg), MIL-101 (3.00 mg), TiO₂@MIL-101 (3.75 mg, 20 wt% Ti) or Pd/TiO₂@MIL-101 (4.50 mg, 10 wt% Pd, 20 wt% Ti), and 20 mL RhB aqueous solution (2·10⁻⁵ mol L⁻¹) were mixed in a borosilicate glass vessel and stirred for 2 h under exclusion of light at 20 °C. The catalysts were weighted accurate to 0.01 mg. UV-light catalysis was performed by using a UV-F 400F lamp (450 W Hg) with transmission from 290 nm to 420 nm. The distance between the lamp and the borosilicate glass vessels was 20 cm. At given irradiation intervals during the UV-light irradiation, a volume of 1.00 mL of the solution was taken out. The catalyst was separated by centrifugation at 8000 rpm for 8 min. UV/Vis spectra were measured from the supernatant in the range of 400-600 nm. The catalysts were purified

in water three times between the runs of recyclability studies.

Hydrogenation of aromatic ketones: All reduction experiments were performed for 5 h or 20 h in a Parr Instruments steel autoclave with 30 bar H₂. The catalysts amounts between 0.5 mg and 15 mg were weighted accurate to 0.01 mg. Conversion numbers and purity were determined by GC and GC-MS. The catalysts were purified in THF three times between the runs of recyclability studies.

Dehydrogenation of aromatic alcohols: All dehydrogenation experiments were performed for 24, 40, 48, or 60 h in a pressure tube (inner diameter 25.4 mm, length 20.3 cm, volume 28 mL) under dry inert gas atmosphere. The generated H₂ was allowed to leave the reaction system. The catalyst amounts between 0.5 mg and 15 mg were weighted accurate to 0.01 mg. Conversion numbers and purity was determined by GC and GC-MS. The catalysts were purified in THF three times between the runs of recyclability studies.

Acknowledgements

The authors thank the Deutsche Forschungsgemeinschaft (DFG, SFB 840, B1) for funding. Further the help of Florian Puchtler (XRD measurements), Dr. Christine Denner (EDX measurements), and Andreas Gollwitzer (graphical modifications) is gratefully acknowledged. We would like to thank Prof. Dr. Erdmann Spiecker, Dr. Mirza Mackovic, and Yolita Eggeler (Center for Nanoanalysis and Electron Microscopy (CENEM), University of Erlangen-Nuremberg) for providing the HRTEM CM 300 UT (Philips, 300 kV).

4.5 References

- [1] a) B. F. Hoskins, R. Robson, *J. Am. Chem. Soc.* **1989**, *111*, 5962–5964; b) B. F. Abrahams, B. F. Hoskins, D. M. Michail, R. Robson, *Nature* **1994**, *369*, 727–729.
- [2] a) O. M. Yaghi, H. Li, *J. Am. Chem. Soc.* **1995**, *117*, 10401–10402; b) H. Li, M. Eddaoudi, M. O'Keeffe, O. M. Yaghi, *Nature* **1999**, *402*, 276–279.
- [3] a) M. Meilikhov, K. Yusenko, D. Esken, S. Turner, G. Van Tendeloo, R. A. Fischer, *Eur. J. Inorg. Chem.* **2010**, *24*, 3701–3714; b) L. E. Kreno, K. Leong, O. K. Farha, M. Allendorf, R. P. Van Duyne, J. T. Hupp, *Chem. Rev.* **2011**, *112*, 1105–1125; c) A. Morozan, F. Jaouen, *Energy Environ. Sci.* **2012**, *5*, 9269–9290;

- d) H. Furukawa, K. E. Cordova, M. O’Keeffe, O. M. Yaghi, *Science* **2013**, *341*, 1230444; e) J. Liu, L. Chen, H. Cui, J. Zhang, L. Zhang, C.-Y. Su, *Chem. Soc. Rev.* **2014**, *43*, 6011–6061; f) Z. Hu, B. J. Deibert, J. Li, *Chem. Soc. Rev.* **2014**, *43*, 5815–5840.
- [4] a) J. Lee, O. K. Farha, J. Roberts, K. A. Scheidt, S. T. Nguyen, J. T. Hupp, *Chem. Soc. Rev.* **2009**, *38*, 1450–1459; b) Y. Liu, W. Xuan, Y. Cui, *Adv. Mater.* **2010**, *22*, 4112–4135; c) A. Corma, H. García, F. X. Llabrés i Xamena, *Chem. Rev.* **2010**, *110*, 4606–4655; d) A. Dhakshinamoorthy, H. Garcia, *Chem. Soc. Rev.* **2012**, *41*, 5262–5284; e) A. Dhakshinamoorthy, M. Opanasenko, J. Cejka, H. Garcia, *Catal. Sci. Technol.* **2013**, *3*, 2509–2540; f) H. R. Moon, D.-W. Lim, M. P. Suh, *Chem. Soc. Rev.* **2013**, *42*, 1807–1824; g) A. Aijaz, Q. Xu, *J. Phys. Chem. Lett.* **2014**, *5*, 1400–1411; h) Z.-Y. Gu, J. Park, A. Raiff, Z. Wei, H.-C. Zhou, *ChemCatChem* **2014**, *6*, 67–75; i) C. Rösler, R. A. Fischer, *CrystEngComm* **2014**, *17*, 199–217.
- [5] S. Hermes, M.-K. Schröter, R. Schmid, L. Khodeir, M. Muhler, A. Tissler, R. W. Fischer, R. A. Fischer, *Angew. Chem.* **2005**, *117*, 6394–6397; *Angew. Chem. Int. Ed.* **2005**, *44*, 6237–6241.
- [6] a) S. Hermes, F. Schröder, S. Amirjalayer, R. Schmid, R. A. Fischer, *J. Mater. Chem.* **2006**, *16*, 2464–2472; b) S. Hermes, D. Zacher, A. Baunemann, C. Wöll, R. A. Fischer, *Chem. Mater.* **2007**, *19*, 2168–2173; c) M. Müller, O. Lebedev, R. A. Fischer, *J. Mater. Chem.* **2008**, *18*, 5274–5281; d) M. Müller, S. Hermes, K. Köhler, M. W. E. van den Berg, M. Muhler, R. A. Fischer, *Chem. Mater.* **2008**, *20*, 4576–4587; e) F. Schröder, D. Esken, M. Cokoja, M. W. E. van den Berg, O. I. Lebedev, G. Van Tendeloo, B. Walaszek, G. Buntkowsky, H. H. Limbach, B. Chaudret, R. A. Fischer, *J. Am. Chem. Soc.* **2008**, *130*, 6119–6130; f) S. Proch, J. Hermannsdörfer, R. Kempe, C. Kern, A. Jess, L. Seyfarth, J. Senker, *Chem. Eur. J.* **2008**, *14*, 8204–8821; g) M. Meilikhov, K. Yusenko, A. Torrisi, B. Jee, C. Mellot-Draznieks, A. Pöppel, R. A. Fischer, *Angew. Chem.* **2010**, *122*, 6348–6351; *Angew. Chem. Int. Ed.* **2010**, *49*, 6212–6215; h) M. Müller, S. Turner, O. I. Lebedev, Y. Wang, G. Van Tendeloo, R. A. Fischer, *Eur. J. Inorg. Chem.* **2011**, 1876–1887; i) D. Esken, S. Turner, C. Wiktor, S. B. Kalidindi, G. Van Tendeloo, R. A. Fischer, *J. Am. Chem. Soc.* **2011**, *133*, 16370–16373; j) J. Hermannsdörfer, R. Kempe, *Chem. Eur. J.* **2011**, *17*, 8071–8077; k) S. B. Kalidindi, H. Oh, M.

- Hirscher, D. Esken, C. Wiktor, S. Turner, G. Van Tendeloo, R. A. Fischer, *Chem. Eur. J.* **2012**, *18*, 10848–10856; l) D.-W. Lim, J. W. Yoon, K. Y. Ryu, M. P. Suh, *Angew. Chem.* **2012**, *124*, 9952–9955; *Angew. Chem. Int. Ed.* **2012**, *51*, 9814–9817; m) J. Hermannsdörfer, M. Friedrich, N. Miyajima, R. Q. Albuquerque, S. Kümmel, R. Kempe, *Angew. Chem.* **2012**, *124*, 11640–11644; *Angew. Chem. Int. Ed.* **2012**, *51*, 11473–11477; n) J. Hermannsdörfer, M. Friedrich, R. Kempe, *Chem. Eur. J.* **2013**, *19*, 13652–13657.
- [7] a) K. Nakata, A. Fujishima, *J. Photochem. Photobiol., C* **2012**, *13*, 169; b) J. Schneider, M. Matsuoka, M. Takeuchi, J. Zhang, Y. Horiuchi, M. Anpo, D. W. Bahnemann, *Chem. Rev.* **2014**, *114*, 9919.
- [8] a) M. Müller, X. Zhang, Y. Wang, R. A. Fischer, *Chem. Commun.* **2009**, 119–121; b) A. S. Hall, A. Kondo, K. Maeda, T. E. Mallouk, *J. Am. Chem. Soc.* **2013**, *135*, 16276–16279; c) S. Abedi, A. Morsali, *ACS Catal.* **2014**, *4*, 1398–1403; d) C. R. Kim, T. Uemura, S. Kitagawa, *Microporous Mesoporous Mater.* **2014**, *195*, 31–35; e) Y. Hu, Z. Huang, L. Zhou, D. Wang, G. Li, *J. Sep. Sci.* **2014**, *37*, 1482–1488; f) A. V. Vinogradov, H. Zaake-Hertling, E. Hey-Hawkins, A. V. Agafonov, G. A. Seisenbaeva, V. G. Kessler, V. V. Vinogradov, *Chem. Commun.* **2014**, *50*, 10210–10213.
- [9] a) T. Schareina, R. Kempe, *Z. Anorg. Allg. Chem.* **2000**, *626*, 1279–1281; b) T. Schareina, C. Schick, B. F. Abrahams, R. Kempe, *Z. Anorg. Allg. Chem.* **2001**, *627*, 1711–1713; c) T. Schareina, C. Schick, R. Kempe, *Z. Anorg. Allg. Chem.* **2001**, *627*, 131–133.
- [10] G. Férey, C. Mellot-Draznieks, C. Serre, F. Millange, J. Dutour, S. Surblé, I. Margiolaki, *Science* **2005**, *309*, 2040–2042.
- [11] a) H. Liu, Y. Liu, Y. Li, Z. Tang, H. Jiang, *J. Phys. Chem. C* **2010**, *114*, 13362–13369; b) Z. Sun, G. Li, L. Liu, H. Liu, *Catal. Commun.* **2012**, *27*, 200–205.
- [12] F. Wu, L.-G. Qiu, F. Ke, X. Jiang, *Inorg. Chem. Commun.* **2013**, *32*, 5–8.
- [13] a) A. M. Balua, C. S. K. Lin, H. Liu, Y. Li, C. Vargas, R. Luque, *Appl. Catal. A* **2013**, *455*, 261–266; b) M. Saikia, D. Bhuyan, L. Saikia, *New J. Chem.* **2015**, *39*, 64–67.
- [14] a) Y. K. Hwang, D.-Y. Hong, J.-S. Chang, S. H. Jhung, Y.-K. Seo, J. Kim, A. Pan, B. Yuan, Y. Li, D., G. Férey, *Angew. Chem.* **2008**, *120*, 4212–4216; *Angew. Chem. Int. Ed.* **2008**, *47*, 4144–4148; b) A. Henschel, K. Gedrich, R. Kraehnert,

- S. Kaskel, *Chem. Commun.* **2008**, 41924194; c) Y. Pan, B. Yuan, Y. Li, D. He, *Chem. Commun.* **2010**, 46, 2280–2282; d) B. Yuan, Y. Pan, Y. Li, B. Yin, H. Jiang, *Angew. Chem.* **2010**, 122, 4148–4152; *Angew. Chem. Int. Ed.* **2010**, 49, 4054–4058; e) Y. Huang, Z. Lin, R. Cao, *Chem. Eur. J.* **2011**, 17, 12706–12712; f) H. Liu, Y. Li, R. Luque, H. Jiang, *Adv. Synth. Catal.* **2011**, 353, 3107–3113; g) H. Li, Z. Zhu, F. Zhang, S. Xie, H. Li, P. Li, X. Zhou, *ACS Catal.* **2011**, 1, 1604–1612; h) F. G. Cirujano, F. X. Llabrés i Xamena, A. Corma, *Dalton Trans.* **2012**, 41, 4249–4254; i) Y. Huang, S. Liu, Z. Lin, W. Li, X. Li, R. Cao, *J. Catal.* **2012**, 292, 111–117; j) M. Yadav, A. Aijaz, Q. Xu, *Funct. Mater. Lett.* **2012**, 5, 1250039; k) G. Chen, S. Wu, H. Liu, H. Jiang, Y. Li, *Green Chem.* **2013**, 15, 230–235; l) Y. Huang, T. Ma, P. Huang, D. Wu, Z. Lin, R. Cao, *ChemCatChem* **2013**, 5, 1877–1883; m) V. Pascanu, Q. Yao, A. Bermejo Gómez, M. Gustafsson, Y. Yun, W. Wan, L. Samain, X. Zou, B. Martín-Matute, *Chem. Eur. J.* **2013**, 19, 17483–17493; n) D. Zhang, Y. Guan, E. J. M. Hensen, L. Chen, Y. Wang, *Catal. Commun.* **2013**, 41, 47–51; o) F. G. Cirujano, A. Leyva-Pérez, A. Corma, F. X. Llabrés i Xamena, *ChemCatChem* **2013**, 5, 538–549; p) N. Shang, S. Gao, X. Zhou, C. Feng, Z. Wang, C. Wang, *RSC Adv.* **2014**, 4, 54487–54493; q) V. Pascanu, P. R. Hansen, A. Bermejo Gómez, C. Ayats, A. E. Platero-Prats, M. J. Johansson, M. À. Pericàs, B. Martín-Matute, *ChemSusChem* **2015**, 8, 123–130; r) M. Annapurna, T. Parsharamulu, P. Vishnuvardhan Reddy, M. Suresh, P. R. Likhar, M. Lakshmi Kantam, *Appl. Organomet. Chem.* **2015**, 29, 234–239; s) F. Carson, V. Pascanu, A. Bermejo Gómez, Y. Zhang, A. E. Platero-Prats, X. Zou, B. Martín-Matute *Chem. Eur. J.* **2015**, 21, 10896–10902.
- [15] a) A. Aijaz, A. Karkamkar, Y. J. Choi, N. Tsumori, E. Rönnebro, T. Autrey, H. Shioyama, Q. Xu, *J. Am. Chem. Soc.* **2012**, 134, 13926–13929; b) H. Khajavi, H. A. Stil, H. P. C. E. Kuipers, J. Gascon, F. Kapteijn, *ACS Catal.* **2013**, 3, 2617–2626; c) H. Pan, X. Li, D. Zhang, Y. Guan, P. Wu, *J. Mol. Catal. A: Chem.* **2013**, 377, 108–114; d) W. Du, G. Chen, R. Nie, Y. Li, Z. Hou, *Catal. Commun.* **2013**, 41, 56–59.
- [16] T. Van Vu, H. Kosslick, A. Schulza, J. Harloff, E. Paetzold, J. Radnik, U. Kragl, G. Fulda, C. Janiak, N. D. Tuyen, *Microporous Mesoporous Mater.* **2013**, 177, 135–142.

- [17] a) X. Gu, Z.-H. Lu, H.-L. Jiang, T. Akita, Q. Xu, *J. Am. Chem. Soc.* **2011**, *133*, 11822–11825; b) J. Long, H. Liu, S. Wu, S. Liao, Y. Li, *ACS Catal.* **2013**, *3*, 647–654; c) M. Yadav, Q. Xu, *Chem. Commun.* **2013**, *49*, 3327–3329; d) C. M. Granadeiro, P. Silva, V. K. Saini, F. A. A. Paz, J. Pires, L. Cunha-Silva, S. S. Balula, *Catal. Today* **2013**, *218–219*, 35–42; e) Q.-L. Zhu, J. Li, Q. Xu, *J. Am. Chem. Soc.* **2013**, *135*, 10210–10213; f) N. Cao, L. Yang, H. Dai, T. Liu, J. Su, X. Wu, W. Luo, G. Cheng, *Inorg. Chem.* **2014**, *53*, 10122–10128; g) H. Dai, N. Cao, L. Yang, J. Su, W. Luo, G. Cheng, *J. Mater. Chem. A* **2014**, *2*, 11060–11064; h) N. Cao, J. Su, W. Luo, G. Cheng, *Int. J. Hydrogen Energy* **2014**, *39*, 9726–9734; i) J. Li, Q.-L. Zhu, Q. Xu, *Chem. Commun.* **2014**, *50*, 5899–5901; j) Jun Li, Q.-L. Zhu, Q. Xu, *Catal. Sci. Technol.* **2015**, *5*, 525–530; k) H. Liu, R. Fang, Z. Li, Y. Li, *Chem. Eng. Sci.* **2015**, *122*, 350–359; l) Y.-Z. Chen, Y.-X. Zhou, H. Wang, J. Lu, T. Uchida, Q. Xu, S.-H. Yu, H.-L. Jiang, *ACS Catal.* **2015**, *5*, 2062–2069; m) J. Li, Q.-L. Zhu, Q. Xu, *Catal. Sci. Technol.* **2015**, *5*, 525–530.
- [18] a) L. Bromberg, Y. Diao, H. Wu, S. A. Speakman, T. A. Hatton, *Chem. Mater.* **2012**, *24*, 1664–1675; b) A. El R. S. Khder, H. M. A. Hassan, M. S. El-Shall, *Appl. Catal., A* **2014**, *487*, 110–118; c) A. Herbst, A. Khutia, C. Janiak, *Inorg. Chem.* **2014**, *53*, 7319–7333; d) Y.-X. Zhou, Y.-Z. Chen, Y. Hu, G. Huang, S.-H. Yu, H.-L. Jiang, *Chem. Eur. J.* **2014**, *20*, 14976–14980.
- [19] a) C. Gunanathan, D. Milstein, *Science* **2013**, *341*, 1229712; b) M. Trincado, D. Banerjee, H. Grützmacher, *Energy Environ. Sci.* **2014**, *7*, 2464–2503.
- [20] a) C. W. Jung, P. E. Garrou, *Organometallics* **1982**, *1*, 658–666; b) J. Zhang, M. Gandelman, L. J. W. Shimon, H. Rozenberg, D. Milstein, *Organometallics* **2004**, *23*, 4026–4033; c) K. Shimizu, K. Sugino, K. Sawabe, A. Satsuma, *Chem. Eur. J.* **2009**, *15*, 2341–2351; d) M. Nielsen, A. Kammer, D. Cozzula, H. Junge, S. Gladiali, M. Beller, *Angew. Chem.* **2011**, *123*, 9767–9771; *Angew. Chem. Int. Ed.* **2011**, *50*, 9593–9597; e) J. Zhang, E. Balaraman, G. Leitus, D. Milstein, *Organometallics* **2011**, *30*, 5716–5724; f) D. Spasyuk, S. Smith, D. G. Gusev, *Angew. Chem.* **2012**, *124*, 2826–2829; *Angew. Chem. Int. Ed.* **2012**, *51*, 2772–2775; g) R. Kawahara, K.-i. Fujita, R. Yamaguchi, *Angew. Chem.* **2012**, *124*, 12962–12966; *Angew. Chem. Int. Ed.* **2012**, *51*, 12790–12794; h) G. Zhang, K. V. Vasudevan, B. L. Scott, S. K. Hanson, *J. Am. Chem. Soc.* **2013**, *135*, 8668–8681; i) E. Balaraman, E. Khaskin, G. Leitus, D. Milstein, *Nat. Chem.* **2013**, *5*, 122–

- 125; j) Y. Sawama, K. Morita, S. Asai, M. Kozawa, S. Tadokoro, J. Nakajima, Y. Monguchi, H. Sajiki, *Adv. Synth Catal.* **2015**, 357, 1205–1210.
- [21] Y. Tatsuno, T. Yoshida, Seiotsuka, N. Al-Salem, B. L. Shaw, *Inorganic Synthesis*, Vol. 19 (Ed.: D. F. Shriver) Wiley-VCH, Weinheim, Germany **1979**, pp. 220–223.

4.6 Supporting Information

Experimental

Reactants and solvents: All manipulations of air sensitive products were carried out under dry and oxygen-free argon atmosphere (Schlenk techniques) or in a nitrogen-filled glovebox (mBraun 120G) with a high-capacity recirculator (below 0.1 ppm of oxygen and water). Manipulations with light sensitive substances were carried out under exclusion of light. N-hexane and thf were distilled from sodium benzophenone ketyl. 1-Phenylethanol C₈H₁₀O, 1-(2-methoxyphenyl)ethanol C₉H₁₂O₂, 1-(2-methylphenyl)ethanol C₉H₁₂O, 1-(4-fluorophenyl)ethanol C₈H₈FO, 1-(4-methoxyphenyl)ethanol C₉H₁₂O₂, 1-(4-methylphenyl)ethanol C₉H₁₂O, 1-phenyl-1-pentanol C₁₁H₁₆O, 1-phenyl-1-propanol C₉H₁₂O, 4-Methylbenzyl alcohol C₈H₁₀O, acetophenone C₈H₈O, allylpalladium(II) chloride dimer [(C₃H₅)₂Pd₂Cl₂], benzophenone C₁₃H₁₀O, benzyl alcohol C₇H₈O, chromium(III) nitrate nonahydrate [Cr(NO₃)₃·9H₂O], diphenylmethanol C₁₃H₁₂O, ethanol C₂H₆O, hydrofluoric acid HF, n-dodecane C₁₂H₂₆, Pd@AC, Pd@Al₂O₃, Pd@SiO₂, rhodamine B C₂₈H₃₁ClN₂O₃, sodium cyclopentadienide NaC₅H₅, terephthalic acid C₆H₄(COOH)₂ and titanium(IV) isopropoxide [Ti(OCH(CH₃)₂)₄] were obtained commercially from Sigma-Aldrich, ABCR or Acros Organics and used without further purification. The products [(η⁵-C₅H₅)Pd(η³-C₃H₅)]^[S1] and MIL-101 (Cr) ^[S2] were prepared according to published procedures.

Characterization: ¹H NMR spectra were recorded with a Varian Unity 300 MHz spectrometer. Chemical shifts given in ppm were recorded at 25 °C and are referenced using CDCl₃ as internal standard. EDX measurements were performed with a Zeiss 1540 EsB Cross beam, equipped with a Thermo Noran System Six EDX-system. Elemental analysis was performed by standard protocols employing microwave assisted digestion in HNO₃/HCl/H₃PO₄/(BF₄)⁻H⁺ and inductively coupled plasma optical emission spectrometry using a Varian Vista-Pro radial. FT-IR measurements were performed at a

Perkin-Elmer FT-IR-Spectrum 100 over a range from 4000 cm^{-1} to 500 cm^{-1} . GC analyses were performed using an Agilent Technologies 6850 gas chromatograph equipped with a flame ionisation detector (FID) and a MN Optima 17 capillary column (30.0 m x 0.32 mm x 0.25 μm) using n-dodecane as internal standard and THF as solvent. Gas mixtures were analysed using a Agilent special Plot and Molsieve capillary column (30.0 m x 0.32 mm x 0.25 μm). GC-MS analyses were performed using an Agilent Technologies 6890 gas chromatograph with a MN-MS HP-5 capillary column (30.0 m x 0.32 mm x 0.25 μm) and a coupled mass spectrometer as detector. Nitrogen physisorption isotherms were determined at -196 $^{\circ}\text{C}$ using a Quantachrome Nova 2000e apparatus. Specific surface areas were calculated by using p/p_0 -values from 0.05-0.25 by BET. Specific total pore volumes were measured by the DFT calculations (N_2 at -196 $^{\circ}\text{C}$ on silica (cylindr. pore, NLDFT equilibrium model)). TEM measurements were carried out by using a LEO 9220 (Carl Zeiss, 200 kV). The samples were suspended in chloroform and sonicated for 5 min. 2 μL of the suspension were placed on a CF200-Cu-grid (Electron Microscopy Sciences) and allowed to dry. HRTEM measurements were performed using a CM 300 UT (Philips, 300 kV). The samples were suspended in chloroform and sonicated for 5 min. 2 μL of the suspension were placed on a CF200-Cu-grid with a lacey carbon film (Electron Microscopy Sciences) and allowed to dry. TGA analysis were performed from 30 $^{\circ}\text{C}$ to 450 $^{\circ}\text{C}$ (5 $^{\circ}\text{C min}^{-1}$) using a Mettler TGA/SDTA 85 under air. UV-Vis spectra (liquid) were taken for supernatants of the reaction solutions in range of 400 nm to 600 nm using a CARY 300 (Agilent Technologies) with Scan-software and PS-cuvettes (12.5 mm x 12.5 mm x 45 mm). Solid state UV-Vis spectra were measured using a CARY 300 with an Ulbricht sphere in the range of 200 nm to 800 nm. XRD diffractograms were recorded using a STOE STADI-P-diffractometer ($\text{Cu}_{K\alpha}$ radiation, 1,54178 \AA) in θ -2 θ -geometry with a position sensitive detector.

Synthesis of MIL-101: $[\text{Cr}(\text{NO}_3)_3 \cdot 9 \text{H}_2\text{O}]$ (640 mg, 1.60 mmol), H_2BDC (265 mg, 1.60 mmol), HF 40 wt.-% (10 μL , 0.228 mmol) and de-ionized H_2O (8.00 mL) were combined and sealed in a 23 mL Teflon-lined hydrothermal autoclave. The mixture was heated for 1 h at 80 $^{\circ}\text{C}$ (heating rate: 2.7 $^{\circ}\text{C min}^{-1}$) and for 7.45 h at 220 $^{\circ}\text{C}$ (4.7 $^{\circ}\text{C min}^{-1}$). The reaction mixture was cooled down fast to 160 $^{\circ}\text{C}$ and slowly to 30 $^{\circ}\text{C}$ (cooling rate: 5.4 $^{\circ}\text{C h}^{-1}$). Excessively crystallized H_2BDC was removed by filtration over a pore 3 filter. The green product was separated from the reaction solution by centrifugation

(2000 rpm, 45 min). The MIL-101 was refluxed in ethanol/water (90/10 vol.-%) for 14 h and centrifugalized (1800 rpm, 45 min) three times to remove grimaldiite (α -CrOOH) impurities. Repetitive differential centrifugation in ethanol/water (1800 rpm, 5 min) was also used to separate MIL-101 crystals with different size distribution. The different MIL-101 fractions were dried under vacuum (10^{-4} mbar, 85 °C). (BET: 2900 m² g⁻¹; XRD (2θ (°), intensity (%)): 2.78 (56), 3.26 (100), 3.41 (44), 3.94 (19), 4.30 (11), 4.84 (16), 5.13 (32), 5.59 (16), 5.85 (22), 6.24 (5), 6.48 (5), 8.10 (7), 8.40 (22), 8.58 (11), 8.86 (15), 9.02 (28), 9.71 (5), 9.86 (5), 10.30 (6), 11.22 (4), 16.50 (6)).

Synthesis of $[(\eta^5\text{-C}_5\text{H}_5)\text{Pd}(\eta^3\text{-C}_3\text{H}_5)]$: A solution of NaCp (1.50 g, 17.1 mmol) in 40 mL of THF was added dropwise to a solution of $[(\text{C}_3\text{H}_5)_2\text{Pd}_2\text{Cl}_2]$ (2.50 g, 6.83 mmol) in 50 mL of THF at -78 °C. The reaction mixture was stirred for 10 min at -78 °C, warmed up to room temperature and stirred for another 15 min at room temperature. The solvent was removed under vacuum and the resulting residue was dissolved in n-hexane. The NaCl was removed by cannula filtration and the solvent was removed under vacuum. The red residue was sublimated under vacuum (10^{-4} mbar) and the obtained red crystals were stored under exclusion of light and air at -30 °C. (Yield 2.50 g, 11.76 mmol (86 %)). ¹H NMR (300 MHz, CDCl₃): δ (ppm) 1.74 (d, ³J_{HH} = 9.83 Hz, 2 H, CH₂), 3.11 (d, ³J_{HH} = 6.10 Hz, 2 H, CH₂), 4.47 (m, 1 H, CH), 5.23 (s, 5 H, C₅H₅).

Synthesis of amorphous TiO₂: The precursor compound $[\text{Ti}(\text{O-iP})_4]$ was processed in hydrolysis to yield amorphous TiO₂. The hydrolysis of $[\text{Ti}(\text{O-iP})_4]$ was performed by thermal treatment under H₂O atmosphere at 80 °C in order to maintain. The material was evacuated (10^{-4} mbar) at 85 °C for 18 h in order to remove former metal ligand recess and water.

Synthesis of TiO₂@MIL-101: MIL-101 powder and $[\text{Ti}(\text{O-iP})_4]$ were placed into a two-chamber-tube separated by a glass frit. The gas-phase loading occurred at 35 °C in a 10^{-4} mbar (diffusions pump) dynamic vacuum for 16 h. The resulting bright green powder was instantly processed in hydrolysis to yield TiO₂@MIL-101. The hydrolysis of $[\text{Ti}(\text{O-iP})_4]$ was performed by thermal treatment under H₂O atmosphere at 80 °C. The material was evacuated (10^{-4} mbar) at 85 °C for 18 h in order to remove former metal ligand recess and water.

Synthesis of Pd@TiO₂, Pd@MIL-101, and Pd/TiO₂@MIL-101: Amorphous TiO₂, MIL-101, or TiO₂@MIL-101 powder and $[(\eta^5\text{-C}_5\text{H}_5)\text{Pd}(\eta^3\text{-C}_3\text{H}_5)]$ were placed into a two-chamber-tube separated by a glass frit. The gas-phase loading occurred at 25 °C in a

10^{-4} mbar (diffusions pump) dynamic vacuum for 16 h. The resulting dark green to black powder (depending on the metal content) was instantly processed in hydrogenolysis to yield Pd@MIL-101 or Pd/TiO₂@MIL-101. The reduction of $[(\eta^5\text{-C}_5\text{H}_5)\text{Pd}(\eta^3\text{-C}_3\text{H}_5)]$ to Pd⁰ was performed under hydrogen atmosphere (50 bar H₂) at 70 °C for 18 h in a Parr Instruments steel autoclave. The material was evacuated (10^{-4} mbar) at 85 °C for 18 h in order to remove former metal ligand recess.

Degradation of RhB: 3.00 mg of TiO₂, 3.30 mg of Pd@TiO₂, 3.00 mg of MIL-101, 3.75 mg of TiO₂@MIL-101 (20 wt.-% Ti), or 4.5 mg of Pd/TiO₂@MIL-101 (10 wt.-% Pd, 20 wt.-% Ti) and 20 mL RhB aqueous solution ($2 \cdot 10^{-5}$ mol L⁻¹) was mixed in a borosilicate glass vessel and stirred for 2 h under exclusion of light at 20 °C. The catalysts were weighted accurate to 0.01 mg. UV-catalysis was performed using a UV-F 400F lamp (450 W Hg) with transmission from 290 nm to 420 nm. The distance between the lamp and the borosilicate glass vessels was 20 cm. At given irradiation intervals during the UV irradiation, 1.00 mL of the solution was taken out. The catalyst was separated by centrifugation at 8000 rpm for 8 min. UV-Vis spectra were measured from the supernatant in the range of 400 nm to 600 nm. The catalysts were purified in water three times between the runs of recyclability studies.

Hydrogenation of aromatic ketones: All reduction experiments were carried out for 5 h or 20 h in a Parr Instruments steel autoclave with 30 bar H₂. The catalysts amounts between 0.5 mg and 15 mg were weighted accurate to 0.01 mg. Conversion numbers and purity was determined by GC and GC-MS. The catalysts were purified in THF three times between the runs of recyclability studies.

Dehydrogenation of aromatic alcohols: All dehydrogenation experiments were carried out for 24 h, 40 h 48 h or 60 h in a pressure tube (inner diameter 25.4 mm, length 20.3 cm, volume 28 mL) under dry inert gas atmosphere. The generated H₂ was allowed to leave the reaction system. The catalyst amounts between 0.5 mg and 15 mg were weighted accurate to 0.01 mg. Conversion numbers and purity was determined by GC and GC-MS. The catalysts were purified in THF three times between the runs of recyclability studies.

Characterization

MIL-101

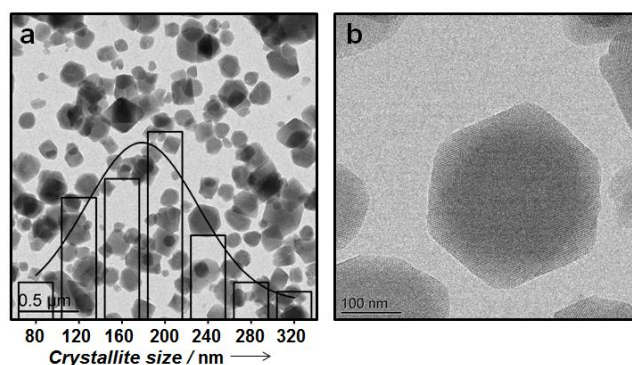


Figure S 1. TEM images of MIL-101 with a narrow crystallite-size distribution between 100 nm and 300 nm adjusted by the amount of HF during the hydrothermal synthesis (a). The typical octahedral shape of the PCP/MOF crystallites was observed (b).

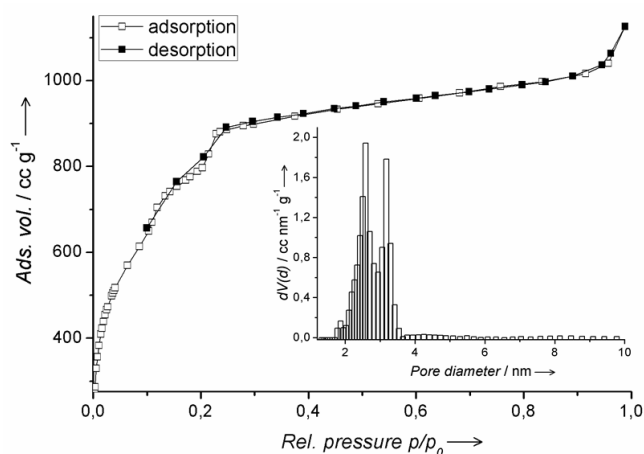


Figure S 2. N₂ physisorption measurements of MIL-101. Specific surface area of 2900 m²g⁻¹ was determined by BET (0.02-0.25 p/p₀). Characteristic pore diameters were determined by DTF calculations.

BET

Table S 1. Specific surface areas of TiO₂@MIL-101, Pd@MIL-101, and Pd/TiO₂@MIL-101 with different metal contents (calculated) determined by BET (0.02-0.25 p/p₀). The remaining specific surface area of the samples decreases with rising Pd and Ti contents.

| sample | metal content (wt.-%) | | surface area (m ² g ⁻¹) |
|------------------------------|-----------------------|----|--|
| | Pd | Ti | |
| TiO ₂ @MIL-101 | - | 5 | 2300 |
| | - | 10 | 1800 |
| | - | 15 | 1550 |
| | - | 20 | 1200 |
| | - | 30 | 1050 |
| Pd@MIL-101 | 10 | - | 1900 |
| Pd/TiO ₂ @MIL-101 | 10 | 5 | 1600 |
| | 10 | 10 | 1250 |
| | 10 | 15 | 1000 |
| | 10 | 20 | 900 |
| | 10 | 30 | 700 |

FT-IR

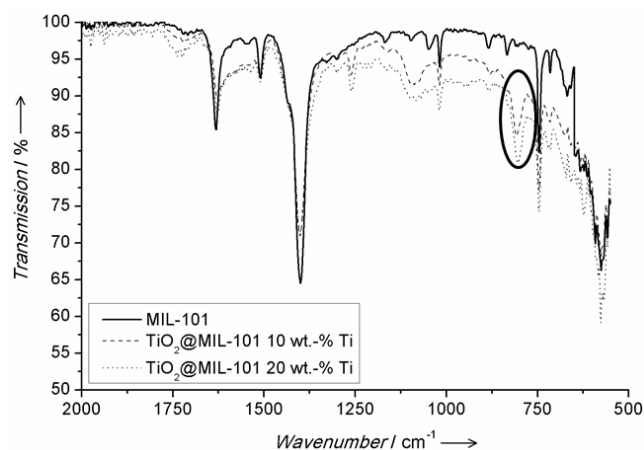


Figure S 3. FT-IR measurements of TiO₂@MIL-101 with Ti contents of 10 and 20 wt.-% in comparison to pure MIL-101. The incorporation of titania does not affect the characteristic lattice vibrations of the metal-organic host system. The band located at 780 cm⁻¹ is attributed to Ti-O stretching and Ti-O-Ti bridging stretching modes.

Solid state UV-Vis

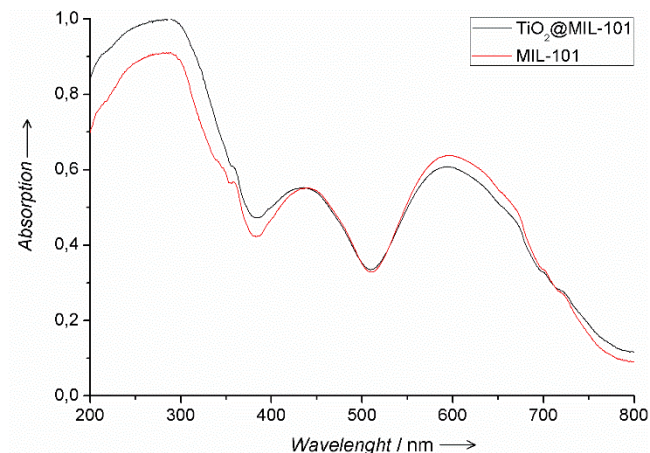


Figure S 4. Solid state UV-Vis measurement of TiO_2 @MIL-101 (15 wt.-% Ti) and MIL-101. The incorporation of amorphous TiO_2 increases the UV absorption of MIL-101.

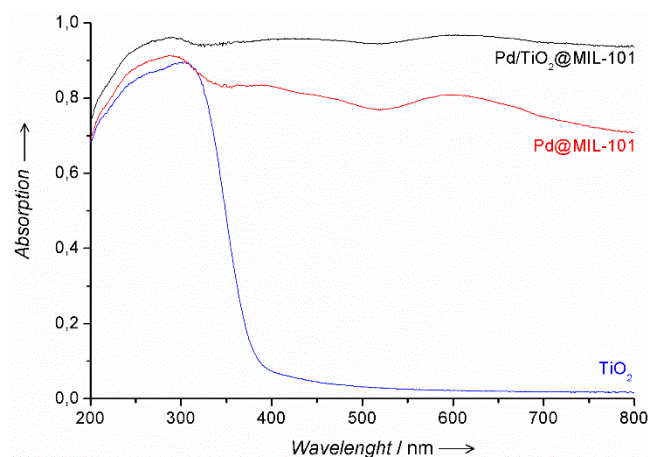


Figure S 5. Solid state UV-Vis measurement of amorphous hydrolyzed $[\text{Ti}(\text{O-iP})_4]$ (TiO_2) shows characteristic UV absorption below 400 nm. Black colored Pd-loaded MIL-101 or TiO_2 @MIL-101 absorbs irradiated light over the entire range from 200 nm to 800 nm.

TEM

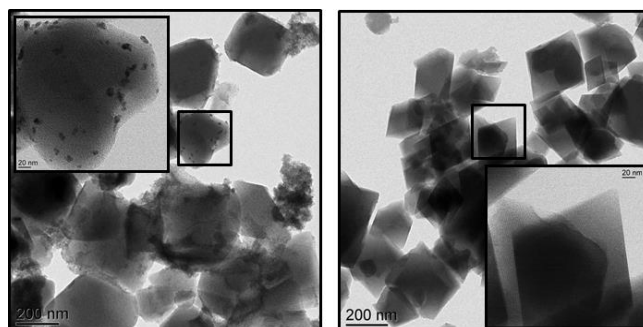


Figure S 6. TEM analysis of TiO₂@MIL-101 with 30 wt.-% Ti (left) and 5 wt.-% Ti (right) indicates the limited capacity of the metal-organic host structure regarding to homogeneous TiO₂ loadings with high Ti contents. High precursor contents lead to the formation of TiO₂ around the metal-organic host structure. Titanium dioxide inside the cavities of MIL-101 exhibits low contrast to the host structure and is hard to visualize in TEM analysis.

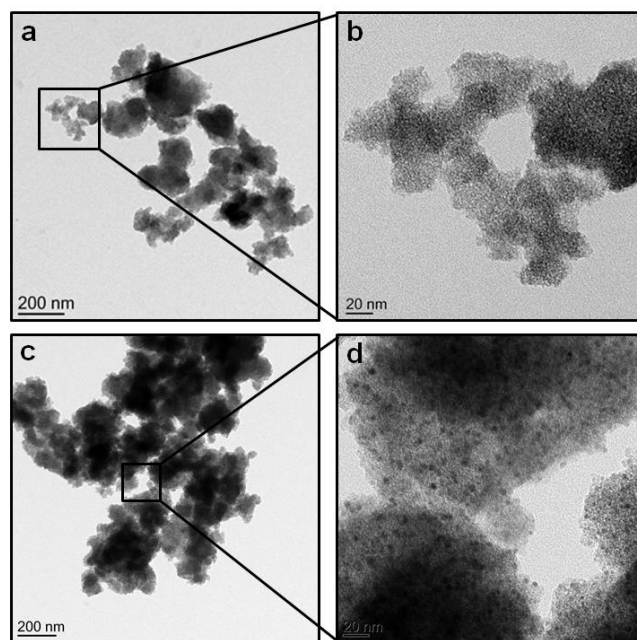


Figure S 7. TEM images of amorphous TiO₂ (a, b) prepared by controlled hydrolysis of [Ti(O-iP)₄] and Pd@TiO₂ (c, d) prepared by MOCVD infiltration of the Pd precursor followed by subsequent hydrogenolysis.

TGA

The thermogravimetric analysis (TGA) of Pd/TiO₂@MIL-101, TiO₂@MIL-101, Pd@MIL-101, and MIL-101 identifies a quite similar behavior in comparison to Pd@MIL-101 and MIL-101. Up to 230 °C, no serious weight loss or release of water (weight loss < 7 %) was observed for Pd/TiO₂@MIL-101 and TiO₂@MIL-101. The thermal induced decomposition of the TiO₂-loaded compounds started at about 230 °C whereas the beginning decomposition of Pd@MIL-101 and MIL-101 was identified at 200 °C (Figure S 8).

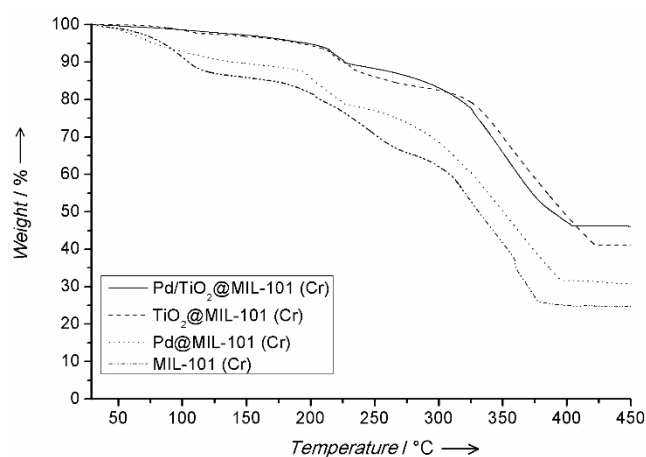


Figure S 8. TGA analysis of Pd/TiO₂@MIL-101, TiO₂@MIL-101, and Pd@MIL-101 (10 wt.-% Pd, 20 wt.-% Ti) in comparison to pure MIL-101 (all compounds as synthesized).

XRD

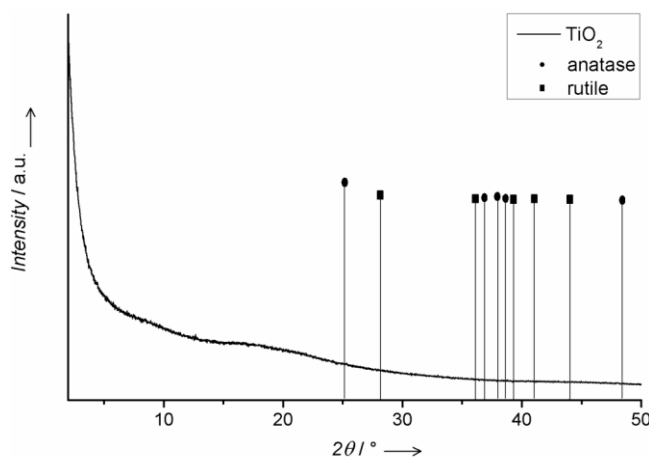


Figure S 9. XRD analysis of hydrolyzed [Ti(O-iP)₄] indicates amorphous titanium dioxide. The hydrolysis was performed under H₂O-atmosphere analogous to the preparation of TiO₂@MIL-101.

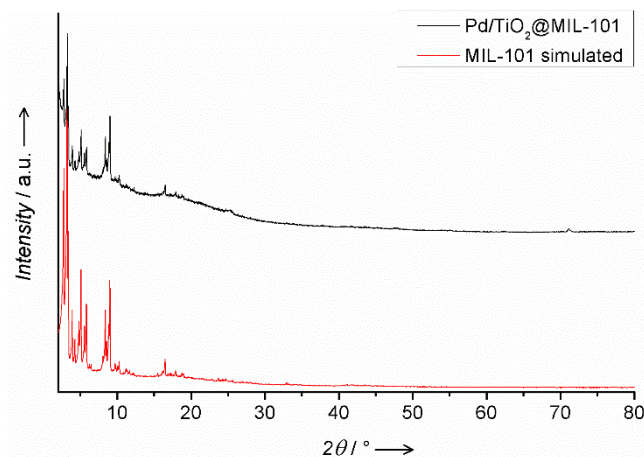
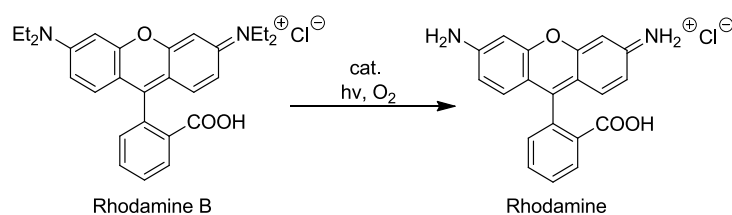


Figure S 10. XRD measurement of Pd/TiO₂@MIL-101 (10 wt.-% Pd, 20 wt.-% Ti) catalyst used for the hydrogenation of benzophenone at 140 °C for five times in comparison to the representative MIL-101 reflexes

Degradation of RhB



Scheme S 1. Photocatalytic N-deethylation of RhB in the presence of O₂ leads to the reduction of the characteristic absorption maximum of the dye at 552 nm.

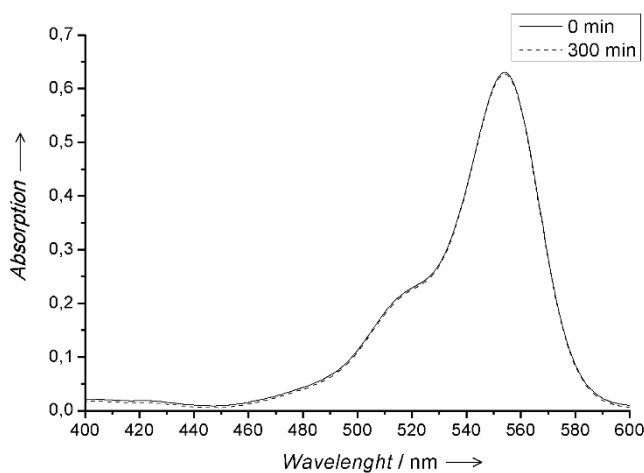


Figure S 11. The concentration of RhB in presence of Pd/TiO₂@MIL-101 (10 wt.-% Pd, 20 wt.-% Ti) does not change under exclusion of light proven by UV-Vis measurements.

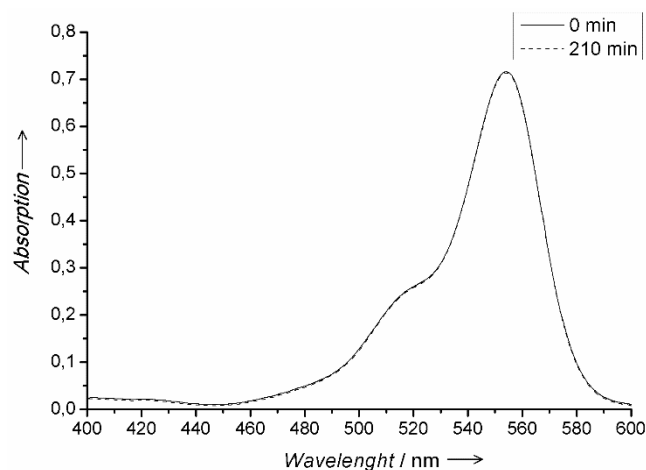


Figure S 12. The concentration of RhB in presence of external irradiated UV light in absence of the catalyst does not change proven by UV-Vis measurements.



Figure S 13. Decreasing RhB colour of the supernatant in presence of Pd/TiO₂@MIL-101 before the exposure to UV-light (left, $c/c_0 = 100\%$) and after 360 min under UV-light irradiation (right, $c/c_0 = 12\%$).

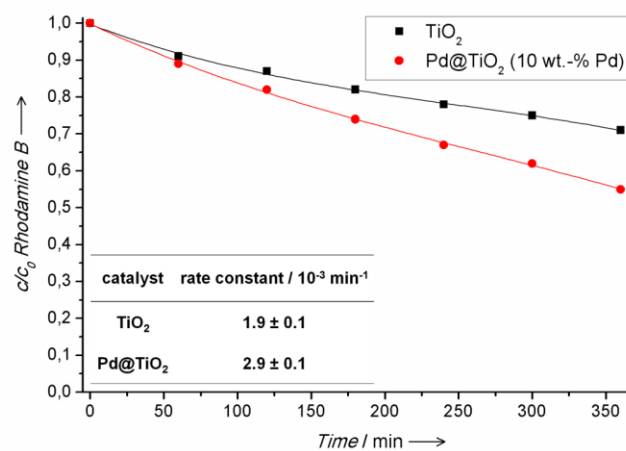


Figure S 14. Degradation of RhB by TiO₂ and Pd@TiO₂ (10 wt.-% Pd) under irradiation of UV-light with normalized catalyst amounts referred to the TiO₂ amount. c and c_0 are the intensities of the absorbance peak at 552 nm at the reaction time and the initial time.

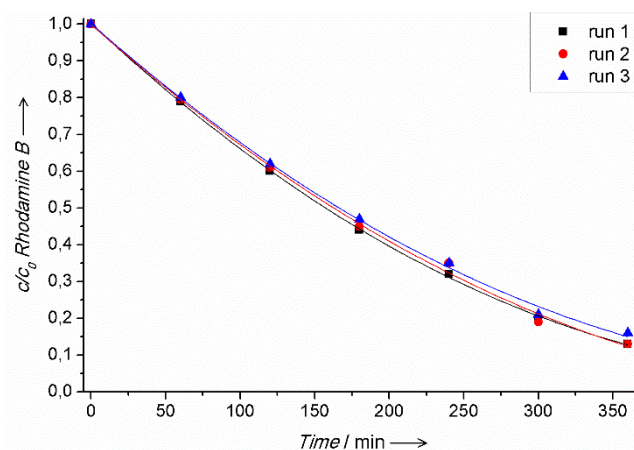


Figure S 15. Degradation of RhB by Pd/TiO₂@MIL-101 (10 wt.-% Pd, 20 wt.-% Ti) under the irradiation of UV-light. c and c_0 are the intensities of the absorbance peak at 552 nm at the reaction time and the initial time. The catalyst was reused three times with constant photocatalytic activity.

Thermal Treatment at 230 °C

In order to investigate the stability of the titanium dioxide featured compounds Pd/TiO₂@MIL-101 and TiO₂@MIL-101 and to compare them to Pd@MIL-101 and MIL-101, all four materials were thermally treated at 230 °C for 14 h. The compounds without TiO₂ showed a serious decomposition of the metal-organic network system. The mass loss of Pd@MIL-101 and MIL-101 during the thermal treatment at 230 °C is illustrated in Supporting Information, Table S 2 and goes along with a drastic decrease of the specific surface area about 70 %. In contrast, the TiO₂-reinforced catalyst materials Pd/TiO₂@MIL-101 and TiO₂@MIL-101 only indicated a partial decomposition of the host material. The resulting mass loss and the reduction of the specific surface areas were less severe.

In addition, the drastic decomposition of the MIL-101 host structure of the TiO₂-free compounds could be verified by XRD. The collapse of the MIL-101 crystallites resulted in changing reflex patterns. The characteristic reflexes of MIL-101 were significantly reduced for MIL-101 and especially for Pd@MIL-101 induced by the thermal liability. The partial decomposition of the TiO₂-containing compounds resulted in slightly

decreasing intensities of the reflex pattern of Pd/TiO₂@MIL-101 and TiO₂@MIL-101 (Supporting Information, Figure S 16).

The decomposition of the MIL-101 crystallites during the thermal treatment at 230 °C was accessorially identified by TEM analysis. Pd@MIL-101 and MIL-101 showed an intense destruction of the host material. Furthermore, the agglomeration of the palladium particles was identified for Pd@MIL-101 (Figure S 17, 18). The thermal induced collapse of the MIL-101 network is clearly reduced in case of the TiO₂-loaded compounds. The metal-organic framework only exhibited a slight decomposition on the outer spheres of the crystallites without any particle agglomeration (Figure S 19, 20).

Table S 2. Mass lost and surface area decrease of thermally treated Pd/TiO₂@MIL-101, TiO₂@MIL-101, Pd@MIL-101, and MIL-101 at 230 °C for 14 h.

| Sample | Mass loss (%) | Specific surface area decrease (%) ^[d] |
|---|---------------|---|
| Pd/TiO ₂ @MIL-101 ^[a] | 21 | 22 |
| TiO ₂ @MIL-101 ^[b] | 17 | 19 |
| Pd@MIL-101 ^[c] | 46 | 69 |
| MIL-101 | 57 | 71 |

[a] 10 wt.-% Pd, 20 wt.-% Ti. [b] 20 wt.-% Ti. [c] 10 wt.-% Pd. [d] determined by BET.

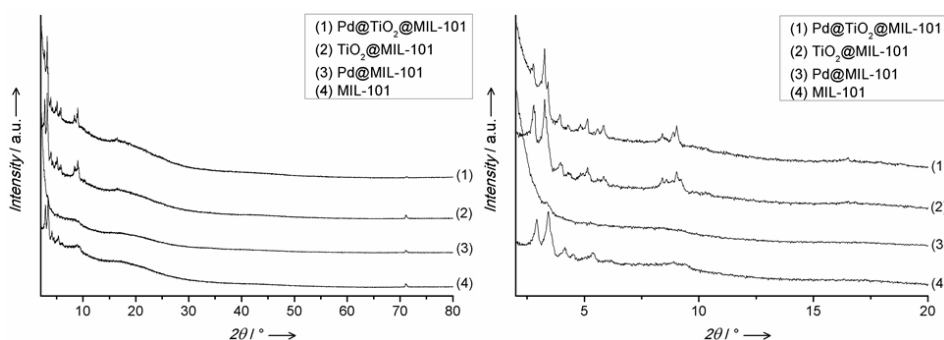


Figure S 16. X-ray powder diffraction analysis of thermally treated catalysts (230 °C, 20 h). The temperature induced destruction of the metal-organic host structure was more profound for unreinforced Pd@MIL-101 (10 wt.-% Pd) and MIL-101 in comparison to Pd/TiO₂@MIL-101.

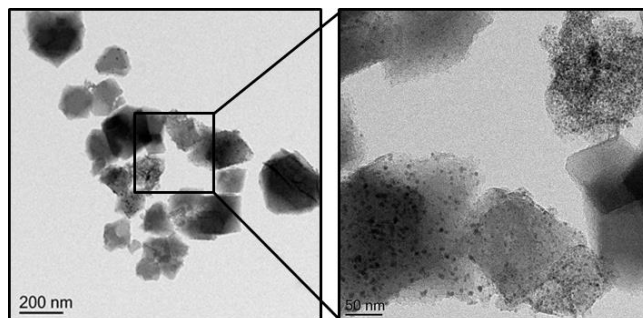


Figure S 17. TEM images of Pd@MIL-101 thermally treated at 230 °C for 14 h.

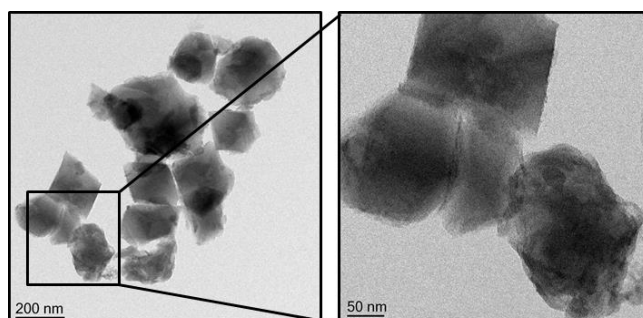


Figure S 18. TEM images of MIL-101 thermally treated at 230 °C for 14 h.

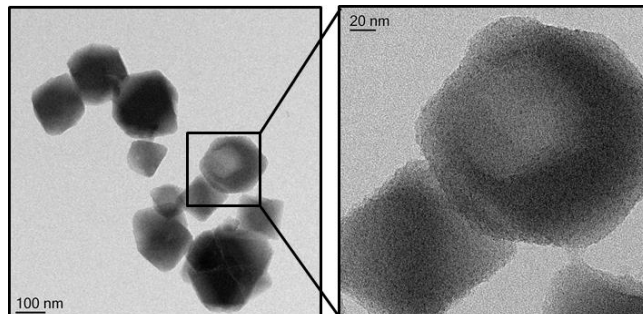


Figure S 19. TEM images of Pd/TiO₂@MIL-101 thermally treated at 230 °C for 14 h.

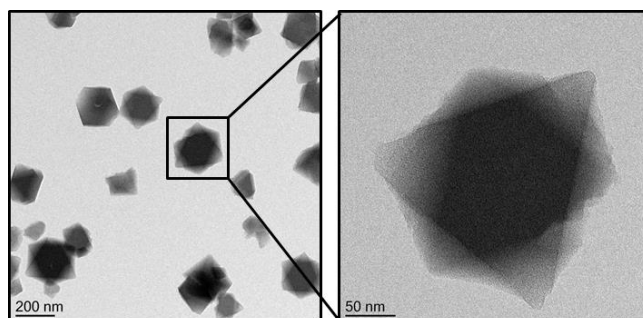


Figure S 20. TEM images of TiO₂@MIL-101 thermally treated at 230 °C for 14 h.

- [S1] Y. Tatsuno, T. Yoshida, Seitsuka, N. Al-Salem, B. L. Shaw in *Inorganic Synthesis, Vol. 19* (Ed.: D. F. Shriver) Wiley-VCH, Weinheim, Germany **1979**, pp. 220–223.
- [S2] J. Hermannsdörfer, M. Friedrich, R. Kempe, *Chem. Eur. J.* **2013**, *19*, 13652–13657.

5 A Plasmonic Colloidal Photocatalyst Composed of a Metal–Organic Framework Core and a Gold/Anatase Shell for Visible-Light-Driven Wastewater Purification from Antibiotics and Hydrogen Evolution

Dominic Tilgner and Rhett Kempe^{*[a]}

[a] Inorganic Chemistry II – Catalyst Design, Universität of Bayreuth, Universitätsstraße 30, 95440 Bayreuth (Germany).

Published in *Chem. Eur. J.* **2017**, *23*, 3184–3190.

Keywords: dye degradation; metal-organic frameworks; photocatalysis; plasmonic materials; water splitting

Abstract: Porous coordination polymers (PCP) or metal-organic frameworks (MOF) are promising materials for the generation of photocatalytically active composite materials. Here, a novel synthesis concept is reported, which permits the formation of PCP/MOF-core–Au/anatase-shell materials. These materials are photocatalysts for wastewater purification and hydrogen generation from water under visible-light illumination. MIL-101 (Cr) is utilized as the core material, which directs the size of the core–shell compound and ensures the overall stability. In addition, its excellent reversible large molecule sorption behavior allows the materials synthesis. The crystalline anatase shell is generated stepwise under mild conditions using titanium(IV) isopropoxide as a precursor. The high degree of control of the vapor phase deposition process permits the precise anatase shell formation. The generation of plasmonic active gold particles on the TiO₂ shell leads to an efficient material for visible-light driven photocatalysis with a higher activity than gold-decorated P25 (Degussa).

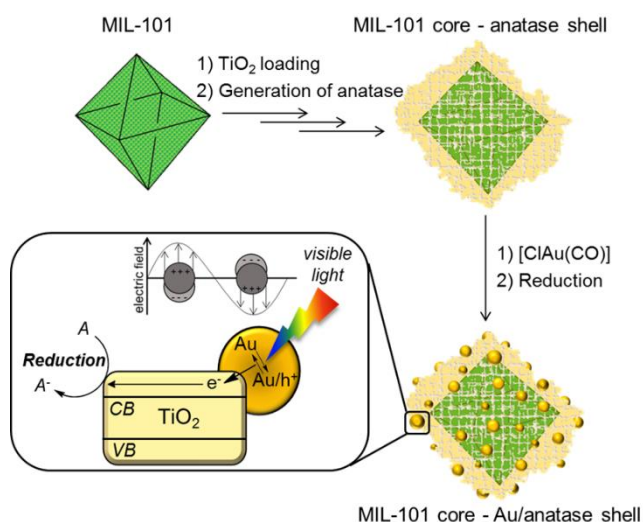
5.1 Introduction

Porous coordination polymers (PCPs)^[1] or metal–organic frameworks (MOFs)^[2] are regularly ordered crystalline materials built up of inorganic building units (metal ions or

clusters generally designated as secondary building units) connected by multidentate organic linkers. The resulting structural flexibility has led to a constantly increasing number of PCP/MOF compounds combining large specific surface areas, well-defined pore or cavity structures, or variable functionalities.^[3] Many applications of PCP/MOFs, such as gas storage and separation, drug delivery, sensing, and catalysis are based on the unique molecule sorption properties of these materials.^[4] Herein, we use the large molecule sorption properties of PCP/MOFs to synthesize a photoactive PCP/MOF-core–Au/anatase-shell material. The metal-organic framework MIL-101 (Cr)^[5] was used. In addition, we report on the application of the core–shell material for visible-light-driven photocatalytic wastewater purification from antibiotics and dye compounds, as well as for hydrogen generation from water. To the best of our knowledge, this is the first example of a PCP/MOF used as a core in conjunction with a crystalline anatase/plasmonic gold nanoparticle shell. The size of the core–shell compound could be manipulated by controlling the crystallite size of the metal–organic framework. The PCP/MOF is also necessary for the overall stability of the composite. The desired denseness of the anatase shell was achieved by a stepwise synthesis protocol, including the gas-phase infiltration of the TiO₂ precursor titanium(IV) isopropoxide [Ti(O*i*Pr)₄], followed by hydrolysis and the formation of the crystalline anatase shell under relatively mild reaction conditions. Crystalline anatase is reported to be the most beneficial modification of TiO₂ regarding the photocatalytic activity, because of the low charge-recombination rate.^[6] Catalytically active materials consisting of titanium dioxide and PCP/MOFs have already been reported in the literature mainly describing the generation of nanosized TiO₂ inside the PCP/MOF structure.^[7] The combination of plasmonic gold particles and the semiconductor TiO₂ is a promising approach to generate efficient photoactive materials under visible-light illumination.^[8] In addition, several PCP/MOFs including MIL-101 have been reported to be applicable in diverse photocatalytic processes, and represent a promising class of materials for the generation of photocatalysts by using further modifications;^[9] however, other synthesis strategies were employed. Our group has a long ongoing interest in PCP/MOF-based functional materials^[7g, 10] and therefore became interested in developing PCP/MOF-based photocatalysts.

5.2 Results and Discussion

The synthesis protocol of the MIL-101-core–Au/anatase-shell compound requires the generation of a dense anatase shell around the MIL-101 crystallites as a first step. Afterwards, gold particles were generated on the outer TiO₂ surface in order to maintain a shell of anatase covered with gold particles around the PCP/MOF crystallites (Scheme 1).



Scheme 1. Schematic illustration for the synthesis procedure of the MIL-101-core–Au/anatase-shell compound. A possible explanation for the generation of electron-hole pairs is the plasmonic excitation of gold particles on the surface of the anatase shell under visible-light illumination.

The gold particles are assumed to serve as the visible-light-capturing part of the composite material. The electromagnetic field of the incident light induces collective oscillations of free electrons within the gold nanoparticles, which is known as a localized surface-plasmon resonance effect.^[11] The energy received from such excited nanostructures can result in the generation of hot electrons. The combination of plasmonic nanostructures and semiconductors, such as TiO₂, allows for the separation of the charge carriers (hot electrons and corresponding holes) via the conduction band of the semiconductor. Consequently, the electrons may initiate locally separated reduction reactions. The volatile Ti-precursor titanium(IV) isopropoxide was infiltrated into the porous network system of MIL-101 for the generation of the anatase shell. MIL-101 was synthesized with a specific surface area of 2900 m²g⁻¹ and the characteristic cavity structures (Figure S1 in

the Supporting Information). The MIL-101 particles serve as size- and shape-directing centers for the final core–shell material. An average PCP/MOF particle size between 150 and 300 nm was applied in order to generate colloidal core–shell materials with a related size distribution. The gas-phase infiltration procedure of appropriate amounts of $[\text{Ti}(\text{O}i\text{Pr})_4]$ ensured the complete uptake of the precursor by the MIL-101 crystallites. Consequently, the gas-phase loading procedure gave a very high degree of reaction control, and the uncontrolled formation of pure TiO_2 agglomerates in undefined sizes and shapes was avoided. The resulting material was thermally processed under water atmosphere, which led to the decomposition of $[\text{Ti}(\text{O}i\text{Pr})_4]$ and to the formation of amorphous TiO_2 (Figure 1a) as described in a previous work.^[7g]

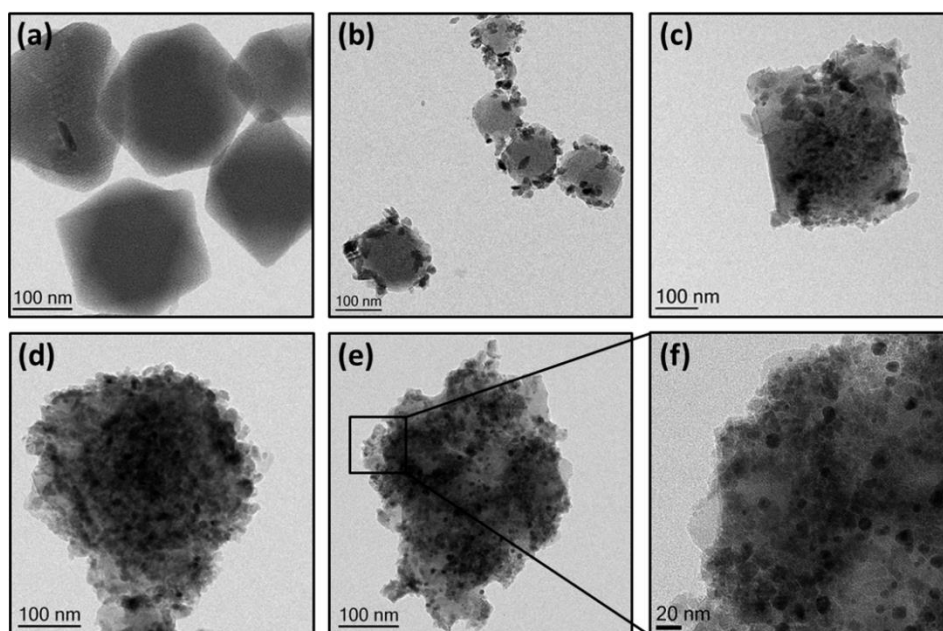


Figure 1. a) TEM image of MIL-101 crystallites with homogeneously incorporated amorphous TiO_2 . The generation of anatase under hydrothermal conditions led to a partial release of TiO_2 and the formation of anatase agglomerates on the outer surface of the MIL-101 crystallites, resulting in b) A@MIL-101 and c) A/A@MIL-101. d) The stepwise synthesis protocol resulted in the formation of the MIL-101 core–anatase shell material after the generation of anatase was performed three times. e) and f) The subsequent generation of gold particles on the surface of the anatase shell led to the MIL-101-core–Au/anatase-shell compound.

The formation of the anatase shell around the MIL-101 crystallites was carried out under mild hydrothermal conditions at 150 °C, which led to a fragmentary arrangement of anatase grains around the PCP/MOF crystallites visualized by transmission electron

microscopy (TEM) analysis (Figure 1b). In order to obtain a compact shell of titania, the generation procedure for anatase described was carried out twice more (the intermediate compounds with incomplete anatase shells are denoted as A@MIL-101 and A/A@MIL-101; Figure 1c). We achieved a dense anatase shell after the generation of anatase grains around the PCP/MOF crystallites three times (denoted as MIL-101 core–anatase shell) (Figure 1d). The formation of gold nanoparticles on top of the anatase shell was performed by gas-phase deposition of the gold(I) precursor [ClAu(CO)], followed by the reduction to Au⁰ particles under hydrogen atmosphere (Figure 1e,f). The final core–shell colloids still exhibit the octahedral shape of the MIL-101 crystallites. In order to demonstrate the necessity of the PCP/MOF regarding the stability of the whole MIL-101 core–anatase shell material, we decomposed the PCP/MOF crystallites by calcination or etching under alkaline conditions. The removal of the metal–organic core induced the collapse of the material (Figure S2 in the Supporting Information). We investigated the specific surface area of the compounds occurring during the synthesis of the MIL-101-core–Au/anatase-shell material by nitrogen physisorption measurements (Table S1). The initial specific surface area of MIL-101 was successively decreased by 83 % during the stepwise generation of the Au/anatase shell. The formation of TiO₂ inside the metal–organic network correlated with decreasing surface areas, whereas the following hydrothermal generation of anatase indicated a slight increase of the internal surface area. This investigation additionally supports the observation that partially released TiO₂ assembles the anatase shell. The remaining specific surface area of the MIL-101-core–anatase-shell material is related to the highly porous MIL-101 cores; the anatase shell did not introduce additional cavity structures (Figure S3). Only the characteristic pore species of the PCP/MOF were determined, despite the fact that the titanium dioxide shell around the MIL-101 crystallites reduced the pore accessibility. X-ray powder diffraction (XRD) analysis indicates the formation of crystalline anatase for the core–shell materials, as well as for A@MIL-101 and A/A@MIL-101 (Figure 2). Anatase was the only existing crystalline modification of TiO₂ observed in XRD analysis, which indicates the selective hydrothermal generation of an anatase shell under mild conditions. The synthesis of Au particles was also investigated by XRD, detecting the reflexes for crystalline cubic gold. We determined an average Au particle size of 18 nm on the basis of the (111) reflex using the Scherrer equation. The pattern from 2° to 20° (2θ) is attributed to the representative reflexes of the MIL-101 core. The generation of

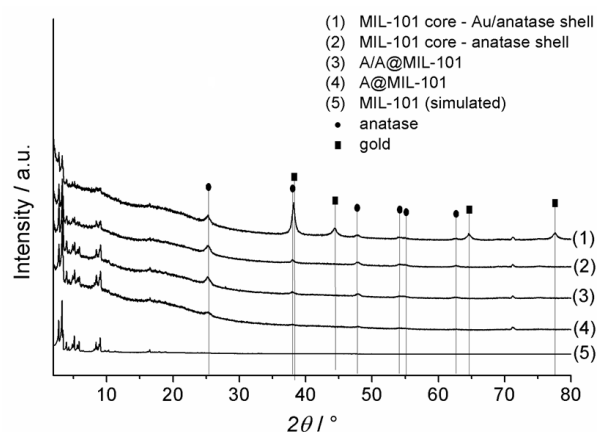


Figure 2. XRD analysis of A@MIL-101, A/A@MIL-101, MIL-101-core–anataseshell, and MIL-101-core–Au/anatase-shell materials.

amorphous TiO_2 inside MIL-101 through the decomposition of the infiltrated Ti-precursor $[\text{Ti}(\text{O}i\text{Pr})_4]$ did not result in any reflexes for crystalline titanium dioxide prior to the hydrothermal formation of anatase (Figure S4). The light absorption properties of the core–shell materials were investigated in comparison to MIL-101 by ultraviolet-visible (UV/Vis) spectroscopy (Figure 3a).

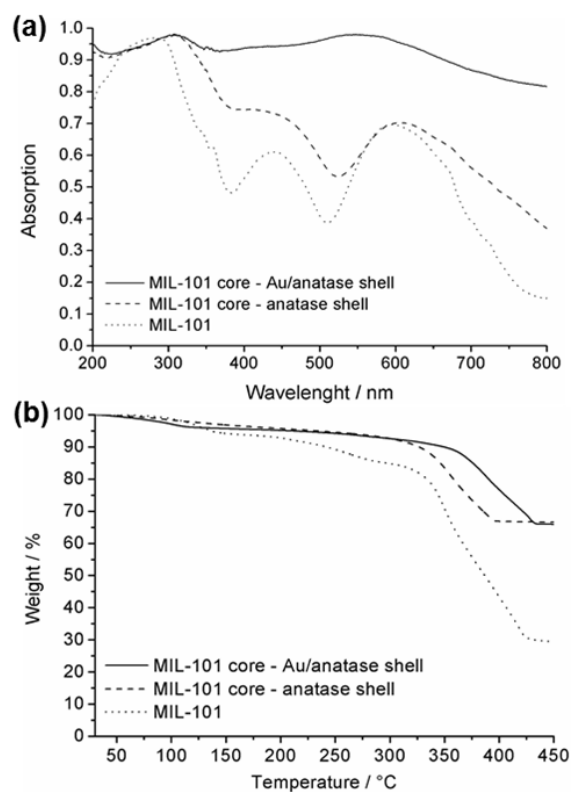


Figure 3. a) Diffuse reflectance UV/Vis spectra of MIL-101, MIL-101-core–anatase-shell, and MIL-101-core–Au/anatase-shell materials. b) TGA spectra of MIL-101, MIL-101-core–anatase-shell, and MIL-101-core–Au/anatase-shell materials.

The generation of the anatase shell around the PCP/MOF crystallites led to an increased light absorption of the MIL-101 core–anatase shell material between 300 and 500 nm compared to MIL-101. The dark purple MIL-101-core–Au/anatase-shell material exhibited an almost constant light absorption between 200 and 800 nm. Thermogravimetric analysis (TGA) shows a total weight loss of 34 % for the core–shell materials (Figure 3b). The mass loss of MIL-101 was 71 %. Fourier transform infrared (FTIR) spectroscopy analysis indicates the characteristic signals of MIL-101 in the range of 2000 to 550 cm^{-1} for the core–shell materials with and without gold particles (Figure S5). Considering the FTIR spectrum of anatase, the intensified signal of the core–shell compounds between 880 and 550 cm^{-1} is representative of the anatase shell. Energy-dispersive X-ray (EDX) analysis shows the characteristic element signals for the shell (Au, O, and Ti) and the MIL-101 core (C, Cr, and O) (Figure S6). The quantitative elemental composition of the MIL-101 core–Au/anatase shell material was determined by inductively coupled plasma optical emission spectroscopy (ICP-OES) analysis (Table 1).

Table 1. ICP-OES analysis of MIL-101-core–Au/anatase-shell, MIL-101-core–anatase-shell, and the materials generated used for comparison in photocatalytic wastewater treatment and hydrogen generation. The corresponding metal contents are given in wt%.

| Material | Ti | TiO ₂ ^[a] | Au | Cr |
|-------------------------------|------|---------------------------------|------|------|
| MIL-101-core–Au/anatase-shell | 22.6 | 37.7 | 28.1 | 7.1 |
| MIL-101-core–anatase-shell | 26.0 | 43.4 | - | 8.2 |
| Au@anatase | 45.3 | 75.6 | 22.2 | - |
| Au@P25 | 47.5 | 79.3 | 20.9 | - |
| Au/TiO ₂ @MIL-101 | 10.9 | 18.2 | 17.2 | 11.1 |
| Au@MIL-101 | - | - | 20.1 | 12.9 |

[a] Calculated on the basis of the Ti content.

The gold and titania shell amounted to 59.5 wt.% of the compound with an almost equal weight proportion of Au and Ti. Consequently, we assume that the remaining 40.5 wt.% was attributed to the MIL-101 core, which is almost in accordance with the TGA measurements.

We investigated the photocatalytic activity of the MIL-101-core–Au/anatase-shell material for the degradation of toxic organic dye compounds under visible-light illumination at a constant ambient temperature and neutral pH. The degradation of the xanthene dye rhodamine B was examined first (Figure 4a,b).

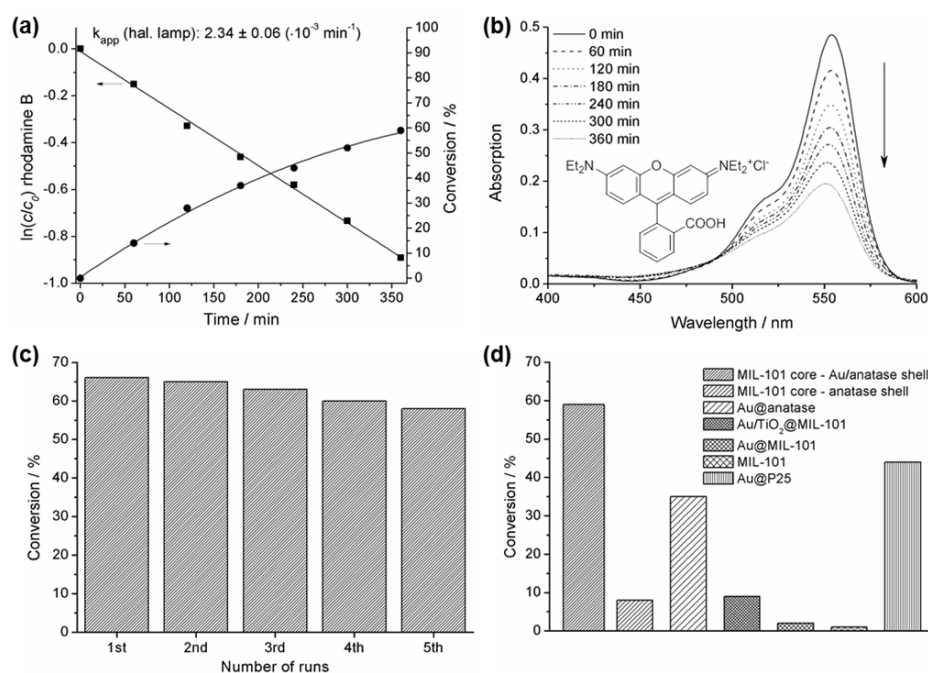


Figure 4. a) Photocatalytic degradation of rhodamine B with the MIL-101-core–Au/anatase-shell catalyst under visible light illumination. b) The time-dependent dye concentrations were determined based on the corresponding maxima of the absorption spectra. c) Reusability of the MIL-101-core–Au/anatase-shell catalyst for the photocatalytic degradation of rhodamine B. d) Comparison of catalysts for the photocatalytic degradation of rhodamine B under visible light illumination.

We used a halogen lamp with a broad emission of the visible light spectrum ($\lambda > 400$). The reaction temperature was kept constant by using a cooling jacket to avoid heating effects. The temperature of the reaction mixture (17 °C) was measured before the illumination and after 6 h of illumination for all experiments. In order to obtain the adsorption/desorption equilibrium of the dye and the catalyst material, and to determine the initial dye concentration, the respective reaction mixtures were stirred for two hours under the exclusion of light prior to the degradation experiments. We detected no further adsorption phenomena after stirring for two hours for all degradation experiments described in this work. The dye concentrations were analyzed by UV/Vis spectroscopy on the basis of the respective absorption maxima. The degradation reactions followed

pseudo-first-order kinetics approximately. The degradation of rhodamine B using the halogen lamp succeeded with a rate constant of $2.34 \pm 0.06 (\times 10^{-3} \text{ min}^{-1})$ and led to a total dye decomposition of 59 % under the conditions selected. The concentration of rhodamine B was investigated 1) during exposure to visible light without catalyst and 2) in the presence of the MIL-101-core–Au/anatase-shell catalyst under the exclusion of light (Figure S7 in the Supporting Information). Neither reaction showed any decrease of the dye concentration, thereby suggesting that the degradation of rhodamine B is a photocatalytic process. The reusability of the MIL- 101-core–Au/anatase-shell material was investigated for the photocatalytic degradation of rhodamine B. We performed five successive runs without a remarkable loss of activity (Figure 4c). The structural integrity of the reused core–shell catalyst after the degradation of rhodamine B was investigated by TEM analysis (Figure S8). We also demonstrated the beneficial contribution of the size-directing MIL-101 crystallites leading to a colloidal core–shell material. The photocatalytic activity of the MIL-101-core–Au/anatase-shell material was significantly higher than that of unstructured anatase covered with gold nanoparticles (denoted as Au@anatase), and even higher in comparison to commercially available TiO₂ powder (Degussa, P25) that was also decorated with Au particles (denoted as Au@P25) (Figure 4d). The MIL-101-core–anatase-shell material only showed a low photocatalytic activity without plasmonic gold particles. Amorphous TiO₂ incorporated into MIL-101, obtained by the infiltration of [Ti(OiPr)₄], resulted in a minor activity in combination with gold particles. The catalytic performance of Au@MIL-101 and the pure PCP/MOF MIL-101 was insignificantly low under visible-light illumination, since the small change in rhodamine B concentration is below the measurement precision. All catalyst materials described were synthesized under conditions comparable to those used to synthesize the core–shell material. The exact gold content is given in Table 1 and the catalysts used for comparison were additionally characterized with TEM analysis (Figure S9). We were also interested in the photocatalytic decomposition of methyl orange and methylene blue under visible light in order to investigate the degradation of additional (toxic) dyes (Figure 5a,b). The MIL-101-core–Au/anatase-shell catalyst again showed a good activity and the degradation reaction proceeded even faster than for rhodamine B under the same conditions. The rate constants determined were $3.30 \pm 0.06 (\times 10^{-3} \text{ min}^{-1})$ for methyl orange and $5.00 \times 0.01 (\times 10^{-3} \text{ min}^{-1})$ for methylene blue. We performed the control experiments for both dyes as already described for rhodamine B (Figures S10 and S11).

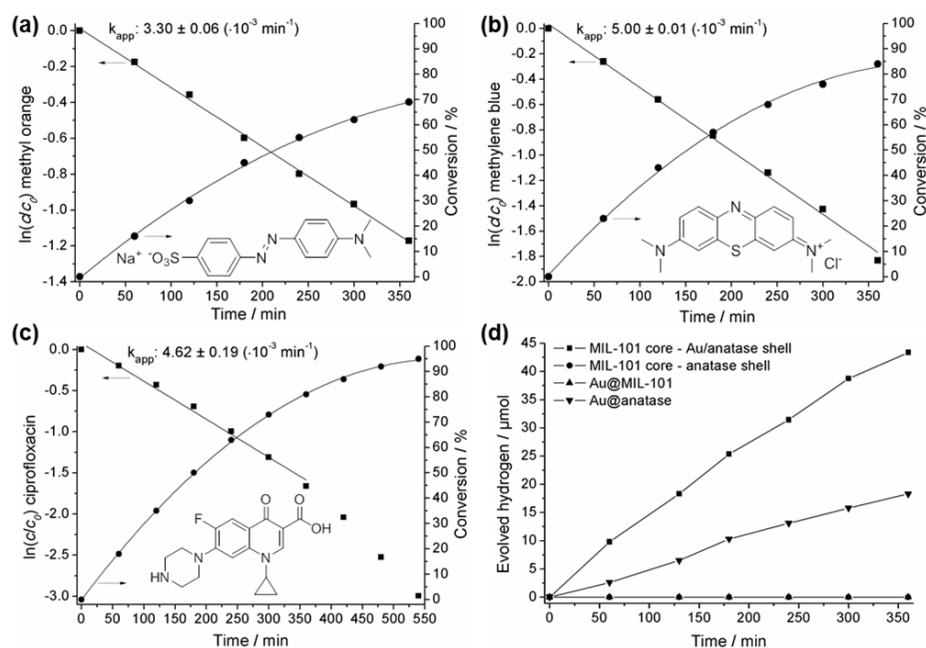


Figure 5. Visible-light-driven photocatalytic degradation of a) methyl orange, b) methylene blue, and c) ciprofloxacin with the MIL-101-core–Au/anatase-shell catalyst. d) Photocatalytic hydrogen evolution from a water/methanol solution with the MIL-101-core–Au/anatase-shell catalyst.

We detected no decomposition of methyl orange or methylene blue under the exclusion of light. Methyl orange is also stable under visible-light illumination without catalyst material. For methylene blue, we observed a small decrease in the concentration of about 6 % in 6 h without a catalyst. The different kinetic degradation rates of the dyes may be attributed to diverse interactions with the catalyst material, specific adsorption properties or varied degradation mechanisms. In order to amplify the application of the MIL-101-core–Au/anatase-shell catalyst in the field of water purification, we further surveyed the photocatalytic degradation of ciprofloxacin (1-cyclopropyl-6-fluoro-4-oxo-7-(piperazin-1-yl)-1,4-dihydroquinoline-3-carboxylic acid) (Figure 5c). Ciprofloxacin is a commonly used synthetic antibacterial drug of the fluoroquinolone group.^[12] The experiments were also carried out under visible-light illumination and neutral pH in an aqueous solution. We used slightly more catalyst material than for the decomposition of the dyes, which led to very good conversion numbers for the degradation of ciprofloxacin. The rate constant determined was $(4.62 \pm 0.19) \times 10^{-3} \text{ min}^{-1}$. The control experiments again verified a catalytic degradation of the antibiotic. The concentration of the ciprofloxacin solution remained constant during exposure to visible light without a catalyst and under the

exclusion of light together with the MIL-101-core–Au/anatase-shell material (Figure S12 in the Supporting Information).

Finally, we were interested in the photocatalytic activity of our core–shell compound for hydrogen generation from water (Figure 5d). The catalyst was homogeneously dispersed in a water/methanol mixture (2:1) and the suspension was purged with argon for 20 minutes. The hydrogen evolved in the reaction headspace was determined by gas chromatography using methane as internal standard. The MIL-101-core–Au/anatase-shell material showed a hydrogen evolution rate of $903 \text{ mmol h}^{-1} \text{ g}^{-1}$ and a higher activity than unstructured Au@anatase. The MIL-101-core–anatase-shell compound and Au@MIL-101 showed no hydrogen generation, indicating that the combination of gold and anatase is beneficial. The hydrogen evolution rate of other reported Au/TiO₂ photocatalysts fabricated under significantly higher temperatures could not be reached by the MIL-101-core–Au/anatase-shell material.^[13]

5.3 Conclusions

In summary, the first core–shell material combining a PCP/MOF core and a shell of crystalline anatase decorated with plasmonic gold nanoparticles was prepared. The average diameter of the colloids could be influenced through the size of the MIL-101 crystallites, and the denseness of the anatase shell could be controlled by a stepwise synthesis protocol under mild conditions. Additionally, the MIL-101 core was proven to be essential for the entire material's stability. We demonstrated the efficient application and the reusability of the MIL-101-core–Au/anatase-shell photocatalyst for visible-light-driven purification of dye compounds and the antibiotic ciprofloxacin from wastewater. In this context, the photocatalytic activity of the colloidal core–shell compound was significantly higher compared to that of Au@anatase, Au@MIL-101, Au/TiO₂@MIL-101, MIL-101-core–anatase-shell, MIL-101, and Au@P25. We also used our photocatalyst material for photocatalytic hydrogen evolution from water and demonstrated its superior activity in comparison to Au@anatase.

5.4 Experimental Section

Synthesis of MIL-101 (Cr): MIL-101 was synthesized according to previous work in order to maintain crystallite sizes between 150 nm and 300 nm.^[10g] $[\text{Cr}(\text{NO}_3)_3 \cdot 9\text{H}_2\text{O}]$ (640 mg, 1.60 mmol), terephthalic acid H_2BDC (265 mg, 1.60 mmol), HF 40 wt% (10 mL, 0.228 mmol) and deionized H_2O (8.00 mL) were sealed in a 23 mL Teflon-lined hydrothermal autoclave. The mixture was heated for 1 h at 80 °C (heating rate: 2.7 °C min⁻¹) and for 7.45 h at 220 °C (4.7 °C min⁻¹). The reaction mixture was quickly cooled down to 160 °C and slowly to 30 °C (cooling rate: 5.4 °C h⁻¹). Excessively crystallized H_2BDC was removed by filtration over a pore 3 filter. The green product was separated from the reaction solution by centrifugation (2000 rpm, 45 min). The MIL-101 was refluxed in ethanol/water (90/10 vol%) for 14 h and centrifuged (1800 rpm, 45 min) three times to remove α -CrOOH impurities. Repetitive differential centrifugation in ethanol/water (1800 rpm, 5 min) was also used to separate MIL-101 crystals with different size distributions. The different MIL-101 fractions were dried under vacuum (10⁻⁴ mbar, 95 °C). BET: 2900 m² g⁻¹; XRD (2 θ (°), intensity (%)): 2.78 (56), 3.26 (100), 3.41 (44), 3.94 (19), 4.30 (11), 4.84 (16), 5.13 (32), 5.59 (16), 5.85 (22), 6.24 (5), 6.48 (5), 8.10 (7), 8.40 (22), 8.58 (11), 8.86 (15), 9.02 (28), 9.71 (5), 9.86 (5), 10.30 (6), 11.22 (4), 16.50 (6).

Synthesis of the MIL-101-core–anatase-shell compounds: MIL-101 powder, A@MIL-101, or A/A@MIL-101 (500 mg) was placed in a two-chamber-tube with $[\text{Ti}(\text{O}i\text{Pr})_4]$ (0.75 mL, 2.50 mmol) separated by a glass frit. The gas-phase loading occurred at 35 °C in a 10⁻⁴ mbar (diffusion pump) dynamic vacuum for 16 h. The resulting bright green powder was subsequently processed by hydrolysis to yield TiO_2 @MIL-101. The hydrolysis of $[\text{Ti}(\text{O}i\text{Pr})_4]$ was performed by thermal treatment with water vapor at 80 °C in order to generate TiO_2 @MIL-101. The material was evacuated (10⁻⁴ mbar) at 95 °C for 18 h in order to remove excess ligand and water. The TiO_2 @MIL-101, TiO_2 /A@MIL-101, or TiO_2 /A/A@MIL-101 material and deionized water (50 mL) were sealed in a 125 mL Teflon-lined hydrothermal autoclave and heated at 150 °C for 8 h (heating rate: 2.5 °C min⁻¹). After cooling down to room temperature, the MIL-101-core–anatase-shell materials were dried under vacuum (10⁻⁴ mbar, 95 °C).

In order to generate the final MIL-101-core–anatase-shell material, this process was performed three times in order to produce a dense anatase shell.

Synthesis of MIL-101 core–Au/anatase-shell compounds, Au/TiO₂@MIL-101, Au@MIL-101, Au@P25, and Au@anatase: The MIL-101-core–anatase-shell material, TiO₂@MIL-101, MIL-101, P25, or anatase (100 mg) were placed in a Schlenk tube with [ClAu(CO)] (50 mg, 0.19 mmol) separated by a glass installation. The gas-phase loading was performed at 45 °C under static vacuum conditions for 20 h. The resulting dark green to violet powder was subsequently processed by hydrogenolysis. The reduction of [ClAu(CO)] to Au⁰ was performed under hydrogen atmosphere (30 bar H₂) at 100 °C for 20 h in a Parr Instruments steel autoclave. The resulting compounds were evacuated (10⁻⁴ mbar) at 95 °C for 20 h in order to remove excess metal and ligand.

Calcination/etching of MIL-101-core–anatase-shell materials: Calcination experiments of the MIL-101-core–anatase-shell powder (50 mg) were performed at 400 °C for 4 h (heating rate: 6.7 °C min⁻¹) under air atmosphere using a muffle furnace (Nabertherm). For the etching tests, MIL-101-core–anatase-shell powder (25 mg) was stirred in a mixture of deionized water (5.00 mL) and NaOH (0.20 mL, 2.5 M) for 2 h at 25 °C. The suspension was filtered (pore 3) and the solid residue was dried at 95 °C under reduced pressure (10⁻⁴ mbar) for 20 h.

Photocatalytic degradation of pollutants and antibiotics: The reactions were performed in a 150 mL two-necked reaction vessel equipped with a borosilicate glass window, magnetic stirring, and a cooling jacket. Each catalyst material (4.00 mg) investigated was mixed with the pollutant (20 mL) in aqueous solution (2 × 10⁻⁵ mol L⁻¹). For the degradation of ciprofloxacin, MIL-101-core–Au/anatase-shell (12.0 mg) and the antibiotic solution (20 mL; 2 × 10⁻⁵ mol L⁻¹) were used. The suspensions were stirred for 2 h under exclusion of light at 20 °C in order to achieve the adsorption/desorption equilibrium. The photocatalytic degradation experiments were performed using a tungsten halogen lamp (400 W, RITOS) with a UV filtering glass ($\lambda > 400$ nm). The distance between the lamp and the bottom of the vessel was 20 cm. For the recyclability studies, MIL-101-core–Au/anatase-shell material (6.00 mg) and rhodamine B solution (20 mL, 2 × 10⁻⁵ mol L⁻¹) were used and purified in water and ethanol three times between the runs of the recyclability studies. At given irradiation intervals, 1.00 mL of the reaction

mixture was taken out. The catalyst was separated by centrifugation at 8000 rpm for 8 min. UV/Vis spectra were measured from the supernatant solutions to determine the concentration of the pollutant based on the absorption maximum.

Photocatalytic hydrogen evolution: The reactions were performed in a two-necked reaction vessel equipped with a borosilicate glass window, magnetic stirring, and a cooling jacket and sealed with rubber septa (total volume of 28 mL). The catalyst (8.00 mg) was homogeneously dispersed in water/methanol (2:1; 3.00 mL) and degassed for 20 min by bubbling argon through the suspension. Methane (500 μ L) was added as internal standard. The hydrogen generation was performed using a tungsten halogen lamp (400 W, RITOS) with a UV filtering glass ($\lambda > 400$ nm). The distance between the lamp and the bottom of the reaction vessel was 15 cm. At given irradiation intervals, 500 μ L of the headspace was taken out and analyzed by gas chromatography.

Acknowledgements

The authors thank the Deutsche Forschungsgemeinschaft (DFG, SFB 840, B1) for funding as well as the DAAD Polymer and Colloids Network Melbourne-Bayreuth. Furthermore, the help of Florian Puchtler (XRD measurements), Martin Friedrich (TGA measurements), Beate Fçrster, and Dr. Christine Denner (EDX measurements) is gratefully acknowledged.

5.5 References

- [1] a) B. F. Abrahams, B. F. Hoskins, D. M. Michail, R. Robson, *Nature* **1994**, *369*, 727–729; b) B. F. Hoskins, R. Robson, *J. Am. Chem. Soc.* **1989**, *111*, 5962–5964.
- [2] a) H. Li, M. Eddaoudi, M. O’Keeffe, O. M. Yaghi, *Nature* **1999**, *402*, 276–279; b) O. M. Yaghi, H. Li, *J. Am. Chem. Soc.* **1995**, *117*, 10401–10402.
- [3] H. Furukawa, K. E. Cordova, M. O’Keeffe, O. M. Yaghi, *Science* **2013**, *341*, 1230444.
- [4] a) J.-R. Li, R. J. Kuppler, H.-C. Zhou, *Chem. Soc. Rev.* **2009**, *38*, 1477–1504; b) H. Wu, Q. Gong, D. H. Olson, J. Li, *Chem. Rev.* **2012**, *112*, 836–868; c) A. Morozan, F. Jaouen, *Energy Environ. Sci.* **2012**, *5*, 9269–9290; d) P. Horcajada, R. Gref, T. Baati, P. K. Allan, G. Maurin, P. Couvreur, G. Férey, R. E. Morris, C.

- Serre, *Chem. Rev.* **2012**, *112*, 1232–1268; e) J.-R. Li, J. Sculley, H.-C. Zhou, *Chem. Rev.* **2012**, *112*, 869–932; f) L. E. Kreno, K. Leong, O. K. Farha, M. Allendorf, R. P. Van Duyne, J. T. Hupp, *Chem. Rev.* **2012**, *112*, 1105–1125; g) J. Canivet, A. Fateeva, Y. Guo, B. Coasne, D. Farrusseng, *Chem. Soc. Rev.* **2014**, *43*, 5594–5617; h) J. Liu, L. Chen, H. Cui, J. Zhang, L. Zhang, C.-Y. Su, *Chem. Soc. Rev.* **2014**, *43*, 6011–6061; i) Q.-L. Zhu, Q. Xu, *Chem. Soc. Rev.* **2014**, *43*, 5468–5512.
- [5] G. Férey, C. Mellot-Draznieks, C. Serre, F. Millange, J. Dutour, S. Surblé, I. Margiolaki, *Science* **2005**, *309*, 2040–2042.
- [6] a) D. C. Hurum, A. G. Agrios, K. A. Gray, T. Rajh, M. C. Thurnauer, *J. Phys. Chem. B* **2003**, *107*, 4545–4549; b) E. Kowalska, S. Rau, B. Ohtani, *J. Nanotechnol.* **2012**, *2012*, 361853; c) J. B. Joo, Q. Zhang, M. Dahl, I. Lee, J. Goebel, F. Zaera, Y. Yin, *Energy Environ. Sci.* **2012**, *5*, 6321–6327.
- [7] a) M. Müller, X. Zhang, Y. Wang, R. A. Fischer, *Chem. Commun.* **2009**, 119–121; b) M. Müller, S. Turner, O. I. Lebedev, Y. Wang, G. van Tendeloo, R. A. Fischer, *Eur. J. Inorg. Chem.* **2011**, *2011*, 1876–1887; c) Y. Hu, Z. Huang, L. Zhou, D. Wang, G. Li, *J. Sep. Sci.* **2014**, *37*, 1482–1488; d) C. R. Kim, T. Uemura, S. Kitagawa, *Microporous Mesoporous Mater.* **2014**, *195*, 31–35; e) S. Abedi, A. Morsali, *ACS Catal.* **2014**, *4*, 1398–1403; f) R. Li, J. Hu, M. Deng, H. Wang, X. Wang, Y. Hu, H.-L. Jiang, J. Jiang, Q. Zhang, Y. Xie, Y. Xiong, *Adv. Mater.* **2014**, *26*, 4783–4788; g) D. Tilgner, M. Friedrich, J. Hermannsdörfer, R. Kempe, *ChemCatChem* **2015**, *7*, 3916–3922.
- [8] a) Q. Zhang, D. Q. Lima, I. Lee, F. Zaera, M. Chi, Y. Yin, *Angew. Chem.* **2011**, *123*, 7226–7230; *Angew. Chem. Int. Ed.* **2011**, *50*, 7088–7092; b) Z. W. Seh, S. Liu, M. Low, S.-Y. Zhang, Z. Liu, A. Mlayah, M.-Y. Han, *Adv. Mater.* **2012**, *24*, 2310–2314; c) J. B. Priebe, M. Karnahl, H. Junge, M. Beller, D. Hollmann, A. Brückner, *Angew. Chem.* **2013**, *125*, 11631–11635; *Angew. Chem. Int. Ed.* **2013**, *52*, 11420–11424; d) Z. Bian, T. Tachikawa, P. Zhang, M. Fujitsuka, T. Majima, *J. Am. Chem. Soc.* **2014**, *136*, 458–465; e) C.-T. Dinh, H. Yen, F. Kleitz, T.-O. Do, *Angew. Chem.* **2014**, *126*, 6736–6741; *Angew. Chem. Int. Ed.* **2014**, *53*, 6618–6623; f) W. Zhao, Z. Ai, J. Dai, M. Zhang, *PLoS One* **2014**, *9*, e103671; g) E. Kowalska, K. Yoshiiri, Z. Wei, S. Zheng, E. Kastl, H. Remita, B. Ohtani, S. Rau, *Appl. Catal. B: Environ.* **2015**, *178*, 133–143; h) J. Zhang, X. Jin, P. I. Morales-

- Guzman, X. Yu, H. Liu, H. Zhang, L. Razzari, J. P. Claverie, *ACS Nano* **2016**, *10*, 4496–4503; i) M. G. Méndez-Medrano, E. Kowalska, A. Lehoux, A. Herissan, B. Ohtani, S. Rau, C. Colbeau-Justin, J. L. Rodríguez-López, H. Remita, *J. Phys. Chem. C* **2016**, *120*, 25010–25022.
- [9] a) C. Gomes Silva, I. Luz, F. X. Llabrés i Xamena, A. Corma, H. García, *Chem. Eur. J.* **2010**, *16*, 11133–11138; b) C. Wang, K. E. deKrafft, W. Lin, *J. Am. Chem. Soc.* **2012**, *134*, 7211–7214; c) P. Wu, C. He, J. Wang, X. Peng, X. Li, Y. An, C. Duan, *J. Am. Chem. Soc.* **2012**, *134*, 14991–14999; d) A. Fateeva, P. A. Chater, C. P. Ireland, A. A. Tahir, Y. Z. Khimyak, P. V. Wiper, J. R. Darwent, M. J. Rosseinsky, *Angew. Chem.* **2012**, *124*, 7558–7562; *Angew. Chem. Int. Ed.* **2012**, *51*, 7440–7444; e) L. Chen, Y. Peng, H. Wang, Z. Gu, C. Duan, *Chem. Commun.* **2014**, *50*, 8651–8654; f) M. Wen, K. Mori, T. Kamegawa, H. Yamashita, *Chem. Commun.* **2014**, *50*, 11645–11648; g) D. Wang, R. Huang, W. Liu, D. Sun, Z. Li, *ACS Catal.* **2014**, *4*, 4254–4260; h) M. A. Nasalevich, R. Becker, E. V. Ramos-Fernandez, S. Castellanos, S. L. Veber, M. V. Fedin, F. Kapteijn, J. N. H. Reek, J. I. van der Vlugt, J. Gascon, *Energy Environ. Sci.* **2015**, *8*, 364–375; i) H.-Q. Xu, J. Hu, D. Wang, Z. Li, Q. Zhang, Y. Luo, S.-H. Yu, H.-L. Jiang, *J. Am. Chem. Soc.* **2015**, *137*, 13440–13443; j) Y. Wang, Y. Zhang, Z. Jiang, G. Jiang, Z. Zhao, Q. Wu, Y. Liu, Q. Xu, A. Duan, C. Xu, *Appl. Catal. B: Environ.* **2016**, *185*, 307–314.
- [10] a) T. Schareina, R. Kempe, *Z. Anorg. Allg. Chem.* **2000**, *626*, 1279–1281; b) T. Schareina, C. Schick, B. F. Abrahams, R. Kempe, *Z. Anorg. Allg. Chem.* **2001**, *627*, 1711–1713; c) T. Schareina, C. Schick, R. Kempe, *Z. Anorg. Allg. Chem.* **2001**, *627*, 131–133; d) S. Proch, J. Herrmannsdörfer, R. Kempe, C. Kern, A. Jess, L. Seyfarth, J. Senker, *Chem. Eur. J.* **2008**, *14*, 8204–8212; e) J. Herrmannsdörfer, R. Kempe, *Chem. Eur. J.* **2011**, *17*, 8071–8077; f) J. Herrmannsdörfer, M. Friedrich, N. Miyajima, R. Q. Albuquerque, S. Kümmel, R. Kempe, *Angew. Chem.* **2012**, *124*, 11640–11644; *Angew. Chem. Int. Ed.* **2012**, *51*, 11473–11477; g) J. Herrmannsdörfer, M. Friedrich, R. Kempe, *Chem. Eur. J.* **2013**, *19*, 13652–13657.
- [11] a) C. Clavero, *Nat. Photonics* **2014**, *8*, 95–103; b) C. Wang, D. Astruc, *Chem. Soc. Rev.* **2014**, *43*, 7188–7216.
- [12] P. C. Appelbaum, P. A. Hunter, *Int. J. Antimicrob. Agents* **2000**, *16*, 5–15.

- [13] a) C. Gomes Silva, R. Juárez, T. Marino, R. Molinari, H. García, *J. Am. Chem. Soc.* **2011**, *133*, 595–602; b) A. Tanaka, S. Sakaguchi, K. Hashimoto, H. Kominami, *ACS Catal.* **2013**, *3*, 79–85; c) K. Qian, B. C. Sweeny, A. C. Johnston-Peck, W. Niu, J. O. Graham, J. S. DuChene, J. Qiu, Y.-C. Wang, M. H. Engelhard, D. Su, E. A. Stach, W. D. Wei, *J. Am. Chem. Soc.* **2014**, *136*, 9842–9845; d) M. Serra, J. Albero, H. García, *ChemPhysChem* **2015**, *16*, 1842–1845.

5.6 Supporting Information

Experimental Section

General Considerations

All manipulations of air or moisture sensitive compounds were carried out under dry and oxygen-free argon atmosphere (Schlenk techniques) or in a nitrogen-filled glovebox (mBraun 120) with a high-capacity recirculator (below 0.1 ppm of oxygen and water).

Chlorocarbonyl gold(I) [ClAu(CO)], ciprofloxacin C₁₇H₁₈FN₃O₃, chromium(III) nitrate nonahydrate [Cr(NO₃)₃·9H₂O], hydrofluoric acid HF, methanol CH₄O, methylene blue C₁₆H₁₈ClN₃S, methyl orange C₁₄H₁₄N₃NaO₃S, rhodamine B C₂₈H₃₁ClN₂O₃, terephthalic acid H₂BDC C₆H₄(COOH)₂, titanium dioxide powder (Degussa, P25) TiO₂, and titanium(IV) isopropoxide [Ti(OCH(CH₃)₂)₄] were obtained commercially from chemical suppliers and used without further purification.

Energy-dispersive X-ray (EDX) analysis was performed using an Ultra plus FE-SEM (Zeiss) equipped with a STEM detector system. Elemental analysis was performed by standard protocols employing microwave assisted digestion (7 min at 170 °C (80 % power), 7 min at 180 °C (85 % power) and 20 min at 195 °C (90 % power)) in HCl (32 %, 4.5 mL), HNO₃ (65 %, 1.5 mL), and HF (40 %, 1.0 mL). The resulting solution was analyzed by inductively coupled plasma optical emission spectrometry (ICP-OES) using a Vista-Pro radial (Varian). Fourier transform infrared (FTIR) spectroscopy measurements were performed at a FTIR-Spectrum 100 (Perkin-Elmer) over a range from 4000 cm⁻¹ to 550 cm⁻¹. Gas chromatography (GC) analysis of gas mixtures was performed using a 6890N gas chromatograph (Agilent Technologies) equipped with an Agilent special Plot + Molsieve capillary column (30.0 m x 0.32 mm x 0.25 μm). Methane was

used as internal standard. Nitrogen physisorption isotherms were determined at $-196\text{ }^{\circ}\text{C}$ using a Nova 2000e (Quantachrome) apparatus. Specific surface areas were calculated by using p/p_0 -values from 0.05-0.25 by the BET model. Specific total pore volumes were measured by DFT calculations (N_2 at $-196\text{ }^{\circ}\text{C}$ on silica (cylindr. pore, NLDFT equilibrium model)). Transmission electron microscopy (TEM) measurements were carried out by using a LEO 922O (Zeiss, 200 kV). The samples were suspended in chloroform and sonicated for 5 min. 2 μL of the suspension were placed on a CF200-Cu-grid (Electron Microscopy Sciences) and allowed to dry. Thermogravimetric analysis (TGA) was performed from $30\text{ }^{\circ}\text{C}$ to $450\text{ }^{\circ}\text{C}$ ($5\text{ }^{\circ}\text{C min}^{-1}$) using a TGA/SDTA 851 $^{\circ}$ (Mettler) under air atmosphere. UV/Vis spectra (liquid) were taken for supernatants of the reaction solutions after centrifugation using a CARY 60 (Agilent Technologies) with Scan-software and PS-cuvettes (12.5 mm x 12.5 mm x 45 mm) or Hellma quartz glass cuvettes (12.5 mm x 12.5 mm x 45 mm). Diffuse reflectance UV/Vis spectra were measured using a CARY 300 (Agilent Technologies) with an Ulbricht sphere in the range of 200 nm to 800 nm. X-ray powder diffraction (XRD) analysis was performed using a STADI-P-diffractometer (STOE) ($\text{Cu}_{\text{K}\alpha}$ radiation, 1.54178 Å) in θ -2 θ -geometry with a position sensitive detector. The reference card numbers for comparison are 00-001-0562 for anatase and 00-001-1172 for gold.

Synthesis of MIL-101 (Cr)

MIL-101 was synthesized according to previous works in order to maintain crystallite sizes between 150 nm and 300 nm^[S1]. $[\text{Cr}(\text{NO}_3)_3 \cdot 9\text{ H}_2\text{O}]$ (640 mg, 1.60 mmol), H_2BDC (265 mg, 1.60 mmol), HF 40 wt.-% (10 μL , 0.228 mmol) and deionized H_2O (8.00 mL) were sealed in a 23 mL Teflon-lined hydrothermal autoclave. The mixture was heated for 1 h at $80\text{ }^{\circ}\text{C}$ (heating rate: $2.7\text{ }^{\circ}\text{C min}^{-1}$) and for 7.45 h at $220\text{ }^{\circ}\text{C}$ ($4.7\text{ }^{\circ}\text{C min}^{-1}$). The reaction mixture was cooled down fast to $160\text{ }^{\circ}\text{C}$ and slowly to $30\text{ }^{\circ}\text{C}$ (cooling rate: $5.4\text{ }^{\circ}\text{C h}^{-1}$). Excessively crystallized H_2BDC was removed by filtration over a pore 3 filter. The green product was separated from the reaction solution by centrifugation (2000 rpm, 45 min). The MIL-101 was refluxed in ethanol/water (90/10 vol.-%) for 14 h and centrifugalized (1800 rpm, 45 min) three times to remove α -CrOOH impurities. Repetitive differential centrifugation in ethanol/water (1800 rpm, 5 min) was also used to separate MIL-101 crystals with different size distribution. The different MIL-101

fractions were dried under vacuum (10^{-4} mbar, 95 °C). (BET: 2900 m² g⁻¹; XRD (2θ (°), intensity (%)): 2.78 (56), 3.26 (100), 3.41 (44), 3.94 (19), 4.30 (11), 4.84 (16), 5.13 (32), 5.59 (16), 5.85 (22), 6.24 (5), 6.48 (5), 8.10 (7), 8.40 (22), 8.58 (11), 8.86 (15), 9.02 (28), 9.71 (5), 9.86 (5), 10.30 (6), 11.22 (4), 16.50 (6)).

Synthesis of the MIL-101 core – Anatase shell compounds

500 mg of MIL-101 powder, A@MIL-101, or A/A@MIL-101 were placed in a two-chamber-tube with [Ti(OiPr)₄] (0.75 mL, 2.50 mmol) separated by a glass frit. The gas-phase loading occurred at 35 °C in a 10^{-4} mbar (diffusions pump) dynamic vacuum for 16 h. The resulting bright green powder was instantly processed in hydrolysis to yield TiO₂@MIL-101. The hydrolysis of [Ti(OiPr)₄] was performed by thermal treatment under H₂O atmosphere at 80 °C in order to generate TiO₂@MIL-101. The material was evacuated (10^{-4} mbar) at 95 °C for 18 h in order to remove former ligand recess and water. The TiO₂@MIL-101, TiO₂/A@MIL-101, or TiO₂/A/A@MIL-101 material and 50 mL of deionized water were sealed in a 125 mL Teflon-lined hydrothermal autoclave and heated at 150 °C for 8 h (heating rate: 2.5 °C min⁻¹). After cooling down to room temperature, the MIL-101 core – Anatase shell materials were dried under vacuum (10^{-4} mbar, 95 °C). The generation of the final MIL-101 core – Anatase shell material requires the described generation of anatase around the MIL-101 crystallites for three times in order to get a dense anatase shell.

Synthesis of MIL-101 core – Au/anatase shell compounds, Au/TiO₂@MIL-101, Au@MIL-101, Au@P25, and Au@anatase

100 mg of the MIL-101 core – anatase shell material, TiO₂@MIL-101, MIL-101, P25, or anatase were placed in a Schlenk tube with [ClAu(CO)] (50 mg, 0.19 mmol) separated by a glass installation. The gas-phase loading occurred at 45 °C under static vacuum conditions for 20 h. The resulting dark green to violet powder was instantly processed in hydrogenolysis. The reduction of [ClAu(CO)] to Au⁰ was performed under hydrogen atmosphere (30 bar H₂) at 100 °C for 20 h in a Parr Instruments steel autoclave. The resulting compounds were evacuated (10^{-4} mbar) at 95 °C for 20 h in order to remove former metal ligand recess.

Calcination of MIL-101 core – anatase shell

MIL-101 core – anatase shell powder (50 mg) was calcinated at 400 °C for 4 h (heating rate: 6.7 °C min⁻¹) under air atmosphere using a muffle furnace (Nabertherm).

Etching of MIL-101 core – anatase shell

MIL-101 core – anatase shell powder (25 mg) was stirred in a mixture of deionized water (5.00 mL) and NaOH (0.20 mL, 2.5 M) for 2 h at 25 °C. The suspension was filtered (pore 3) and the solid residue was dried at 95 °C under reduced pressure (10⁻⁴ mbar) for 20 h.

Photocatalytic degradation of pollutants and antibiotics

The reactions were performed in a 150 mL two necked reaction vessel equipped with a borosilicate glass window, magnetic stirring, and a cooling jacket. 4.00 mg of each catalyst material investigated were mixed with 20 mL of the pollutant in aqueous solution (2·10⁻⁵ mol L⁻¹). For the degradation of ciprofloxacin, 12.0 mg of MIL-101 core – Au/anatase shell and 20 mL of the antibiotic solution (2·10⁻⁵ mol L⁻¹) were used. The suspensions were stirred for 2 h under exclusion of light at 20 °C in order to achieve the adsorption/desorption equilibrium. The photocatalytic degradation experiments were performed using a tungsten halogen lamp (400 W, RITOS) with a UV filtering glass ($\lambda > 400$ nm). The distance between the lamp and the bottom of the vessel was 20 cm. For the recyclability studies, 6.00 mg of MIL-101 core – Au/anatase shell and 20 mL rhodamine B solution (2·10⁻⁵ mol L⁻¹) were used and purified in water and ethanol three times between the runs of the recyclability studies. At given irradiation intervals, 1.00 mL of the reaction mixture was taken out. The catalyst was separated by centrifugation at 8000 rpm for 8 min. UV/Vis spectra were measured from the supernatant solutions to determine the concentration of the pollutant based on the absorption maximum.

Photocatalytic hydrogen evolution

The reactions were performed in a two necked reaction vessel equipped with a borosilicate glass window, magnetic stirring, and a cooling jacket and sealed with rubber septa (total volume of 28 mL). 8.00 mg catalyst were homogeneously dispersed in 3.00 mL water/methanol (2:1) and degassed for 20 min by bubbling argon through the suspension. 500 μ L of methane were added as internal standard. The hydrogen generation

was performed using a tungsten halogen lamp (400 W, RITOS) with a UV filtering glass ($\lambda > 400$ nm). The distance between the lamp and the bottom of the reaction vessel was 15 cm. At given irradiation intervals, 500 μ L of the headspace were taken out and analyzed by GC.

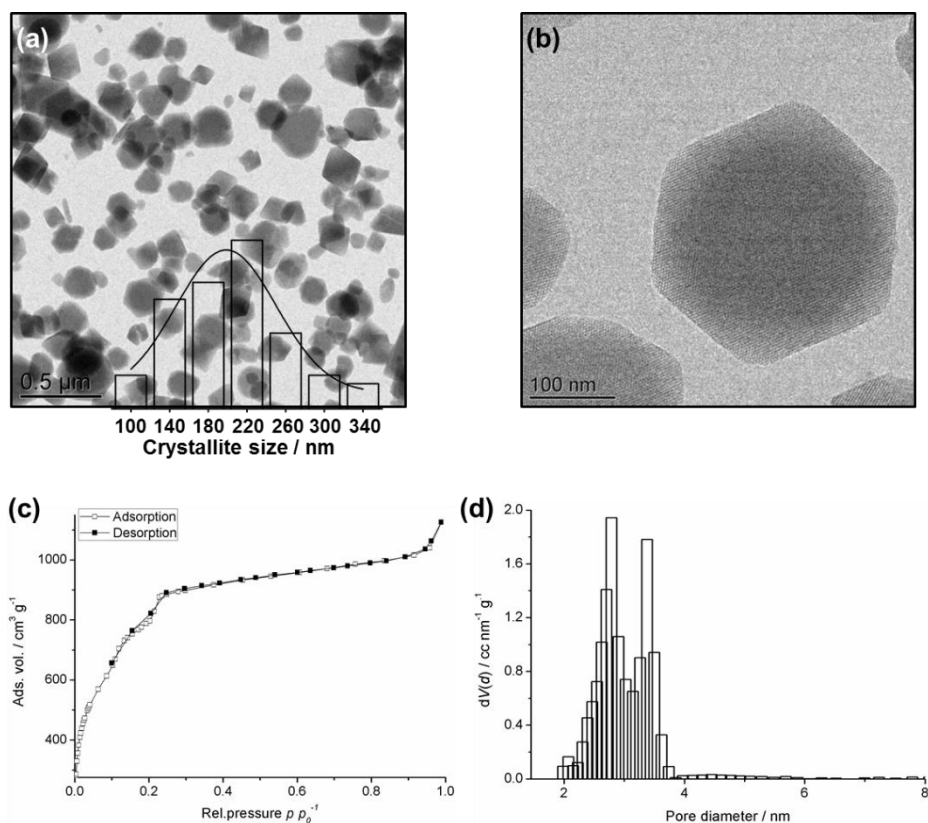


Figure S1. The MIL-101 crystallites were synthesized in their characteristic octahedral shape with an average diameter of about 200 nm (a, b). The specific surface area of 200 $\text{m}^2 \text{g}^{-1}$ as well as the cavity sizes were determined based on nitrogen physisorption measurements using the BET method (c, d).

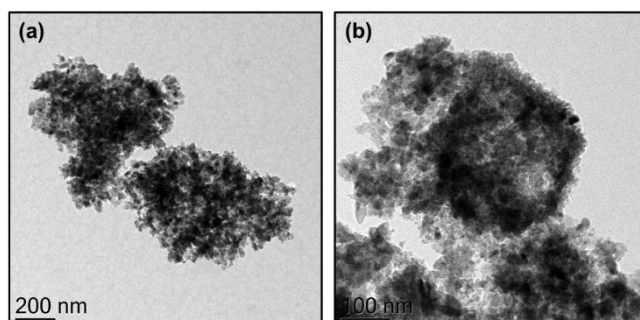


Figure S2. TEM micrographs of MIL-101 core – anatase shell calcinated at 400 °C for 4 h (a) or etched with NaOH (b).

Table S1. Nitrogen physisorption analysis of the MIL-101 core – Au/anatase shell compound and the intermediate materials.

| Sample | Surface area ($\text{m}^2 \text{g}^{-1}$, BET) |
|---------------------------------|--|
| MIL-101 | 2900 |
| TiO_2 @MIL-101 | 1360 |
| A@MIL-101 | 1790 |
| TiO_2 /A@MIL-101 | 860 |
| A/A@MIL-101 | 1120 |
| TiO_2 /A/A@MIL-101 | 690 |
| MIL-101 core – anatase shell | 830 |
| MIL-101 core – Au/anatase shell | 510 |

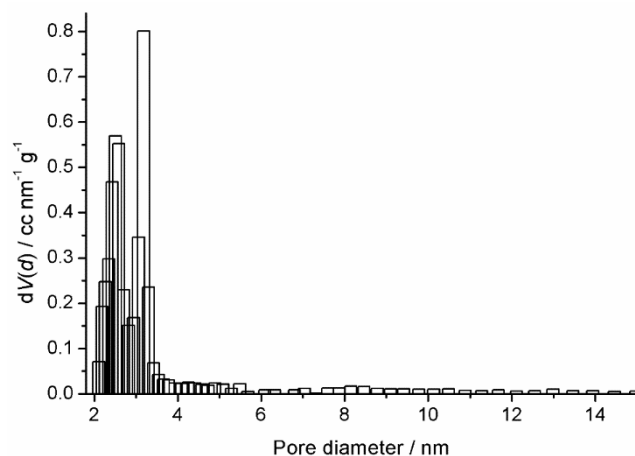


Figure S3. Pore size distribution of the MIL-101 core – anatase shell material.

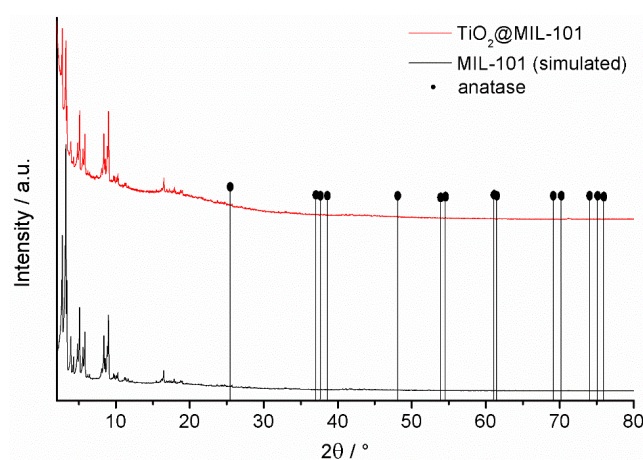


Figure S4. XRD analysis of amorphous TiO_2 incorporated in MIL-101 (TiO_2 @MIL-101).

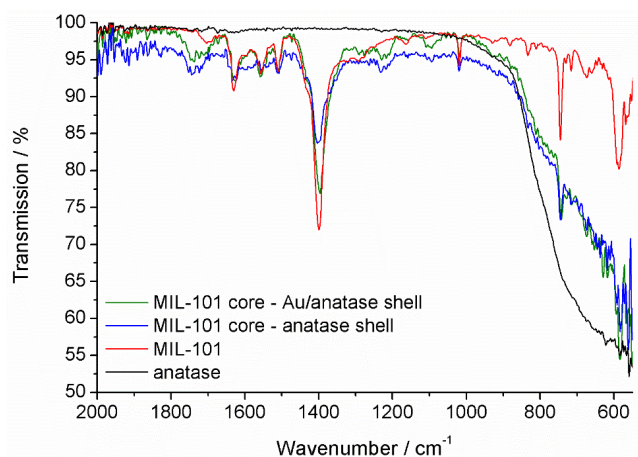


Figure S5. FTIR spectra of MIL-101 core – Au/anatase shell, MIL-101 core – anatase shell, MIL-101, and anatase.

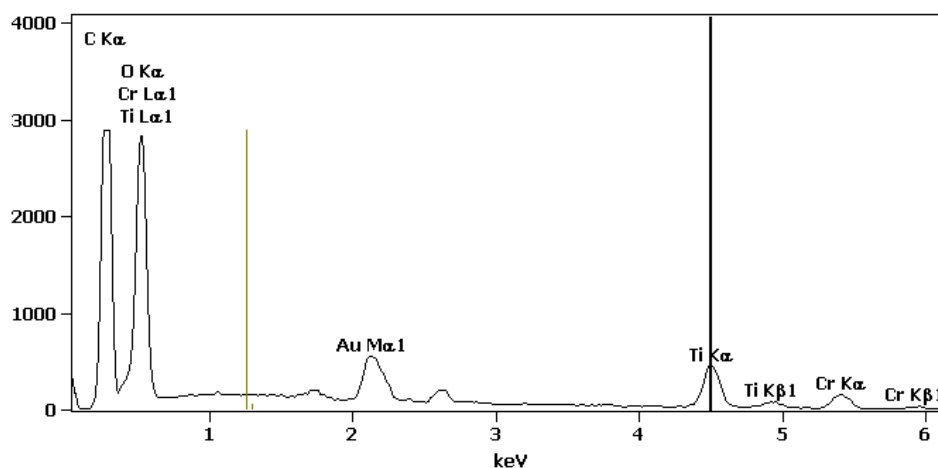


Figure S6. EDX analysis of the MIL-101 core – Au/anatase shell material with the representative element signals for Au, C, Cr, O, and Ti.

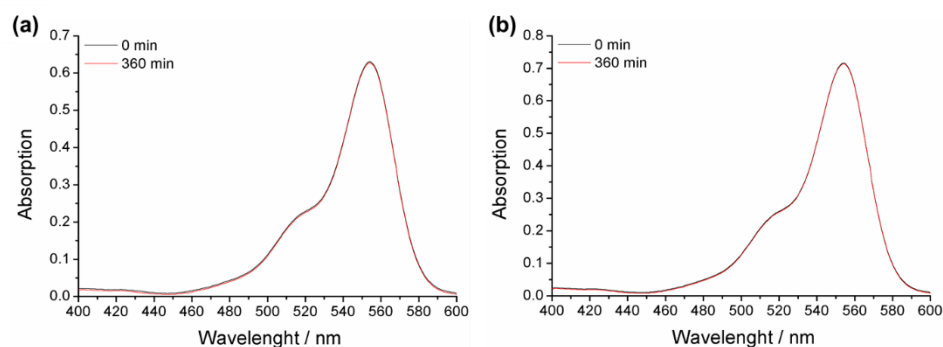


Figure S7. Stability of rhodamine B in presence of the MIL-101 core – Au/anatase shell catalyst in absence of any light (a) and under visible light illumination in absence of catalyst (b).

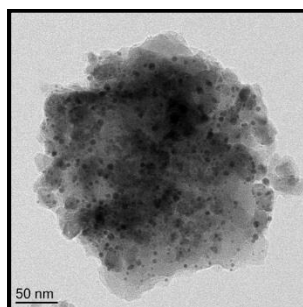


Figure S8. TEM micrograph of the MIL-101 core – Au/anatase shell catalyst reused for the photocatalytic degradation of rhodamine B and extensively purified with water.

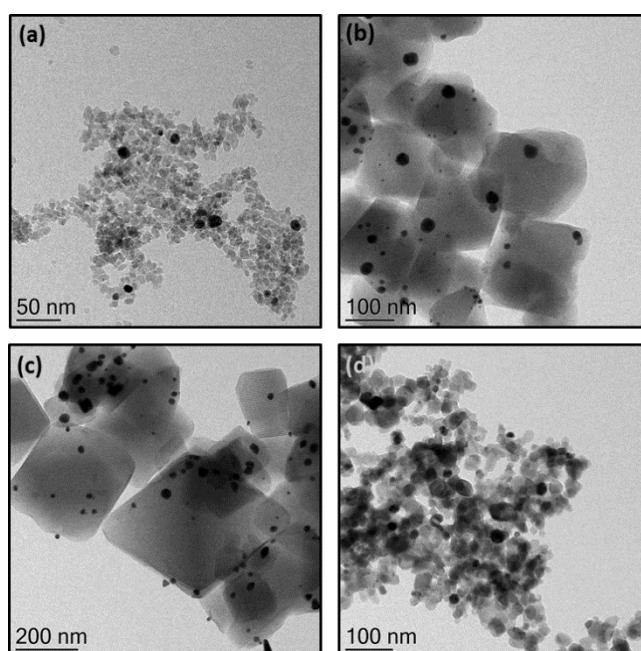


Figure S9. TEM micrographs of Au@anatase (a), Au/TiO₂@MIL-101 (b), Au@MIL-101 (c), and Au@P25 (d).

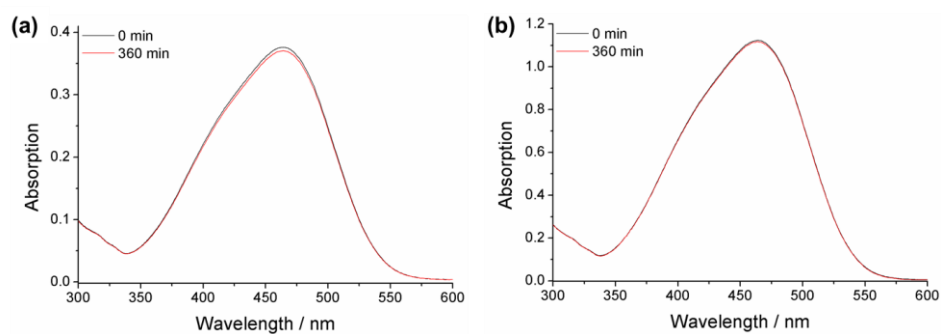


Figure S10. Stability of methyl orange in presence of the MIL-101 core – Au/anatase shell catalyst in absence of any light (a) and under visible light illumination in absence of catalyst (b).

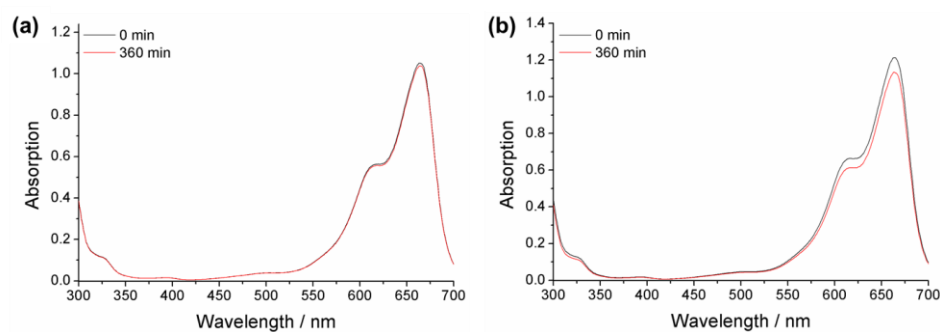


Figure S11. Stability of methylene blue in presence of the MIL-101 core – Au/anatase shell catalyst in absence of any light (a) and under visible light illumination in absence of catalyst (b).

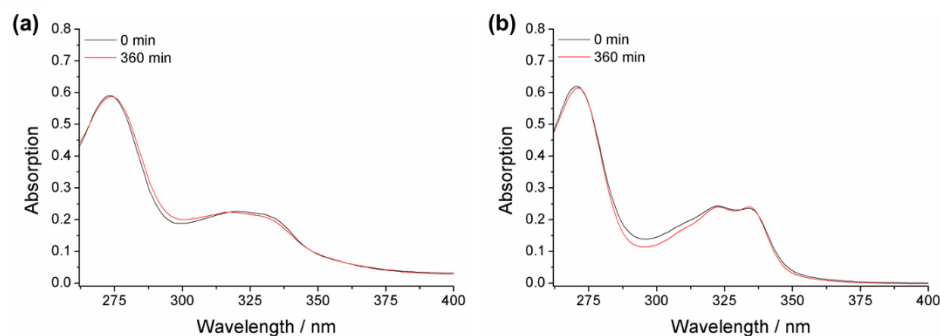


Figure S12. Stability of ciprofloxacin in presence of the MIL-101 core – Au/anatase shell catalyst in absence of any light (a) and under visible light illumination in absence of catalyst (b).

References

- [S1] J. Hermannsdörfer, M. Friedrich, R. Kempe, *Chem. Eur. J.* **2013**,*19*,13652–13657.

6 Visible Light-Driven Hydrogen Generation from Alcohols for C-N Multiple Bond Formation by a Metal-Organic Framework-Based Noble Metal-Free Photocatalyst

Dominic Tilgner,^[a] Martin Friedrich,^[a] Andreas Verch,^[b] Niels de Jonge,^[b,c] and Rhett Kempe*^[a]

[a] Inorganic Chemistry II, Catalyst Design, University of Bayreuth, Universitätsstraße 30, 95440 Bayreuth (Germany).

[b] INM – Leibniz Institute for New Materials, University Bayreuth, Campus D2 2, 66123 Saarbrücken (Germany).

[c] Department of Physics, Saarland University, Campus A5 1, 66123 Saarbrücken (Germany).

To be submitted.

Keywords: alcohol splitting; hydrogen generation; metal-organic frameworks; photocatalysis; sustainable synthesis

Abstract: The synthesis of important classes of chemical compounds from alcohols helps to conserve our fossil carbon resources, since alcohols can be obtained from indigestible and abundantly available biomass. The utilization of visible light for the activation of alcohols could permit alcohol-based C-N and C-C bond formation under conditions inaccessible with thermally operating hydrogen liberation catalysts. Herein, we report on a noble metal-free photocatalyst able to mediate C-N multiple bond formation efficiently using alcohols via liberation of H₂. The photocatalyst consists of a Ni/CdS/TiO₂ heterojunction generated on size-optimized colloidal metal-organic framework (MOF) crystallites. The reusable photocatalyst also permits alcohol splitting into hydrogen and carbonyl compounds under inert gas atmosphere and without the requirement of electron donors, additives, or aqueous reaction media. We expect our findings to inspire others to develop photocatalysts that mediate C-N and C-C bond formation, and to form important classes of compounds concertedly from alcohols.

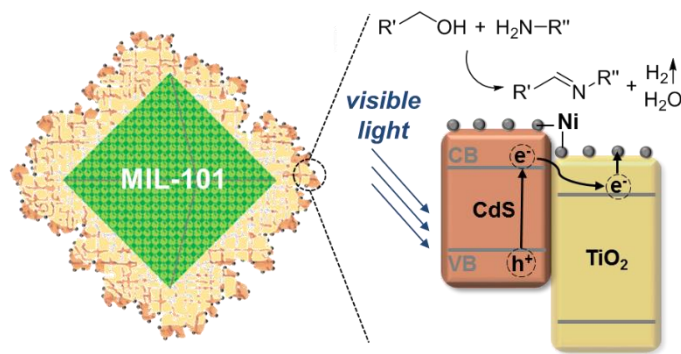
6.1 Introduction

The dehydrogenation of alcohols is a fundamental reaction in green or sustainable chemistry.^[1] Alcohols can be obtained via pyrolysis and hydrogenation from lignocellulose,^[2] an abundantly available, indigestible, and barely used biomass.^[3] Alcohols are rather unreactive and dehydrogenation is an elegant way of activating them. The oxidized form, carbonyl compounds, can undergo condensation reactions permitting the formation of C-C or C-N multiple bonds. The synthesis of imines from alcohols and amines introduced by Milstein and co-workers is an example of broad interest for such a C-N bond formation reaction.^[5] Our group has developed the synthesis of aromatic N-heterocyclic compounds from alcohols in which C-N and C-C multiple bond formation takes place concertedly.^[4,6-8] We expected that a photocatalyst able to mediate C-N bond formation via dehydrogenative coupling or condensation under very mild reaction conditions or thermodynamically unfavorable conditions is highly desirable to significantly extend the applicability of existing thermally operating noble metal-free catalysts for such reactions.^[5b,6b,8b-c,9] Herein, we report on a photocatalyst which can mediate visible light-driven imine synthesis from alcohols and amines. This C-N multiple bond formation takes place via hydrogen generation from alcohols under very mild or thermodynamically unfavorable conditions and no sacrificial electron donors need to be added (alcohol splitting). Our noble metal-free photocatalyst consists of a Ni/CdS/TiO₂ heterojunction generated on a porous support. The generation of a CdS/TiO₂ junction on porous supports with a high surface area is challenging and has not been accomplished before.^[10] The metal-organic framework or porous coordination polymer MIL-101 (Cr)^[11] was used as the porous support material.^[12] We also demonstrate the acceptorless dehydrogenation of alcohols or splitting of alcohols into hydrogen and carbonyl compounds at room temperature with a broad substrate scope by generating aldehydes as well as dialkyl, diaryl, and aryl-alkyl ketones. Visible light-driven alcohol dehydrogenation without electron donors is extremely rare in the literature^[13] and often requires aqueous media, including additives.^[14] Aqueous media are disadvantageous regarding condensation steps, which are needed in many dehydrogenative coupling/condensation reactions.

6.2 Results and Discussion

We expected that the arrangement of CdS and TiO₂ nanocrystals on a suitable metal-organic framework is an elegant way to create heterojunction systems with efficient charge carrier separation and high photocatalytic activity. The pores of the MOF can be selectively loaded with precursor molecules to control the size and amount of the different nanocrystals without applying surface blocking ligands. MIL-101 (Cr) was chosen because of its stability during solvothermal modifications and its large pores. It was prepared according to a procedure described previously with an average crystallite size of 300 nm (Supporting Information, Figure S1). This crystallite size is optimal regarding catalytic performance.^[15] The crystallites are large enough to ensure efficient separation for reusability and small enough to have a sufficiently large outer surface for modification with light harvesting materials. We recently reported a synthesis protocol for the generation of crystalline TiO₂ (anatase) on the metal-organic framework MIL-101 leading to a core-shell morphology.^[12] Titanium(IV) isopropoxide was infiltrated into MIL-101 by gas phase loading. The subsequent hydrolysis of the Ti precursor led to the formation of amorphous TiO₂ inside the cavities of MIL-101. The crystallization of TiO₂ (anatase) on the surface of the MOF crystallites was performed under hydrothermal conditions. In this work, the resulting TiO₂@MIL-101 material was modified with CdS under solvothermal conditions using cadmium acetate dihydrate and dimethylsulfoxide as precursors to yield CdS/TiO₂@MIL-101. Finally, we decorated the core-shell material with homogeneously distributed nickel nanoparticles using bis(cyclopentadienyl)nickel(II) as the volatile Ni precursor. The Ni/CdS/TiO₂@MIL-101 photocatalyst and the characteristic charge carrier separation between the semiconducting materials^[16] is illustrated in Scheme 1.

The initial specific surface area of MIL-101 decreased noticeably during the generation of TiO₂ and CdS, as investigated by nitrogen physisorption measurements (Supporting Information, Figure S2). Only a minor reduction of the specific surface area was observed after the modification with nickel. Crystalline TiO₂ (anatase) and CdS (cubic) were identified by X-ray powder diffraction (XRD) analysis (Supporting Information, Figure S3). The characteristic reflexes from 2° to 20° (2 θ) indicate the preserved structure of MIL-101. X-ray photoelectron spectroscopy analysis confirmed the presence of TiO₂ and CdS. Signals for Ni⁰ and Ni^{II} were observed in the Ni 2p spectrum. The presence of Ni^{II}



Scheme 1. Illustration of the Ni/CdS/TiO₂@MIL-101 material with a core-shell morphology. The MOF-supported Ni/CdS/TiO₂ heterojunction system is an efficient photocatalyst for the dehydrogenative coupling of alcohols and amines under visible light illumination.

can be attributed to the formation of nickel(II) hydroxide during the handling of the sample (Supporting Information, Figure S4). We determined the elemental composition of the materials by inductively coupled plasma optical emission spectrometry measurements (Supporting Information, Table S1). The Ni/CdS/TiO₂@MIL-101 material comprised 3.6 wt.-% Ni, 18.8 wt.-% CdS, and 26.0 wt.-% TiO₂. Diffuse reflectance ultraviolet-visible spectra in the range from 450 to 800 nm show an increased light absorption for TiO₂@MIL-101 and CdS/TiO₂@MIL-101 in comparison to MIL-101 (Supporting Information, Figure S5). The modification with CdS resulted in a distinctive edge for CdS/TiO₂@MIL-101, which is comparable to the absorption of cubic cadmium sulfide. We investigated the size and shape of the Ni/CdS/TiO₂@MIL-101 crystallites by transmission electron microscopy (TEM) and high-angle annular dark-field scanning TEM (HAADF-STEM) measurements (Figure 1). The typical octahedral shape and the homogeneous size distribution of the MIL-101 crystallites was also observed for Ni/CdS/TiO₂@MIL-101. Energy-dispersed X-ray maps demonstrate the uniformed arrangement of TiO₂, CdS, and Ni around MIL-101. The direct interface between the crystalline semiconductors CdS and TiO₂ was also verified by the characteristic lattice planes. Nickel was located on CdS and TiO₂ and showed a marginal tendency for agglomeration (Supporting Information, Figure S5). We investigated the TiO₂@MIL-101 and CdS@MIL-101 materials by TEM measurements to get an impression of the magnitude of the CdS and TiO₂ crystallites formed on the surface of MIL-101 (Supporting Information, Figure S7). The average particle size determined was about 35 nm for TiO₂ and 20 nm for CdS.

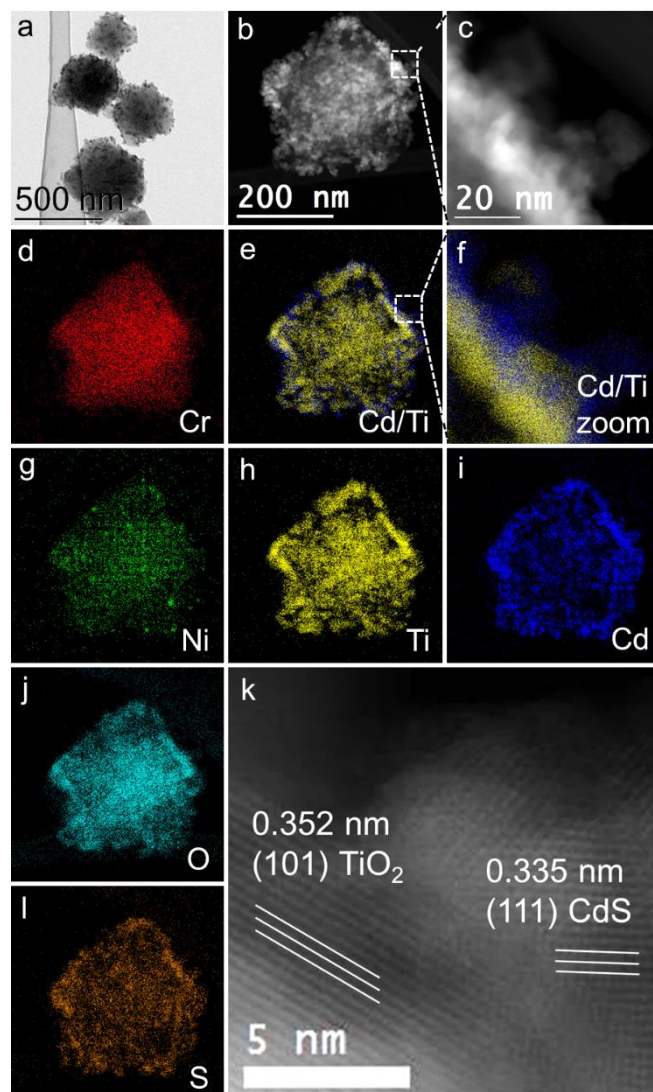


Figure 1. a) TEM micrograph of Ni/CdS/TiO₂@MIL-101. b-l) HAADF-STEM analysis of Ni/CdS/TiO₂@MIL-101 with representative energy-dispersed X-ray element maps and characteristic lattice planes for crystalline CdS and TiO₂.

The photocatalytic liberation of hydrogen via the oxidation of alcohols leading to carbonyl compounds was performed under argon atmosphere and without additives or acceptor molecules. A 50 W blue LED (470 nm) was used as visible light source while the temperature (27 °C) was maintained by a fan (Supporting Information, Figure S9). The dehydrogenation of benzyl alcohol was investigated first. Acetonitrile was identified as the most suitable solvent and the loading with a Ni amount of 4 wt% showed the highest activity (Supporting Information, Table S2, S3). We investigated the photocatalytic activity of CdS/TiO₂@MIL-101 being modified with the noble metals Pd, Pt, and Au to ensure the superior performance of our Ni/CdS/TiO₂@MIL-101 catalyst.

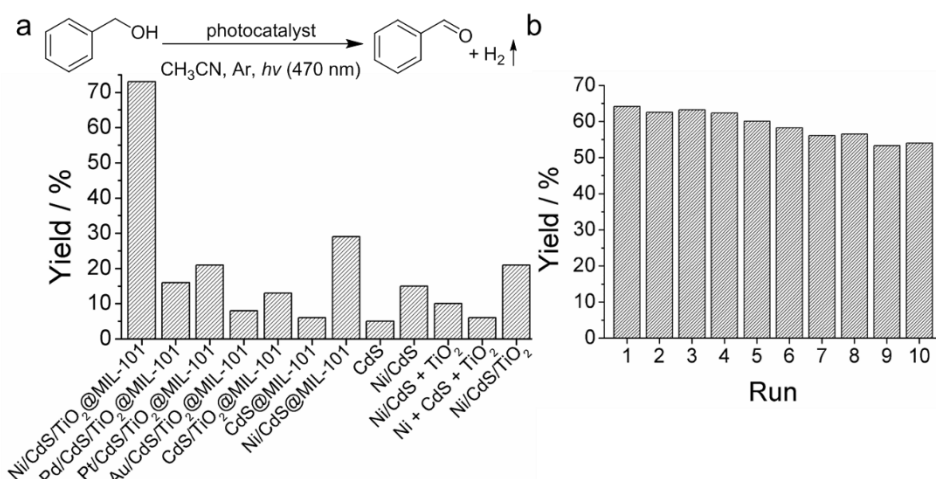
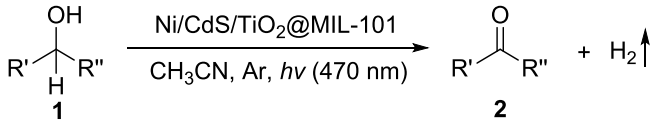
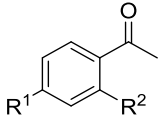
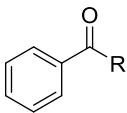
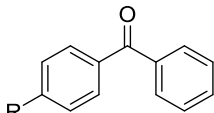
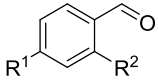
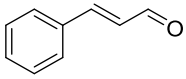


Figure 2. a) Comparison of different photocatalysts for the dehydrogenation of benzyl alcohol. The yields were determined by gas chromatography (GC) using n-dodecane as internal standard. b) Reusability of the Ni/CdS/TiO₂@MIL-101 catalyst with an activity decrease of less than 10 % after ten runs resulting from the purification procedure of the catalyst between the runs.

To our delight, the Ni-modified catalyst system clearly showed the highest activity (Figure 2a). The beneficial contribution of the junction system between the semiconductors was demonstrated by the higher activity of CdS/TiO₂@MIL-101 in comparison to CdS@MIL-101. We also demonstrated the favorable effect resulting from the support of Ni/CdS/TiO₂ on MIL-101 in comparison to pure Ni, CdS, TiO₂, and Ni/CdS/TiO₂. All materials without cadmium sulfide as the light-absorbing component showed no activity under visible light illumination (Supporting Information, Table S4). The reusability of Ni/CdS/TiO₂@MIL-101 was confirmed by performing ten successive runs without a remarkable loss of photocatalytic activity (Figure 2b). The material was analysed by TEM and XRD measurements after the last run to show the structural integrity (Supporting Information, Figure S10). A light on/off experiment was performed to examine whether the dehydrogenation of benzyl alcohol is indeed a visible light-mediated reaction (Supporting Information, Figure S11). The amount of H₂ released during the reaction was only increased under light illumination. Our photocatalyst Ni/CdS/TiO₂@MIL-101 is able to split a broad range of alcohols (**1**) forming the corresponding aldehydes, aryl-alkyl, diaryl, and dialkyl ketones (**2**) (Table 1). A variety of functional groups was well tolerated including halogens, methoxy, hydroxyl, trifluoromethyl, and amino groups. In addition, hydrogenation-sensitive functional groups, such as nitrile and nitro groups, and C=C bonds can be tolerated selectively.

Table 1. Photocatalytic dehydrogenation of aryl, aryl-alkyl, diaryl, and dialkyl alcohol compounds.^[a]

| Entry | Product | R | Yield ^[b] [%] |
|-------------------|---|---|--------------------------|
| |  | | |
| 1 | | 2a R ¹ = H, R ² = H | 97 |
| 2 | | 2b R ¹ = OMe, R ² = H | 96 |
| 3 | | 2c R ¹ = Me, R ² = H | 92 |
| 4 |  | 2d R ¹ = H, R ² = Me | 81 |
| 5 ^[c] | | 2e R ¹ = Me, R ² = Me | 83 |
| 6 ^[d] | | 2f R ¹ = F, R ² = H | 71 |
| 7 | | 2g R ¹ = Cl, R ² = H | 97 |
| 8 | | 2h R ¹ = Br, R ² = H | 96 |
| 9 | | 2i R = Et | 93 |
| 10 ^[c] |  | 2j R = Bu | 83 |
| 11 ^[c] | | 2k R = CH ₂ OH | 90 |
| 12 | | 2l R = H | 88 |
| 13 |  | 2m R = Me | 91 |
| 14 | | 2n R = OMe | 82 |
| 15 ^[d] | cycloheptanone | 2o | 86 |
| 16 | | 2p R ¹ = H, R ² = H | >99 |
| 17 ^[d] | | 2q R ¹ = CN, R ² = H | 93 |
| 18 ^[d] |  | 2r R ¹ = NO ₂ , R ² = H | 88 |
| 19 ^[d] | | 2s R ¹ = H, R ² = NO ₂ | 71 |
| 20 | | 2t R ¹ = H, R ² = NH ₂ | 96 |
| 21 | | 2u R ¹ = CF ₃ , R ² = H | 70 |
| 22 ^[d] |  | 2v | 70 |

[a] Reaction conditions: 0.1 mmol alcohol, 0.6 mg Ni/CdS/TiO₂@MIL-101, Ar, 0.3 mL CH₃CN, 27 °C, 24 h, 470 nm blue LED 50 W. [b] Determined by GC using n-dodecane as internal standard. [c] 1.2 mg Ni/CdS/TiO₂@MIL-101. [d] 1.2 mg Ni/CdS/TiO₂@MIL-101, 48 h.

We converted a total of 38 alcohols to the respective carbonyl compounds in good to excellent yields (Table 1, Supporting Information, Table S5). We further checked whether hydrogen is released equimolar during the photocatalytic reaction for several substrates using methane as an internal standard (Supporting Information, Table S6).

Finally, we were interested in photocatalytic C-N multiple bond formation reactions (Table 2).

Table 2. Photocatalytic synthesis of imines from primary alcohols and amines.^[a]

| Entry | Product | R | Yield ^[b] [%] |
|-------|--|--|--------------------------|
| | $\text{R}'\text{-CH}_2\text{-OH} + \text{H}_2\text{N-R}'' \xrightarrow[\text{-H}_2, \text{-H}_2\text{O}]{\text{Ni/CdS/TiO}_2\text{@MIL-101, CH}_3\text{CN, Ar, } h\nu (470 \text{ nm})} \text{R}'\text{-CH=N-R}''$ | | |
| 1 | | 5a R ¹ = H, R ² = H | 92 % |
| 2 | | 5b R ¹ = Me, R ² = H | 86 % |
| 3 | | 5c R ¹ = H, R ² = Me | 80 % |
| 4 | | 5d R ¹ = OMe, R ² = H | 92 % |
| 5 | | 5e R ¹ = F, R ² = H | 76 % |
| 6 | | 5f R ¹ = Cl, R ² = H | 88 % |
| 7 | | 5g R ¹ = Br, R ² = H | 53 % |
| 8 | | 5h | 72 % |
| 9 | | 5i R = Me | 88 % |
| 10 | | 5j R = Cl | 77 % |
| 11 | | 5k R = OMe | 93 % |
| 12 | | 5l | 62 % |
| 13 | | 5m | 87 % |

[a] Reaction conditions: 0.1 mmol amine, 0.13 mmol alcohol, 1.5 mg Ni/CdS/TiO₂@MIL-101, Ar, 0.15 mL CH₃CN, 27 °C, 48 h, 470 nm blue LED 50 W. The yields were determined by GC using n-decane as internal standard.

The reaction of benzyl alcohol and aniline was chosen to optimize the reaction conditions. Imines (**5**) were obtained in good yields under very mild conditions at room temperature. A notable functional group tolerance was again observed without the use of additives or sacrificial electron donors. Methyl, methoxy, halide, and hydroxyl-substituted benzyl alcohols were well tolerated. Additionally, we varied the amine component tolerating methyl, halogen, and methoxy substituents. We analysed the gas atmosphere to quantify the amount of the hydrogen released for selected examples (Supporting Information, Table S8). Amines formed via hydrogenation of the imines by the hydrogen liberated were not observed.

6.3 Conclusions

In conclusion, we introduced photocatalytic C-N multiple bond formation under visible light illumination. Hydrogen is liberated quantitatively and the reaction takes place at room temperature, conditions under which one would expect imine hydrogenation rather than dehydrogenation employing a thermally operating catalyst. A noble metal-free photocatalyst has been developed to accomplish this reaction. It is composed of a Ni/CdS/TiO₂ junction assembled on the metal-organic framework MIL-101 as a colloidal porous support. The reusable photocatalyst also permits hydrogen generation from alcohols (alcohol splitting) under very mild conditions, inert gas atmosphere, and without the requirement of sacrificial electron donors. We observed a broad substrate scope with very good tolerance of functional groups and high selectivity. We believe our reusable photocatalyst represents a valuable platform for a variety of photocatalytic C-N or C-C bond formation reactions which involve the dehydrogenation of alcohols and condensation reaction(s) as key steps.

Acknowledgements

This work was supported by grants from the Deutsche Forschungsgemeinschaft (DFG, SFB 840, B1). The authors also acknowledge the support of the DAAD, Colloid/Polymer Network, the help of Florian Puchtler (XRD), Dr. Jürgen Seidel (XPS), and Eduard Arzt for his support through INM.

6.4 References

- [1] C. Gunanathan, D. Milstein, *Science* **2013** *341*, 1229712.
- [2] T. P. Vispute, H. Zhang, A. Sanna, R. Xiao, G. W. Huber, *Science* **2010**, *330*, 1222–1227.
- [3] C. O. Tuck, E. Perez, I. T. Horvath, R. A. Sheldon, M. Poliakoff, *Science* **2012**, *337*, 695–699.
- [4] S. Michlik, R. Kempe, *Nat. Chem.* **2013**, *5*, 140–144.
- [5] a) B. Gnanaprakasam, J. Zhang, D. Milstein, *Angew. Chem. Int. Ed.* **2010**, *49*, 1468–1472; *Angew. Chem.* **2010**, *122*, 1510–1513; b) A. Mukherjee, A. Nerush, G. Leitus, L. J. W. Shimon, Y. Ben David, N. A. Espinosa Jalapa, D. Milstein, *J. Am. Chem. Soc.* **2016**, *138*, 4298–4301.
- [6] Pyrrole synthesis: a) D. Forberg, J. Obenauf, M. Friedrich, S. M. Hühne, W. Mader, G. Motz, R. Kempe, *Catal. Sci. Technol.* **2014**, *4*, 4188–4192; b) F. Kallmeier, B. Dudziec, T. Irrgang, R. Kempe, *Angew. Chem. Int. Ed.* **2017**, *56*, 7261–7265; *Angew. Chem.* **2017**, *129*, 7367–7371; for selected work of others see: c) D. Srimani, Y. Ben-David, D. Milstein *Angew. Chem. Int. Ed.* **2013**, *52*, 4012–4015; *Angew. Chem.* **2013**, *125*, 4104–4107; d) M. Zhang, H. Neumann, M. Beller, *Angew. Chem. Int. Ed.* **2013**, *52*, 597–601; *Angew. Chem.* **2013**, *125*, 625–629; e) M. Zhang, X. Fang, H. Neumann, M. Beller, *J. Am. Chem. Soc.* **2013**, *135*, 11384–11388.
- [7] Pyridine synthesis: a) S. Michlik, R. Kempe, *Angew. Chem. Int. Ed.* **2013**, *52*, 6326–6329; *Angew. Chem.* **2013**, *125*, 6450–6454; b) T. Hille, T. Irrgang, R. Kempe, *Angew. Chem. Int. Ed.* **2017**, *56*, 371–374; *Angew. Chem.* **2017**, *129*, 377–381; for selected work of others see: c) D. Srimani, Y. Ben-David, D. Milstein, *Chem. Commun.* **2013**, *49*, 6632–6634.
- [8] Pyrimidine synthesis: a) N. Deibl, K. Ament, R. Kempe, *J. Am. Chem. Soc.* **2015**, *137*, 12804–12807; b) N. Deibl, R. Kempe, *Angew. Chem. Int. Ed.* **2017**, *56*, 1663–1666; *Angew. Chem.* **2017**, *129*, 1685–1688; for selected work of others see: c) M. Mastalir, M. Glatz, E. Pittenauer, G. Allmaier, K. Kirchner, *J. Am. Chem. Soc.* **2016**, *138*, 15543–15546.
- [9] a) G. Zhang, S. K. Hanson, *Org. Lett.* **2013**, *15*, 650–653; b) J. Bain, P. Cho, A. Voutchkova-Kostal, *Green Chem.* **2015**, *17*, 2271–2280; c) P. Daw, S.

- Chakraborty, J. A. Garg, Y. Ben-David, D. Milstein, *Angew. Chem. Int. Ed.* **2016**, *55*, 14373–14377; *Angew. Chem.* **2016**, *128*, 14585–14589; d) M. Mastalir, M. Glatz, N. Gorgas, B. Stöger, E. Pittenauer, G. Allmaier, L. F. Veiros, K. Kirchner, *Chem. Eur. J.* **2016**, *22*, 12316–12320; e) S. Parua, S. Das, R. Sikari, S. Sinha, N. D. Paul, *J. Org. Chem.* **2017**, *82*, 7165–7175.
- [10] Z. Jiang, J. Liu, M. Gao, X. Fan, L. Zhang, J. Zhang, *Adv. Mater.* **2017**, *29*, 1603369.
- [11] G. Férey, C. Mellot-Draznieks, C. Serre, F. Millange, J. Dutour, S. Surblé, I. Margiolaki, *Science* **2005**, *309*, 2040–2042.
- [12] For an example of a TiO₂/MIL-101 core-shell material see: D. Tilgner, R. Kempe, *Chem. Eur. J.* **2017**, *23*, 3184–3190.
- [13] a) T. P. A. Ruberu, N. C. Nelson, I. I. Slowing, J. Vela, *J. Phys. Chem. Lett.* **2012**, *3*, 2798–2802; b) T. Mitkina, C. Stanglmair, W. Setzer, M. Gruber, H. Kisch, B. König, *Org. Biomol. Chem.* **2012**, *10*, 3556–3561; c) Z. Chai, T.-T. Zeng, Q. Li, L.-Q. Lu, W.-J. Xiao, D. Xu, *J. Am. Chem. Soc.* **2016**, *138*, 10128–10131.
- [14] a) W. Zhai, S. Xue, A. Zhu, Y. Luo, Y. Tian, *ChemCatChem* **2011**, *3*, 127–130; b) S. Higashimoto, Y. Tanaka, R. Ishikawa, S. Hasegawa, M. Azuma, H. Ohue, Y. Sakata, *Catal. Sci. Technol.* **2013**, *3*, 400–403; c) Z. Liu, J. Caner, A. Kudo, H. Naka, S. Saito, *Chem. Eur. J.* **2013**, *19*, 9452–9456; d) A. Tanaka, S. Sakaguchi, K. Hashimoto, H. Kominami, *ACS Catal.* **2013**, *3*, 79–85; e) H. Kasap, C. A. Caputo, B. C. M. Martindale, R. Godin, V. W.-h. Lau, B. V. Lotsch, J. R. Durrant, E. Reisner, *J. Am. Chem. Soc.* **2016**, *138*, 9183–9192; f) L. M. Zhao, Q. Y. Meng, X. B. Fan, C. Ye, X. B. Li, B. Chen, V. Ramamurthy, C. H. Tung, L. Z. Wu, *Angew. Chem. Int. Ed.* **2017**, *56*, 3020–3024; *Angew. Chem.* **2017**, *129*, 3066–3070, g) G. Han, Y.-H. Jin, R. A. Burgess, N. E. Dickenson, X.-M. Cao, Y. Sun, *J. Am. Chem. Soc.* **2017** (DOI: 10.1021/jacs.7b08657).
- [15] J. Hermannsdörfer, M. Friedrich, R. Kempe, *Chem. Eur. J.* **2013**, *19*, 13652–13657.
- [16] D. R. Baker, P. V. Kamat, *Adv. Funct. Mater.* **2009**, *19*, 805–811.

6.5 Supporting Information

Experimental Procedures

General Methods

All chemicals and solvents were purchased commercially from chemical suppliers with purity over 95 % and used without further purification. All manipulations including air or moisture sensitive compounds were carried out under dry and oxygen-free argon atmosphere (Schlenk techniques) or in a nitrogen-filled glovebox (mBraun 120) with a high-capacity recirculator (below 0.1 ppm of oxygen and water).

Elemental analysis was performed by standard protocols employing microwave assisted digestion (7 min at 170 °C (80 % power), 7 min at 180 °C (85 % power), and 20 min at 195 °C (90 % power)) in HCl (32 %, 4.5 mL), HNO₃ (65 %, 1.5 mL), and HF (40 %, 1.0 mL). The resulting solution was analysed by inductively coupled plasma optical emission spectrometry (ICP-OES) using a Vista-Pro radial (Varian). Fourier transform infrared (FTIR) spectroscopy measurements were performed with a Cary 630 FTIR spectrometer (Agilent Technologies) over a range from 2000 cm⁻¹ to 550 cm⁻¹. Gas chromatography (GC) analyses were performed using an Agilent Technologies 6850 gas chromatograph equipped with a flame ionization detector (FID) and a MN Optima 17 capillary column (30.0 m x 0.32 mm x 0.25 μm) using n-dodecane or n-decane as internal standard. GC-MS analyses were performed using an Agilent Technologies 6890 gas chromatograph with a MN-MS HP-5 capillary column (30.0 m x 0.32 mm x 0.25 μm) and a coupled mass spectrometer as detector. Gas mixtures were analysed using a 6890N gas chromatograph (Agilent Technologies) equipped with an Agilent special Plot + Molsieve capillary column (30.0 m x 0.32 mm x 0.25 μm). Methane was used as internal standard. Nitrogen physisorption isotherms were determined at -196 °C using a Nova 2000e (Quantachrome) apparatus. Specific surface areas (SSA) were calculated by using p/p₀-values from 0.05-0.25 by the BET model. Specific total pore volumes were measured by DFT calculations (N₂ at -196 °C on silica (cylindr. pore, NLDFT equilibrium model)). Transmission electron microscopy (TEM) measurements were carried out using a LEO 922O microscope (Zeiss, 200 kV). The samples were suspended in chloroform and sonicated for 5 min. 2 μL of the suspension were placed on a CF200-Cu-grid or a LC200-

Cu-grid (Electron Microscopy Sciences) and allowed to dry. High-angle annular dark-field scanning transmission electron microscopy (HAADF-STEM) measurements were performed using a ARM200F (JEOL, 200 kV) equipped with a spherical aberration corrector (CEOS) and an energy-dispersed X-ray analysis (EDX) system (JEOL). Diffuse reflectance ultraviolet-visible spectra were measured using a CARY 300 (Agilent Technologies) with an Ulbricht sphere in the range of 450 to 800 nm. X-ray powder diffraction (XRD) analysis was performed using a XPERT-PRO diffractometer (Panalytical) ($\text{CuK}\alpha$ radiation, 1.54178 Å). The reference card numbers for comparison are 00-021-1272 for TiO_2 and 01-080-0019 for CdS. X-ray photoelectron spectroscopy (XPS) measurements were performed using a Specs Phoibos 150 R6 spectrometer equipped with HSA 3500 and MCD-9 detectors, a Specs Focus 500 monochromator, and a XR50M X-ray source ($\text{AlK}\alpha$, 13 kV, 200 W).

Material Synthesis

Synthesis of MIL-101

MIL-101 was synthesized according to our previous work in order to maintain an average crystallite size of 300 nm.^[S1] chromium(III) nitrate nonahydrate (640 mg, 1.60 mmol), terephthalic acid (265 mg, 1.60 mmol), hydrofluoric acid 40 wt.-% (10 μL , 0.228 mmol), and deionized H_2O (8.00 mL) were sealed in a 23 mL Teflon-lined hydrothermal autoclave. The mixture was heated for 1 h at 80 °C (heating rate: 1.7 °C min^{-1}) and for 7.45 h at 220 °C (4.7 °C min^{-1}). The reaction mixture was cooled down fast to 160 °C and slowly to 30 °C (cooling rate: 5.4 °C h^{-1}). Excessively crystallized H_2BDC was removed by filtration over a pore 3 filter. The product was separated from the reaction solution by centrifugation (2000 rpm, 45 min). The MIL-101 was refluxed in ethanol/water (90/10 vol.-%) for 15 h and centrifugalized (1800 rpm, 45 min) to remove the α -CrOOH impurities and to separate the MIL-101 crystals with different size distribution. The green product was dried under vacuum (10^{-4} mbar, 85 °C) (BET: 2820 $\text{m}^2 \text{g}^{-1}$).

Synthesis of TiO_2 @MIL-101

TiO_2 @MIL-101 was synthesized according to our previous work.^[S2] Dry MIL-101 powder (400 mg) was placed in a two-chamber-tube with titanium(IV) isopropoxide (0.64 mL) separated by a glass frit. The gas phase infiltration of the TiO_2 precursor

occurred at 32 °C in dynamic vacuum (10^{-4} mbar) for 20 h. The resulting bright green powder was processed in hydrolysis by thermal treatment under H₂O atmosphere at 80 °C. The material was evacuated (10^{-4} mbar) at 85 °C for 20 h, transferred into a 125 mL Teflon-lined hydrothermal autoclave with 50 mL of deionized water, and heated at 150 °C for 10 h (heating rate: 2.0 °C min⁻¹). After cooling down to room temperature, the material was dried under vacuum (10^{-4} mbar, 85 °C). The Ti precursor infiltration, hydrolysis, and hydrothermal treatment described was performed one more time to yield TiO₂@MIL-101.

Synthesis of CdS/TiO₂@MIL-101, CdS@MIL-101, and CdS/TiO₂

200 mg dry TiO₂@MIL-101, MIL-101, or TiO₂ (anatase, acquired commercial) was suspended in 35 mL of dimethyl sulfoxide in a 125 mL Teflon-lined hydrothermal autoclave. 250 mg cadmium(II) acetate dihydrate were added and the reaction mixture was stirred for 2 h. The mixture was heated at 180 °C for 10 h (heating rate: 2.5 °C min⁻¹). After cooling down to room temperature, the resulting CdS/TiO₂@MIL-101 was separated by filtration and washed with ethanol. The material was combined with 40 mL of ethanol and heated at 100 °C for 10 h (heating rate: 1.2 °C min⁻¹) in a 125 mL Teflon-lined hydrothermal autoclave. After cooling down, the material was separated by filtration and dried (10^{-4} mbar, 85 °C).

Synthesis of Ni/CdS/TiO₂@MIL-101, Ni/CdS@MIL-101, Ni/TiO₂@MIL-101, Ni/CdS/TiO₂, Ni/CdS, and Ni/TiO₂

150 mg dry CdS/TiO₂@MIL-101, CdS@MIL-101, TiO₂@MIL-101, CdS/TiO₂, CdS (cubic, acquired commercial), or TiO₂ (anatase, acquired commercial) was placed in a two-chamber-tube with bis(cyclopentadienyl)nickel(II) (20 mg) separated by a glass frit. The gas phase infiltration of the Ni precursor occurred at room temperature (25 °C) in static vacuum (10^{-4} mbar) for 20 h. The reduction of the Ni precursor was performed under hydrogen atmosphere (10 bar H₂) at 90 °C for 20 h in a Parr Instruments steel autoclave. The resulting Ni/CdS/TiO₂@MIL-101 was evacuated (10^{-4} mbar, 85 °C) for 20 h in order to remove former metal ligand recess.

Synthesis of Pd/CdS/TiO₂@MIL-101

The synthesis of Pd/CdS/TiO₂@MIL-101 was performed as described for Ni/CdS/TiO₂@MIL-101 using allyl(cyclopentadienyl)palladium(II) (17 mg). The reduction of the Pd precursor was performed at 10 bar H₂.

Synthesis of Pt/CdS/TiO₂@MIL-101

The synthesis of Pt/CdS/TiO₂@MIL-101 was performed as described for Ni/CdS/TiO₂@MIL-101 using Trimethyl(methylcyclopentadienyl)platinum(IV) (15 mg). The reduction of the Pt precursor was performed at 10 bar H₂.

Synthesis of Au/CdS/TiO₂@MIL-101

150 mg dry CdS/TiO₂@MIL-101 powder was placed in a two-chamber-tube with Chlorocarbonylgold(I) (24 mg) separated by a glass installation. The gas phase infiltration of the Au precursor occurred at 45 °C in static vacuum (10⁻⁴ mbar) for 20 h. The reduction of the Au precursor was performed under hydrogen atmosphere (20 bar H₂) at 90 °C for 20 h in a Parr Instruments steel autoclave. The resulting Au/CdS/TiO₂@MIL-101 was evacuated (10⁻⁴ mbar, 85 °C) for 20 h in order to remove former metal ligand recess.

General Procedure for Photocatalytic Experiments

General procedure for the photocatalytic hydrogen generation by alcohol oxidation

A 10 mL reaction vial was charged with a magnetic stir bar, Ni/CdS/TiO₂@MIL-101 catalyst (0.6 mg), and alcohol (0.1 mmol). The vial was sealed with a rubber septum, evacuated to remove the air atmosphere, and flushed with argon for 2 min. Dry and degassed acetonitrile (0.3 mL) was added and the vial was further purged with argon for 1 min. The vial was illuminated for 24 h by a 50 W blue LED (470 nm, distance 5 cm, ~15000 lx) and cooled by a fan (Figure S9). The reaction temperature was measured to be 27 °C. N-dodecane (10 µL, 44 µmol) was added as internal standard and the catalyst was separated from the reaction solution by centrifugation (9000 rpm, 9 min) before quantitative analysis by GC. The amount of H₂ evolved was determined by injecting 500 µL of methane as internal standard before LED illumination. The gas phase of the reaction was analysed by GC-TDC. Regarding the oxidation of 2-propanol, 7.7 µL

(0.1 mmol) of dry and degassed alcohol were added after the evacuation of the vial and dehydrogenated without solvent.

Benzyl alcohol (0.3 mmol, 31.2 μ L) and 0.5 mg catalyst were illuminated for 20 h for the comparison of different catalysts (Figure 2a).

Reusability of the Ni/CdS/TiO₂@MIL-101 photocatalyst

A 10 mL reaction vial was charged with a magnetic stir bar, Ni/CdS/TiO₂@MIL-101 catalyst (4 mg), and benzyl alcohol (0.1 mmol). The vial was sealed with a rubber septum, evacuated to remove the air atmosphere, and flushed with argon for 2 min. Dry and degassed acetonitrile (0.5 mL) was added and the vial was further purged with argon for 1 min. The vial was illuminated for 5 h by a 50 W blue LED (470 nm, distance 5 cm, ~15000 lx) and cooled by a fan (Figure S9). N-dodecane (10 μ L, 44 μ mol) was added as internal standard and the catalyst was separated from the reaction solution by centrifugation (9000 rpm, 9 min) before quantitative analysis by GC. The catalyst was purified with acetonitrile between the runs.

General procedure for the photocatalytic synthesis of imines

A 10 mL reaction vial was charged with a magnetic stir bar, Ni/CdS/TiO₂@MIL-101 catalyst (1.5 mg), amine (0.1 mmol), and alcohol (0.13 mmol). The vial was sealed with a rubber septum, evacuated to remove the air atmosphere, and flushed with argon for 2 min. Dry and degassed acetonitrile (0.15 mL) was added and the vial was further purged with argon for 1 min. The vial was illuminated for 48 h by a 50 W blue LED (470 nm, distance 5 cm, ~15000 lx) and cooled by a fan (Figure S9). The reaction temperature was measured to be 27 °C. N-decane (10 μ L, 51 μ mol) was added as internal standard and the catalyst was separated from the reaction solution by centrifugation (9000 rpm, 9 min) before quantitative analysis by GC. The amount of H₂ evolved was determined by injecting 500 μ L of methane as internal standard before LED illumination. The gas phase of the reaction was analysed by GC-TDC.

Material Characterization

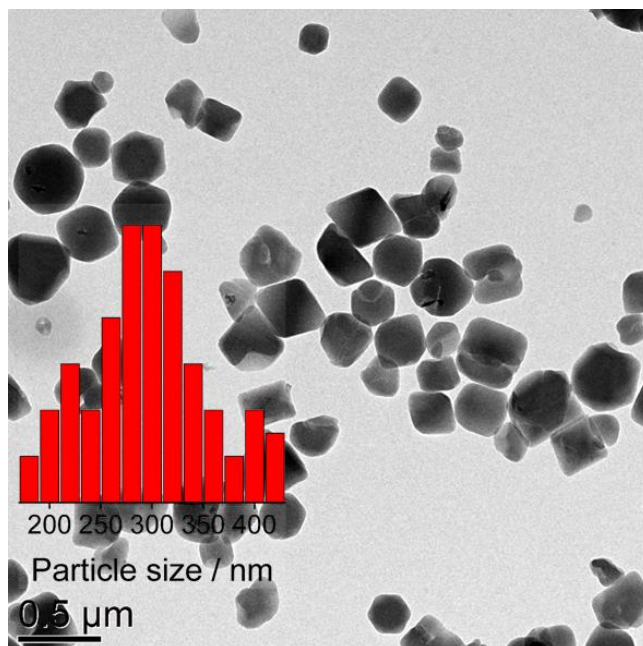


Figure S1. TEM analysis of the as-synthesized MIL-101 crystallites with an average diameter of 300 nm.

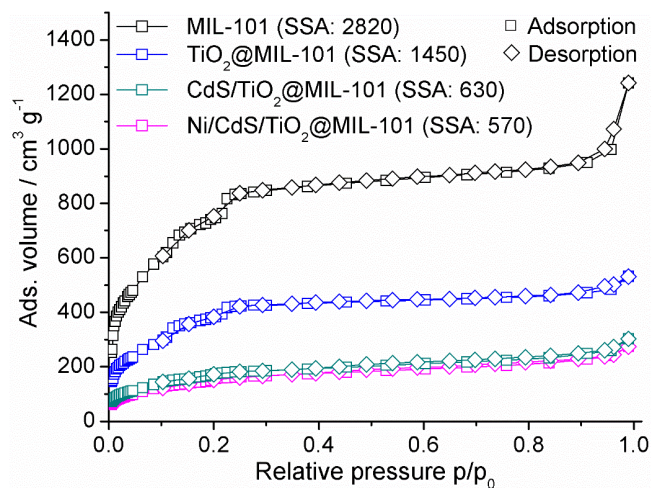


Figure S2. Nitrogen physisorption isotherms of MIL-101, TiO₂@MIL-101, CdS/TiO₂@MIL-101, and Ni/CdS/TiO₂@MIL-101 with the respective specific surface areas (SSA given in m² g⁻¹) determined by the BET model.

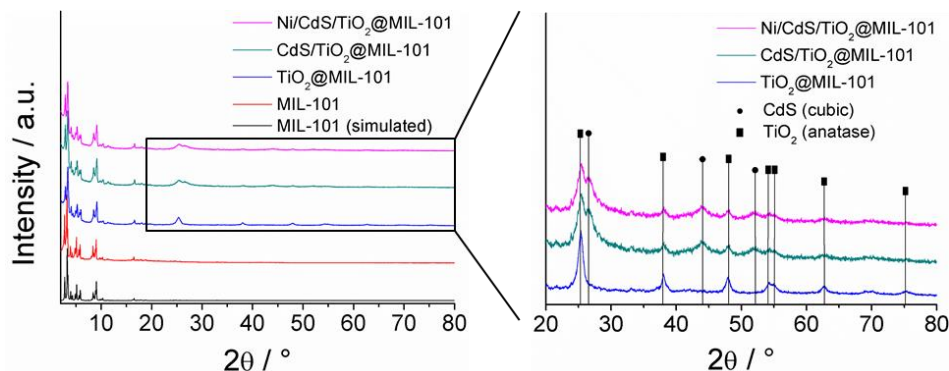


Figure S3. XRD spectra of MIL-101, TiO₂@MIL-101, CdS/TiO₂@MIL-101, and Ni/CdS/TiO₂@MIL-101 with the characteristic reflexes of MIL-101, cubic CdS (Ref. 01-080-0019) and anatase TiO₂ (Ref. 00-021-1272).

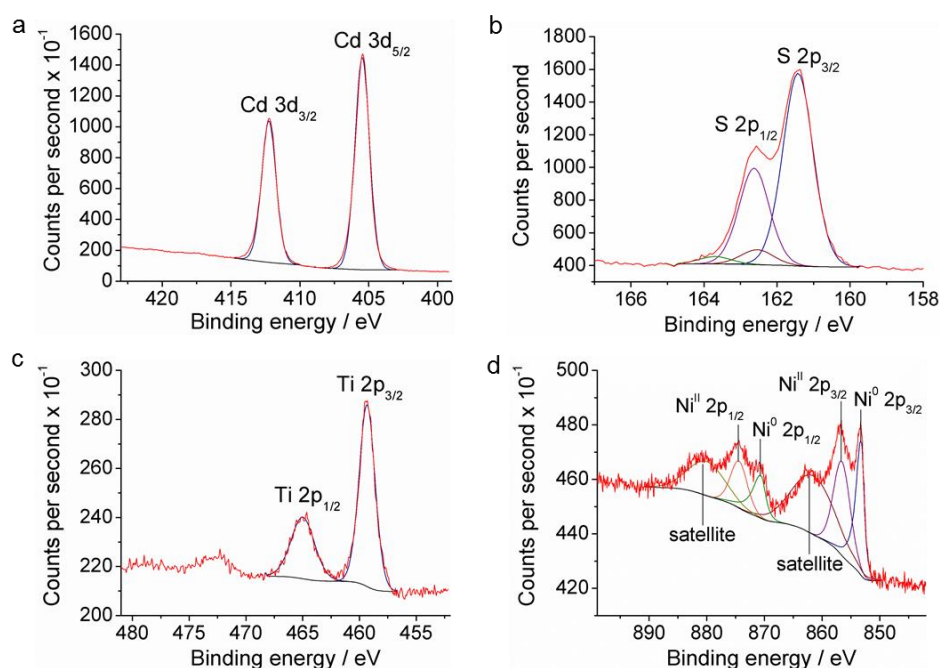


Figure S4. XPS spectra of Ni/CdS/TiO₂@MIL-101 in a) the Cd 3d region, b) the S 2p region, c) the Ti 2p region and, d) the Ni 2p region.

Table S1. ICP-OES analysis of TiO₂@MIL-101, CdS/TiO₂@MIL-101, and M/CdS/TiO₂@MIL-101 (M = Ni, Pd, Pt, Au) with contents given in wt.-%.

| Material | Cr | Ti | TiO ₂ ^[a] | Cd | CdS ^[a] | Ni | Pd | Pt | Au |
|----------------------------------|------|------|---------------------------------|------|--------------------|-----|-----|-----|-----|
| TiO ₂ @MIL-101 | 11.2 | 25.0 | 41.7 | - | - | - | - | - | - |
| CdS/TiO ₂ @MIL-101 | 7.9 | 17.8 | 29.7 | 16.2 | 20.8 | - | - | - | - |
| Ni/CdS/TiO ₂ @MIL-101 | 7.3 | 15.6 | 26.0 | 14.6 | 18.8 | 3.6 | - | - | - |
| Pd/CdS/TiO ₂ @MIL-101 | 6.8 | 16.4 | 27.4 | 15.6 | 20.0 | - | 4.3 | - | - |
| Pt/CdS/TiO ₂ @MIL-101 | 8.2 | 15.1 | 25.2 | 14.3 | 18.4 | - | - | 3.1 | - |
| Au/CdS/TiO ₂ @MIL-101 | 7.1 | 14.7 | 24.5 | 14.8 | 19.0 | - | - | - | 5.6 |

[a] Calculated on the basis of the Ti and Cd content.

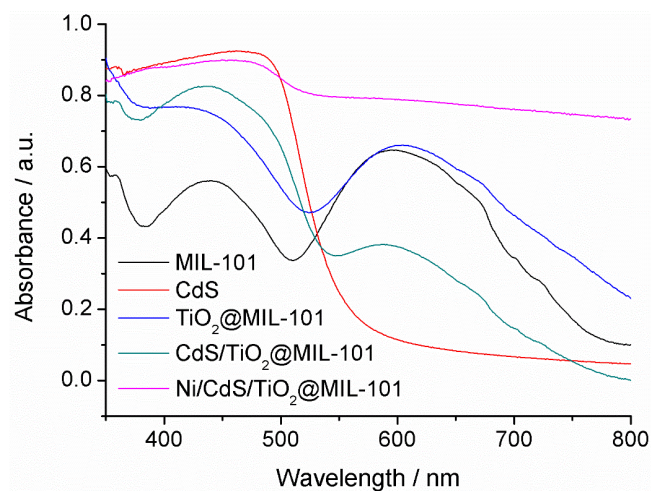


Figure S5. Diffuse reflectance ultraviolet-visible spectra of MIL-101, CdS (cubic), TiO₂@MIL-101, CdS/TiO₂@MIL-101, and Ni/CdS/TiO₂@MIL-101.

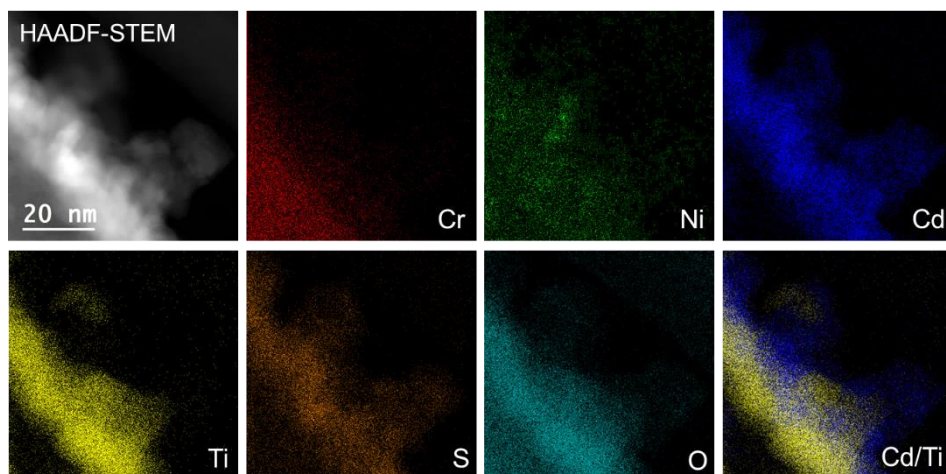


Figure S6. HAADF-STEM analysis of Ni/CdS/TiO₂@MIL-101 with representative EDX element maps.

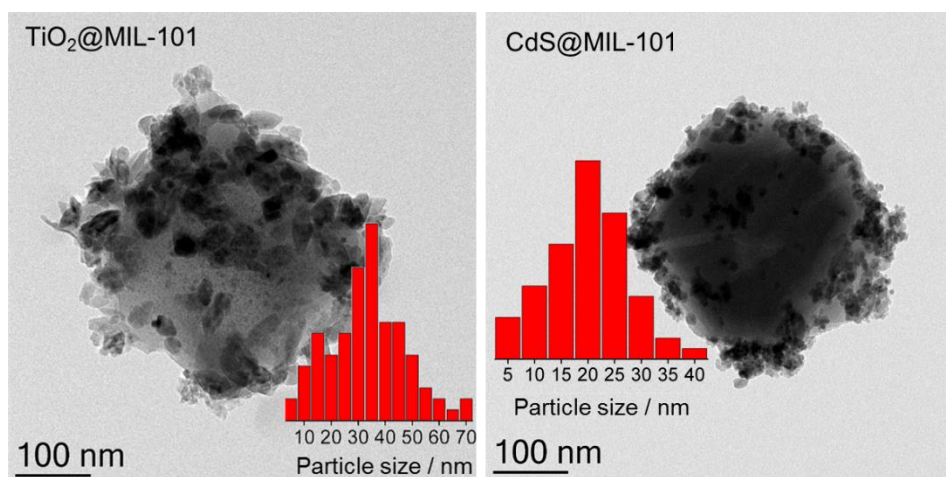


Figure S7. TEM micrographs of TiO₂@MIL-101 and CdS@MIL-101 with the respective particle size distribution.

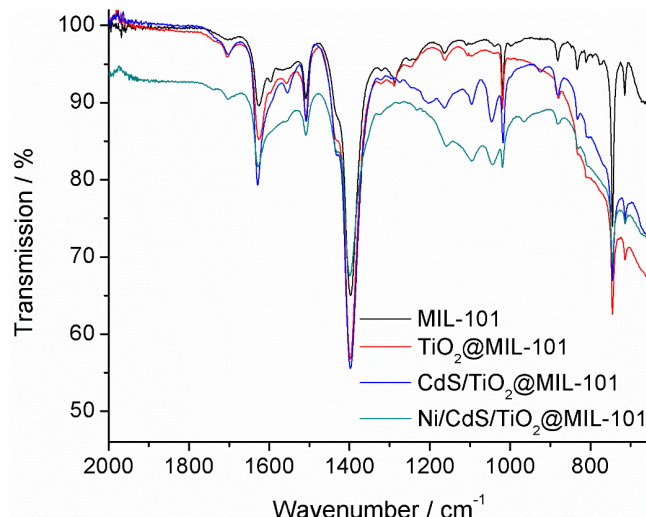


Figure S8. FTIR spectra of MIL-101, TiO₂@MIL-101, CdS/TiO₂@MIL-101, and Ni/CdS/TiO₂@MIL-101.

Photocatalytic Experiments

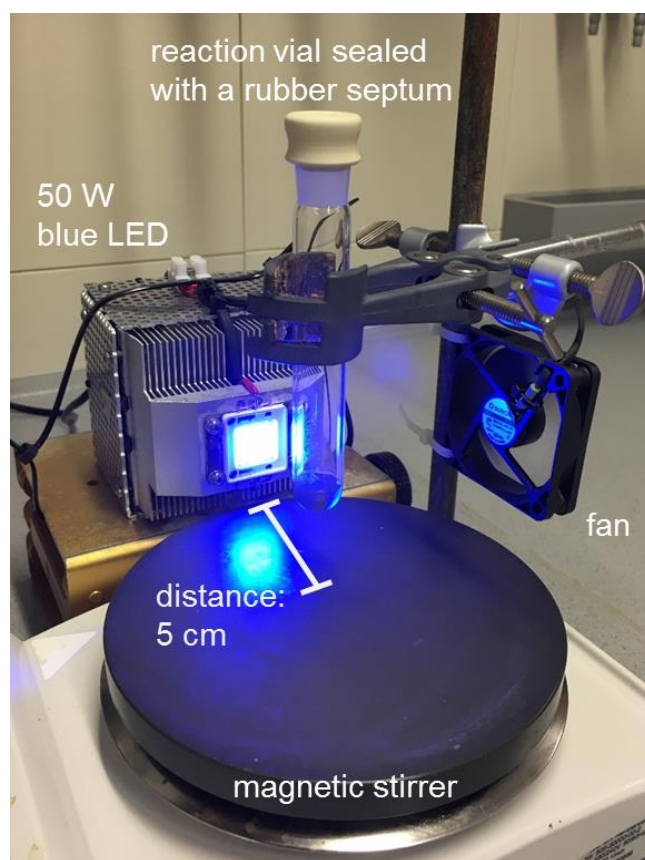


Figure S9. Experimental setup for photocatalytic experiments. The reaction vials sealed with a rubber septum were illuminated by a 50 W blue LED (470 nm, distance 5 cm, ~15000 lx), stirred magnetically, and cooled by a fan.

We performed control experiments to investigate whether O₂ is inserted into the reaction vials by diffusion through the rubber septa during catalysis. Therefore, we prepared several experiments in a nitrogen-filled glovebox using the same amount of catalyst, substrate, and solvent as described in the supplementary methods section and sealed the reaction vials with a greased glass plug. The yields of the reactions prepared in the glove box were equal to the yields prepared according to the supplementary methods section using a rubber septum. Consequently, no entry of O₂ was observed, which would have influenced the reactions (for example the yields). Additionally, no entry of O₂ was observed during the analysis of the evolved amount of H₂ by GC-TDC.

Table S2. Solvent screening for the photocatalytic dehydrogenation of benzyl alcohol.^[a]

c1ccc(cc1)CO >> c1ccc(cc1)C=O + H2

| Entry | Solvent | Yield ^[b] [%] |
|----------|---------------------|--------------------------|
| 1 | Diglyme | 14 |
| 2 | Acetonitrile | 53 |
| 3 | Toluene | 34 |
| 4 | Tetrahydrofurane | 12 |
| 5 | Dimethoxyethane | 15 |
| 6 | 1,4-Dioxane | 6 |
| 7 | No solvent | 33 |

[a] Reaction conditions: 0.20 mmol Benzyl alcohol, 0.5 mg Ni/CdS/TiO₂@MIL-101, Ar, 0.30 mL solvent, 27 °C, 20 h, 470 nm blue LED 50 W. [b] Determined by GC using n-dodecane as internal standard.

Table S3. Screening of the Ni amount for the photocatalytic dehydrogenation of benzyl alcohol.^[a]

| Entry | Catalyst ^[c] | Yield ^[b] [%] |
|-------|--|-----------------------------|
| 1 | Ni/CdS/TiO ₂ @MIL-101 (2 wt% Ni) | 64 |
| 2 | Ni/CdS/TiO₂@MIL-101 (4 wt% Ni) | 73 |
| 3 | Ni/CdS/TiO ₂ @MIL-101 (6 wt% Ni) | 52 |

[a] Reaction conditions: 0.3 mmol benzyl alcohol, 0.5 mg catalyst, 0.5 mL solvent, Ar, 24 h, 27 °C, 470 nm blue LED 50 W. [b] Determined by GC using n-dodecane as internal standard. [c] The Ni content was calculated based on the amount of precursor.

Table S4. Catalyst screening for the photocatalytic dehydrogenation of benzyl alcohol.^[a]

| Entry | Catalyst | Yield ^[b] [%] |
|-------|---|-----------------------------|
| 1 | Ni/CdS/TiO₂@MIL-101 | 73 |
| 2 | Pd/CdS/TiO ₂ @MIL-101 | 16 |
| 3 | Pt/CdS/TiO ₂ @MIL-101 | 21 |
| 4 | Au/CdS/TiO ₂ @MIL-101 | 8 |
| 5 | CdS/TiO ₂ @MIL-101 | 13 |
| 6 | CdS@MIL-101 | 6 |
| 7 | Ni/CdS@MIL-101 | 29 |
| 8 | Ni/TiO ₂ @MIL-101 | 0 |
| 9 | MIL-101 | 0 |
| 10 | CdS ^[c] | 5 |
| 11 | Ni/CdS ^[c] | 15 |
| 12 | Ni/CdS ^[c] + TiO ₂ ^[d] | 10 |
| 13 | Ni/TiO ₂ | 0 |

| | | |
|----|---|----|
| 14 | Ni + CdS ^[c] + TiO ₂ ^[d] | 6 |
| 15 | Ni/CdS/TiO ₂ ^[d] | 21 |
| 16 | TiO ₂ (P25) | 0 |

[a] Reaction conditions: 0.3 mmol benzyl alcohol, 0.5 mg catalyst, 0.5 mL solvent, Ar, 24 h, 27 °C, 470 nm blue LED 50 W. [b] Determined by GC using n-dodecane as internal standard. [c] Commercial available cubic CdS. [d] Commercial available TiO₂ (anatase).

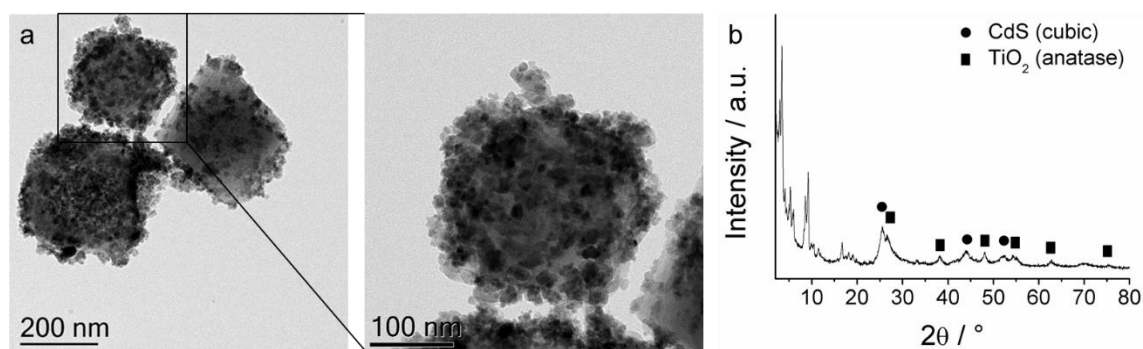


Figure S10. a) TEM micrographs of the Ni/CdS/TiO₂@MIL-101 catalyst reused for the photocatalytic dehydrogenation of benzyl alcohol for ten runs. b) XRD analysis of the reused catalyst.

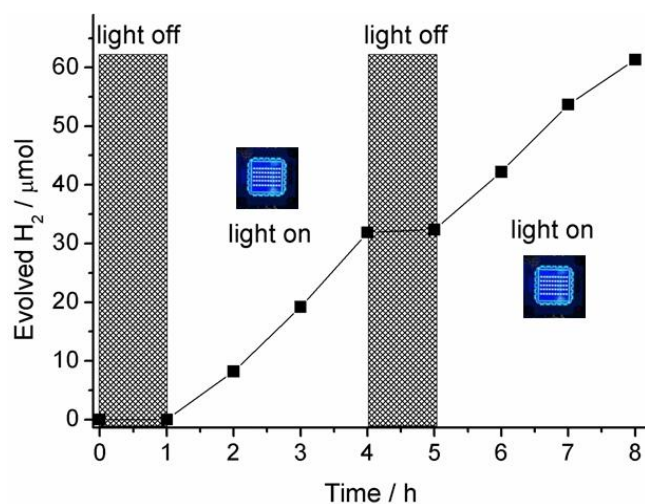


Figure S11. Light on/off experiment. Hydrogen evolution from benzyl alcohol was only observed under light illumination (4.0 mg Ni/CdS/TiO₂@MIL-101, 0.3 mmol benzyl alcohol, 0.3 mL CH₃CN, Ar, 50 W blue LED).

Table S5. Photocatalytic dehydrogenation of additional alcohols.^[a]

| Entry | Product | R | Yield ^[b] [%] |
|-------------------|---------|--|-----------------------------|
| 1 | | R ¹ = OMe, R ² = H | >99 |
| 2 | | R ¹ = H, R ² = OMe | 93 |
| 3 | | R ¹ = Me, R ² = H | >99 |
| 4 | | R ¹ = H, R ² = Me | 82 |
| 5 | | R ¹ = F, R ² = H | 87 |
| 6 | | R ¹ = Cl, R ² = H | >99 |
| 7 ^[c] | | R ¹ = H, R ² = Cl | 87 |
| 8 ^[c] | | R ¹ = Br, R ² = H | 96 |
| 9 ^[c] | | R ¹ = OH, R ² = H | 83 |
| 10 | | R ¹ = H, R ² = OH | 87 |
| 11 ^[d] | | R ¹ = H, R ² = CF ₃ | 89 |
| 12 ^[c] | | | 78 |
| 13 | | | 85 |
| 14 ^[d] | | | 92 |
| 15 ^[d] | | | 83 |
| 16 ^[e] | acetone | | 64 ^[f] |

[a] Reaction conditions: 0.1 mmol alcohol, 0.6 mg Ni/CdS/TiO₂@MIL-101, Ar, 0.3 mL CH₃CN, 27 °C, 24 h, 470 nm blue LED 50 W. [b] Determined by GC using n-dodecane as internal standard. [c] 1.2 mg Ni/CdS/TiO₂@MIL-101. [d] 1.2 mg Ni/CdS/TiO₂@MIL-101, 48 h. [e] Without solvent, 72 h. [f] Determined by the evolved amount of H₂ using methane as internal standard (GC-TCD).

Table S6. Hydrogen generation via photocatalytic dehydrogenation of alcohols.^[a]

$$\text{R}'\text{-CH(OH)-R}'' \xrightarrow[\text{CH}_3\text{CN, Ar, } h\nu (470 \text{ nm})]{\text{Ni/CdS/TiO}_2\text{@MIL-101}} \text{R}'\text{-C(=O)-R}'' + \text{H}_2\uparrow$$

| Entry | Product | R | Yield ^[b] [μmol] | H ₂ ^[c] [μmol] |
|-------|---------|--|---|--|
| 1 | | R ¹ = H, R ² = H | 97 | 92 |
| 2 | | R ¹ = OMe, R ² = H | 96 | 88 |
| 3 | | R ¹ = Cl, R ² = H | 97 | 85 |
| 4 | | | 93 | 77 |
| 5 | | | 88 | 78 |
| 6 | | R ¹ = H, R ² = H | >99 | 93 |
| 7 | | R ¹ = Me, R ² = H | >99 | 94 |
| 8 | | R ¹ = H, R ² = NH ₂ | 96 | 84 |
| 9 | | R ¹ = OH, R ² = H | 83 | 71 |

[a] Reaction conditions: 0.1 mmol alcohol, 0.6 mg Ni/CdS/TiO₂@MIL-101, Ar, 0.3 mL CH₃CN, 27 °C, 24 h, 470 nm blue LED 50 W. [b] Determined by GC using n-dodecane as internal standard. [c] Determined using methane as internal standard (GC-TCD).

Table S7. Screening of the alcohol:amine ratio for the synthesis of imines.^[a]

$$\text{C}_6\text{H}_5\text{CH}_2\text{OH} + \text{C}_6\text{H}_5\text{NH}_2 \xrightarrow[\text{CH}_3\text{CN, Ar, } h\nu (470 \text{ nm})]{\text{Ni/CdS/TiO}_2\text{@MIL-101}} \text{C}_6\text{H}_5\text{CH=N-C}_6\text{H}_5 + \text{H}_2 + \text{H}_2\text{O}$$

| Entry | alcohol:amine | Yield ^[b] [%] |
|----------|---------------|-----------------------------|
| 1 | 1:1 | 36 |
| 2 | 1.1:1 | 41 |
| 3 | 1.2:1 | 49 |
| 4 | 1.3:1 | 66 |
| 5 | 1.4:1 | 65 |

[a] 0.1 mmol aniline, benzyl alcohol, 1.5 mg Ni/CdS/TiO₂@MIL-101, Ar, 0.15 mL CH₃CN, 27 °C, 30 h, 470 nm blue LED 50 W. [b] Determined by GC using n-decane as internal standard.

Table S8. Hydrogen liberation during the photocatalytic synthesis of imines from alcohols and amines.^[a]

$$\text{R}'\text{-CH}_2\text{-OH} + \text{H}_2\text{N-R}'' \xrightarrow[\text{-H}_2, \text{-H}_2\text{O}]{\text{Ni/CdS/TiO}_2\text{@MIL-101, CH}_3\text{CN, Ar, } h\nu \text{ (470 nm)}} \text{R}'\text{-CH=N-R}''$$

| Entry | Product | R | Yield ^[b] [%] | H ₂ ^[c] [μmol] |
|-------|---------|---------|--------------------------|--------------------------------------|
| 1 | | R = H | 92 | 113 |
| 2 | | R = Me | 86 | 107 |
| 3 | | R = Cl | 88 | 95 |
| 4 | | R = Me | 88 | 107 |
| 5 | | R = OMe | 93 | 117 |
| 6 | | | 87 | 113 |

[a] Reaction conditions: 0.1 mmol amine, 0.13 mmol alcohol, 1.5 mg Ni/CdS/TiO₂@MIL-101, Ar, 0.15 mL CH₃CN, 27 °C, 48 h, 470 nm blue LED 50 W. [b] Determined by GC using n-decane as internal standard. [c] Determined using methane as internal standard (GC-TCD). The benzyl alcohol derivatives (0.13 mmol) were completely oxidized to the corresponding aldehydes.

References

- [S1] J. Hermannsdörfer, M. Friedrich, R. Kempe, *Chem. Eur. J.* **2013**, *19*, 13652–13657.
- [S2] D. Tilgner, R. Kempe, *Chem. Eur. J.* **2017**, *23*, 3184–3190.

7 A Metal-Organic Framework-Based Nonprecious Metal Photocatalyst for Visible Light-Driven Wastewater Treatment

Dominic Tilgner,^[a] Martin Friedrich,^[a] Andreas Verch,^[b] Niels de Jonge,^[b,c] and Rhett Kempe*^[a]

[a] Inorganic Chemistry II, Catalyst Design, University of Bayreuth, Universitätsstraße 30, 95440 Bayreuth (Germany).

[b] INM – Leibniz Institute for New Materials, University Bayreuth, Campus D2 2, 66123 Saarbrücken (Germany).

[c] Department of Physics, Saarland University, Campus A5 1, 66123 Saarbrücken (Germany).

Submitted to *ChemPhotoChem*.

Keywords: photocatalysis; wastewater treatment; metal-organic frameworks; titanium dioxide; iron oxide

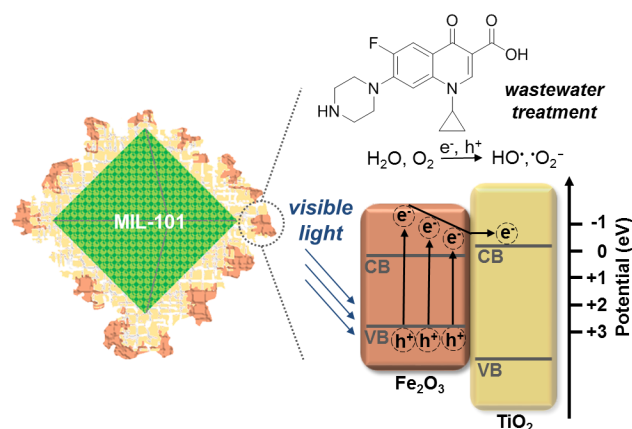
Abstract: The utilization of abundantly available elements in key technologies is a promising way to save precious and rare metals. Iron and titanium offer the highest abundance of all transition metals in the earth's crust and their application in catalytic processes is preferable regarding sustainable material development. The photocatalytic decontamination of wastewater using visible light-responsive materials is of high interest due to the demand for clean water and the increasing accumulation of harmful organic compounds resulting from medical or industrial waste. Herein, we report on a novel photocatalyst based on the generation of crystalline Fe₂O₃ and TiO₂ on size-optimized colloidal metal-organic framework crystallites. The reusable photocatalyst permits the efficient oxidative degradation of pharmaceutical compounds and toxic dyes under visible light illumination and without the requirement of additives or noble metals. We observed a higher photocatalytic activity for our Fe₂O₃/TiO₂@MIL-101 material than for commercially available Fe₂O₃, TiO₂, and TiO₂ (P25).

7.1 Introduction

The conservation of our rare element resources is essential regarding the sustainable development of our planet. The replacement of rare elements by abundantly available elements in key technologies is one of the options for the sustainable material synthesis. Catalysis is a key technology with a high need for noble metals.^[1] Rare noble metals, such as Pt, Ir, and Ru are frequently used for photocatalysis.^[2] Fe and Ti are the two transition metals of the earth crust which appear most and their combination to accomplish efficient visible light-driven photocatalysis is highly desirable.^[3] We introduced a variety of metal-organic framework (MOF)-based materials for liquid-phase catalysis^[4] and photocatalysis^[5] recently and report herein on a novel photocatalyst employing the nonprecious metals Fe and Ti. The corresponding metal oxides Fe_2O_3 and TiO_2 were assembled on colloidal crystallites of the MOF or porous coordination polymer MIL-101 (Cr)^[6] as a tailored porous support material. We combined gas phase infiltration procedures of suitable Fe_2O_3 and TiO_2 precursors and subsequent metal oxide formation to synthesize the $\text{Fe}_2\text{O}_3/\text{TiO}_2@$ MIL-101 material. It is the first example of the generation of $\text{Fe}_2\text{O}_3/\text{TiO}_2$ on a MOF and we hold that such a support of semiconducting materials and the resulting heterojunction systems represents a promising platform for the generation of broadly applicable photocatalysts. We investigated our reusable photocatalyst for the visible light-driven degradation of the common pharmaceutical substances ciprofloxacin, levofloxacin, and diclofenac, and the dye rhodamine B in aqueous solution without additional additives. $\text{Fe}_2\text{O}_3/\text{TiO}_2@$ MIL-101 showed a higher photocatalytic activity than $\text{Fe}_2\text{O}_3@$ MIL-101, $\text{TiO}_2@$ MIL-101 or bare Fe_2O_3 (hematite), TiO_2 (anatase), and TiO_2 (P25). The development of sustainable technologies for wastewater recycling is of high significance due to the increasing demand of the growing earth population for clean water.^[7] Herein, the utilization of sunlight for the oxidative decontamination of harmful organic compounds represents an appealing approach and the generation of visible light-responsive materials for efficient wastewater treatment has attracted tremendous attention.^[8] The support of iron oxide or titanium dioxide on MOFs is regarded as a suitable method for the generation of photocatalysts applicable for wastewater treatment under visible light illumination.^[5b, 9]

7.2 Results and Discussion

We chose MIL-101 (Cr) as support material for the generation of a Fe₂O₃/TiO₂ hetero-junction because of the large pores suitable for the infiltration of the metal precursors and the stability during hydrothermal modifications. It was prepared according to a procedure described previously with an average crystallite size of 300 nm (Supporting Information, Figure S1), which was optimized regarding the catalytic performance.^[4d] The crystallites are large enough to ensure efficient separation for reusability and small enough to have a sufficiently large outer surface for modifications with Fe₂O₃ and TiO₂. The modification of the MIL-101 crystallites with Fe₂O₃ and TiO₂ is based on a two-step procedure. The first step involves the infiltration of suitable metal oxide precursors through the gas phase to ensure high and quantitative loadings and a homogeneous precursor distribution. After the subsequent decomposition of the precursor compounds by exposing them to air or moisture, the crystallization of Fe₂O₃ and TiO₂ on the surface of the MIL-101 crystallites was performed under hydrothermal conditions as the second step. First, we performed the generation of TiO₂@MIL-101 employing titanium(IV) isopropoxide as a volatile TiO₂ precursor. After the hydrothermal crystallization of TiO₂ around the surface of the MOF support at 150 °C, we generated Fe₂O₃ on the surface of TiO₂@MIL-101 using iron(0) pentacarbonyl as precursor to yield Fe₂O₃/TiO₂@MIL-101 with a core-shell morphology. Fe₂O₃ was incorporated as the visible light-absorbing component. It is widely accepted that excited electrons of Fe₂O₃ can be transferred into the conduction band of TiO₂ to ensure efficient charge carrier separation (Scheme 1).^[10]



Scheme 1. Illustration of the Fe₂O₃/TiO₂@MIL-101 photocatalyst with a core-shell morphology. The MOF-supported Fe₂O₃/TiO₂ junction system is an efficient material for wastewater treatment under visible light illumination.

The separated holes and electrons induce the formation of active hydroxyl radicals and superoxide radicals for the oxidative degradation of pollutants.^[11] The crystalline structure of the MIL-101 maintained after the modification with Fe₂O₃ and TiO₂ was investigated by X-ray powder diffraction (XRD) analysis (Supporting Information, Figure S2). While the reflexes from 2° to 20° (2θ) could be assigned to MIL-101, we further identified crystalline Fe₂O₃ (α-Fe₂O₃, hematite) and TiO₂ (anatase). The specific surface area and the initial pore volume of MIL-101 was decreased noticeably after the generation of the metal oxides indicating the partial filling or blocking of the MIL-101 pores (Supporting Information, Figure S3). The elemental composition of TiO₂@MIL-101 and Fe₂O₃/TiO₂@MIL-101 was determined by inductively coupled plasma optical emission spectrometry measurements (Supporting Information, Table S1). The final Fe₂O₃/TiO₂@MIL-101 material comprised 9.7 wt% Fe₂O₃, 38.9 wt% TiO₂, and 10.3 wt% Cr. Diffuse reflectance ultraviolet-visible (UV/Vis) spectra in a range from 450 to 800 nm showed an increased light absorption of the materials modified with Fe₂O₃ and TiO₂ in comparison to bare MIL-101 (Supporting Information, Figure S4). Thermogravimetric analysis showed a lower loss of material for Fe₂O₃/TiO₂@MIL-101 (35 %) than for MIL-101 (73 %), which is related to the metal oxide content (Supporting Information, Figure S5). We investigated the morphology of the Fe₂O₃/TiO₂@MIL-101 material by transmission electron microscopy (TEM) measurements (Figure 1a). The MIL-101 crystallites modified with Fe₂O₃ and TiO₂ still exhibited an octahedral shape and the MOF surface was covered homogeneously with the metal oxide particles. The spatial distribution of Fe₂O₃ and TiO₂ was investigated by high-angle annular dark-field scanning TEM (HAADF-STEM) measurements and the corresponding energy-dispersed X-ray element maps (Figure 1b-i). The MOF surface was covered entirely by Fe₂O₃ and TiO₂ in a core-shell morphology, while Fe₂O₃ formed agglomerates more differentiated compared to TiO₂. The direct interface between Fe₂O₃ and TiO₂ was also verified by the identification of the characteristic lattice planes. We analyzed the TiO₂@MIL-101 and Fe₂O₃@MIL-101 material by TEM measurements to get a rough impression of the magnitude of the Fe₂O₃ and TiO₂ particles formed on the surface of MIL-101 (Supporting Information, Figure S8). The average Fe₂O₃ particle size determined for Fe₂O₃@MIL-101 was smaller than for Fe₂O₃/TiO₂@MIL-101. This might be attributed to the reduced surface area of TiO₂@MIL-101 in comparison to MIL-101 during the Fe₂O₃ generation.

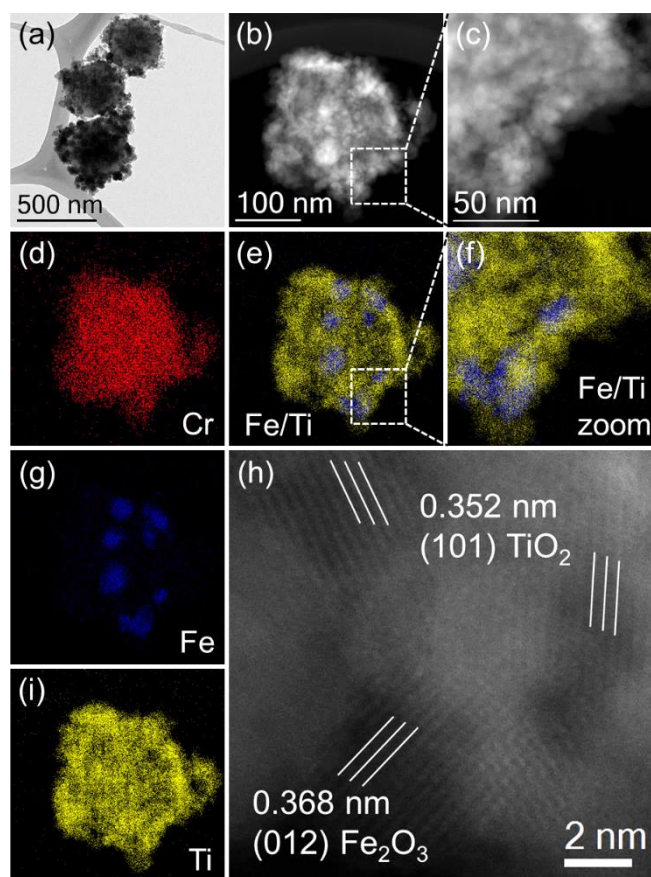


Figure 1. TEM micrograph of $\text{Fe}_2\text{O}_3/\text{TiO}_2@\text{MIL-101}$. The surface of the octahedral-shaped MIL-101 crystallites is covered entirely with Fe_2O_3 and TiO_2 particles (a). HAADF-STEM analysis of $\text{Fe}_2\text{O}_3/\text{TiO}_2@\text{MIL-101}$ with the representative energy-dispersed X-ray element maps and the characteristic lattice planes for crystalline Fe_2O_3 (hematite) and TiO_2 (anatase) (b-i).

We demonstrated the applicability of $\text{Fe}_2\text{O}_3/\text{TiO}_2@\text{MIL-101}$ for purification processes of clinical wastewater based on the degradation of commonly used pharmaceutical substances in aqueous solution. The degradation experiments were performed under air atmosphere and without the requirement of any additives at $\text{pH} = 7-8$. A 50 W blue LED (470 nm) was used as the visible light source for the degradation experiments, while the temperature of the reaction solution of 27°C was maintained by a fan (Supporting Information, Figure S10). The adsorption/desorption equilibrium between the contaminative compounds and the catalyst was achieved after stirring for 2 h without light. The photocatalytic reduction of the concentrations of the pharmaceuticals was analyzed by UV/Vis spectroscopy. We investigated the photocatalytic degradation of ciprofloxacin first to evaluate the activity of our MOF-supported materials regarding the Fe_2O_3 content (Supporting Information, Figure S11) and for comparison to commercially

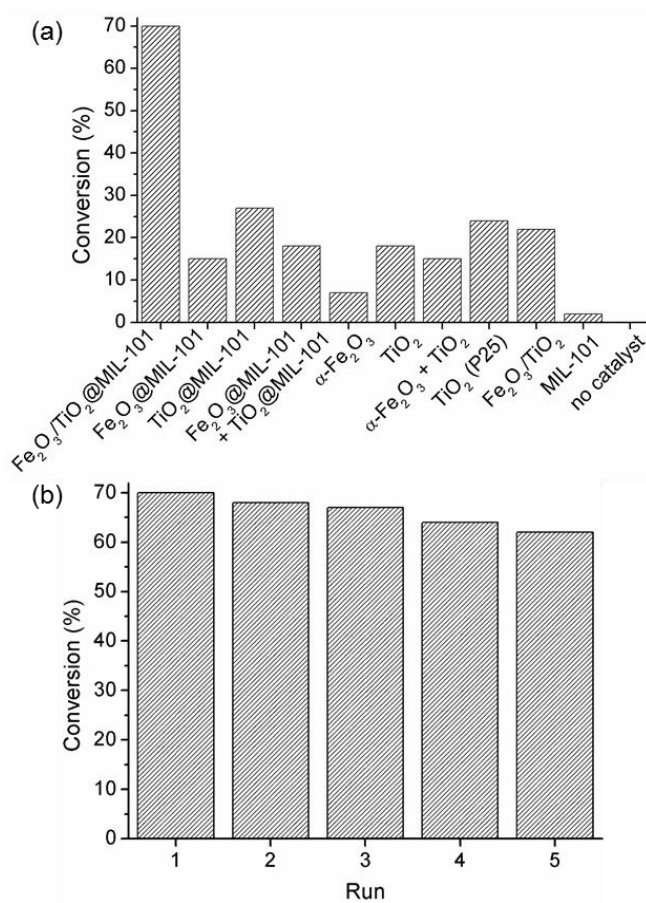


Figure 2. Comparison of different catalysts for the photocatalytic degradation of ciprofloxacin under visible light illumination. The conversions were determined by UV/Vis spectroscopy (a). Reusability of the Fe₂O₃/TiO₂@MIL-101 photocatalyst (b).

available Fe₂O₃ and TiO₂ (Figure 2a). The Fe₂O₃/TiO₂@MIL-101 photocatalyst showed a higher conversion than Fe₂O₃@MIL-101 and TiO₂@MIL-101, which highlights the beneficial arrangement of the two semiconducting materials on the MIL-101 surface. The support of Fe₂O₃ and TiO₂ on MIL-101 increased the photocatalytic activity in comparison to bare Fe₂O₃ (hematite), TiO₂ (anatase), or Fe₂O₃/TiO₂. Fe₂O₃/TiO₂@MIL-101 additionally showed a higher conversion than the commercially available TiO₂ (P25) photocatalyst. We investigated the reusability of the Fe₂O₃/TiO₂@MIL-101 material for the ciprofloxacin decontamination (Figure 2b). The photocatalyst was reused for five successive runs without a remarkable loss of activity. The material reused was analyzed by TEM and XRD measurements afterwards to verify the structural intactness (Supporting Information, Figure S13). The material still exhibited the octahedral-shaped crystallites with Fe₂O₃ and TiO₂ on the MIL-101 surface. The

crystallinity of the components was verified by XRD measurements. We surveyed the degradation of the antibiotic levofloxacin and the analgesic diclofenac as further model substrates for the photocatalytic treatment of clinical wastewater. The degradation of the xanthene dye rhodamine B was performed additionally to amplify the general applicability of the photocatalyst for wastewater purification (Figure 3a).

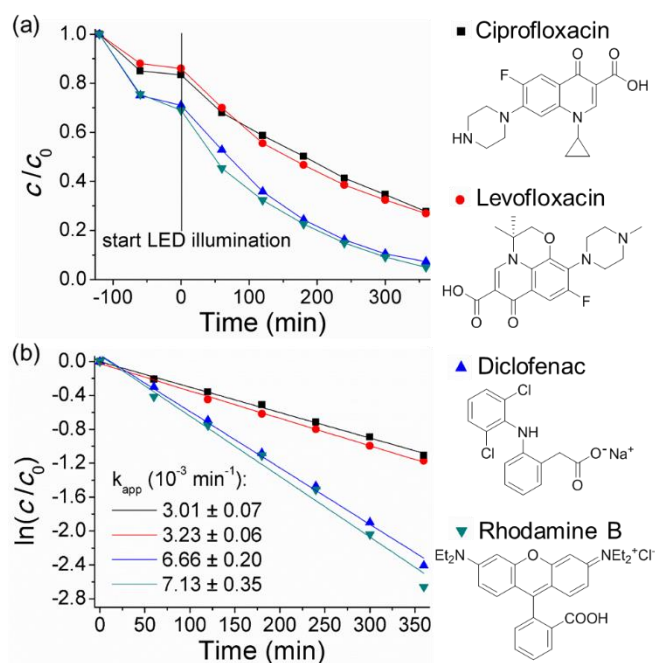


Figure 3. The decreasing concentrations of ciprofloxacin, levofloxacin, diclofenac, and rhodamine B during the photocatalytic degradation with $\text{Fe}_2\text{O}_3/\text{TiO}_2@\text{MIL-101}$. The adsorption/desorption equilibria between the organic compounds and the photocatalyst were maintained prior to the LED illumination (a). Kinetic degradation rates determined from $\ln(c/c_0)$ as a function of time (b).

The degradation reactions followed pseudo first-order kinetics approximately for the substrates described (Figure 3b). The rate constants determined for the degradation reactions were 3.01 ± 0.07 (10^{-3} min^{-1}) for ciprofloxacin, 3.23 ± 0.06 (10^{-3} min^{-1}) for levofloxacin, 6.66 ± 0.20 (10^{-3} min^{-1}) for diclofenac, and 7.13 ± 0.35 (10^{-3} min^{-1}) for rhodamine B. We performed control experiments to ensure the requirement of the photocatalyst and the visible light illumination for the water decontamination experiments presented. Therefore, we investigated the concentrations of the four model substrates under LED illumination without catalyst and without light in presence of catalyst

(Supporting Information, Figure S14-S17). The substrate concentrations remained constant for all control experiments.

7.3 Conclusions

In summary, we introduced a novel photocatalyst comprised of Fe₂O₃ (hematite) and TiO₂ (anatase). We could demonstrate the assembling of these two metal oxides on a MOF crystallite surface. The utilization of Fe and Ti, having the highest abundance of all transition metals of the earth crust, helps to preserve our precious metals, which are often the basis of visible light-sensitive photocatalysts. Our reusable photocatalyst Fe₂O₃/TiO₂@MIL-101 showed a higher activity for the visible light-driven degradation of antibiotics than bare Fe₂O₃ (hematite), TiO₂ (anatase), and commercially available TiO₂ (P25). Additionally, we observed an increased photocatalytic activity due to the support of Fe₂O₃ and TiO₂ on colloidal MIL-101 crystallites and no supplemental additives needed to be added for the oxidative pollutant degradation. Clinical wastewater treatment is a serious concern today and we believe that development of noble metal-free materials for photocatalytic water purification processes is a promising contribution in this context.

Acknowledgements

This work was supported by grants from the Deutsche Forschungsgemeinschaft (DFG, SFB 840, B1). The authors also acknowledge the support of the DAAD, Colloid/Polymer Network, the help of Florian Puchtler (XRD), and Eduard Arzt for his support through INM.

7.4 References

- [1] a) M. Zahmakran, S. Ozkar, *Nanoscale* **2011**, *3*, 3462–3481; b) M. Sankar, N. Dimitratos, P. J. Miedziak, P. P. Wells, C. J. Kiely, G. J. Hutchings, *Chem. Soc. Rev.* **2012**, *41*, 8099–8139; c) C. Gunanathan, D. Milstein, *Science* **2013**, *341*.
- [2] a) S. T. Kochuveedu, Y. H. Jang, D. H. Kim, *Chem. Soc. Rev.* **2013**, *42*, 8467–8493; b) D. M. Schultz, T. P. Yoon, *Science* **2014**, *343*, 1239176; c) X. Liu, J. Iocozzia, Y. Wang, X. Cui, Y. Chen, S. Zhao, Z. Li, Z. Lin, *Energy Environ. Sci.*

- 2017, 10, 402–434; d) J. Twilton, C. Le, P. Zhang, M. H. Shaw, R. W. Evans, D. W. C. MacMillan, *Nat. Rev. Chem.* **2017**, 1, 0052.
- [3] a) H. Tada, Q. Jin, H. Nishijima, H. Yamamoto, M. Fujishima, S. Okuoka, T. Hattori, Y. Sumida, H. Kobayashi, *Angew. Chem.* **2011**, 123, 3563–3567; *Angew. Chem. Int. Ed.* **2011**, 50, 3501–3505; b) K. E. deKrafft, C. Wang, W. Lin, *Adv. Mater.* **2012**, 24, 2014–2018; c) M. Liu, X. Qiu, M. Miyauchi, K. Hashimoto, *J. Am. Chem. Soc.* **2013**, 135, 10064–10072; d) M. Liu, R. Inde, M. Nishikawa, X. Qiu, D. Atarashi, E. Sakai, Y. Nosaka, K. Hashimoto, M. Miyauchi, *ACS Nano* **2014**, 8, 7229–7238; e) X. Li, H. Lin, X. Chen, H. Niu, J. Liu, T. Zhang, F. Qu, *Phys. Chem. Chem. Phys.* **2016**, 18, 9176–9185; f) R. Huang, R. Liang, H. Fan, S. Ying, L. Wu, X. Wang, G. Yan, *Sci. Rep.* **2017**, 7, 7858.
- [4] a) S. Proch, J. Hermannsdörfer, R. Kempe, C. Kern, A. Jess, L. Seyfarth, J. Senker, *Chem. Eur. J.* **2008**, 14, 8204–8212; b) J. Hermannsdörfer, R. Kempe, *Chem. Eur. J.* **2011**, 17, 8071–8077; c) J. Hermannsdörfer, M. Friedrich, N. Miyajima, R. Q. Albuquerque, S. Kümmel, R. Kempe, *Angew. Chem.* **2012**, 124, 11640–11644; *Angew. Chem. Int. Ed.* **2012**, 51, 11473–11477; d) J. Hermannsdörfer, M. Friedrich, R. Kempe, *Chem. Eur. J.* **2013**, 19, 13652–13657.
- [5] a) D. Tilgner, M. Friedrich, J. Hermannsdörfer, R. Kempe, *ChemCatChem* **2015**, 7, 3916–3922; b) D. Tilgner, R. Kempe, *Chem. Eur. J.* **2017**, 23, 3184–3190.
- [6] G. Férey, C. Mellot-Draznieks, C. Serre, F. Millange, J. Dutour, S. Surblé, I. Margiolaki, *Science* **2005**, 309, 2040–2042.
- [7] G. Tchobanous, F. L. Burton, R. Tsuchihashi, D. H. Stensel, *Wastewater Engineering Treatment and Reuse*, McGraw-Hill, New York, **2014**.
- [8] a) C. Chen, W. Ma, J. Zhao, *Chem. Soc. Rev.* **2010**, 39, 4206–4219; b) S. Dong, J. Feng, M. Fan, Y. Pi, L. Hu, X. Han, M. Liu, J. Sun, J. Sun, *RSC Adv.* **2015**, 5, 14610–14630; c) W. Wang, M. O. Tade, Z. Shao, *Chem. Soc. Rev.* **2015**, 44, 5371–5408; d) Z. Yang, F. Wang, C. Zhang, G. Zeng, X. Tan, Z. Yu, Y. Zhong, H. Wang, F. Cui, *RSC Adv.* **2016**, 6, 79415–79436.
- [9] a) C.-F. Zhang, L.-G. Qiu, F. Ke, Y.-J. Zhu, Y.-P. Yuan, G.-S. Xu, X. Jiang, *J. Mater. Chem. A* **2013**, 1, 14329–14334; b) H. Zhao, L. Qian, H. Lv, Y. Wang, G. Zhao, *ChemCatChem* **2015**, 7, 4148–4155; c) L. Qin, Z. Li, Z. Xu, X. Guo, G. Zhang, *Appl. Catal. B: Environ.* **2015**, 179, 500–508; d) C. Zhang, L. Ai, J. Jiang, *J. Mater. Chem. A* **2015**, 3, 3074–3081; e) X. Zhao, S. Liu, Z. Tang, H. Niu, Y.

- Cai, W. Meng, F. Wu, J. P. Giesy, *Sci. Rep.* **2015**, *5*, 11849; f) Z. Jin, W. Dong, M. Yang, J. Wang, H. Gao, G. Wang, *ChemCatChem* **2016**, *8*, 3510–3517; g) R. Panda, S. Rahut, J. K. Basu, *RSC Adv.* **2016**, *6*, 80981–80985; h) X. Li, Y. Pi, Q. Xia, Z. Li, J. Xiao, *Appl. Catal. B: Environ.* **2016**, *191*, 192–201; i) X. Feng, H. Chen, F. Jiang, *J. Colloid Interface Sci.* **2017**, *494*, 32–37; j) Y. Zhao, Y. Dong, F. Lu, C. Ju, L. Liu, J. Zhang, B. Zhang, Y. Feng, *J. Mater. Chem. A* **2017**, *5*, 15380–15389; k) J. Huang, H. Song, C. Chen, Y. Yang, N. Xu, X. Ji, C. Li, J.-A. You, *J. Environ. Chem. Eng.* **2017**, *5*, 2579–2585.
- [10] a) J.-Q. Li, D.-F. Wang, Z.-Y. Guo, Z.-F. Zhu, *Appl. Surf. Sci.* **2012**, *263*, 382–388; b) Y. Xia, L. Yin, *Phys. Chem. Chem. Phys.* **2013**, *15*, 18627–18634; c) P. Luan, M. Xie, D. Liu, X. Fu, L. Jing, *Sci. Rep.* **2014**, *4*, 6180; d) D. Barreca, G. Carraro, M. E. A. Warwick, K. Kaunisto, A. Gasparotto, V. Gombac, C. Sada, S. Turner, G. Van Tendeloo, C. Maccato, P. Fornasiero, *CrystEngComm* **2015**, *17*, 6219–6226.
- [11] a) Y. Wang, Y.-n. Zhang, G. Zhao, H. Tian, H. Shi, T. Zhou, *ACS Appl. Mater. Interfaces* **2012**, *4*, 3965–3972; b) W. Wang, Y. Liu, J. Qu, Y. Chen, M. O. Tadó, Z. Shao, *ChemPhotoChem* **2017**, *1*, 35–45; c) H. Zhao, Y. Chen, Q. Peng, Q. Wang, G. Zhao, *Appl. Catal. B: Environ.* **2017**, *203*, 127–137.

7.5 Supporting Information

Experimental Section

General Considerations

All chemicals and solvents were purchased commercially from chemical suppliers with purity >95 % and used without further purification. Iron(0) pentacarbonyl (>99 %) was obtained from Sigma-Aldrich. TiO₂ (anatase 99.9 %, 32 nm APS powder) was obtained from AlfaAesar. All manipulations including air or moisture sensitive compounds were carried out under dry and oxygen-free argon atmosphere (Schlenk techniques) or in a nitrogen-filled glovebox (mBraun 120) with a high-capacity recirculator (below 0.1 ppm of oxygen and water).

Elemental analysis was performed by standard protocols employing microwave assisted digestion (7 min at 170 °C (80 % power), 7 min at 180 °C (85 % power) and 20 min at

195 °C (90 % power)) in HCl (32 %, 4.5 mL), HNO₃ (65 %, 1.5 mL) and HF (40 %, 1.0 mL). The resulting solution was analysed by inductively coupled plasma optical emission spectrometry (ICP-OES) using a Vista-Pro radial (Varian). Fourier transform infrared (FTIR) spectroscopy measurements were performed with a Cary 630 FTIR spectrometer (Agilent Technologies) over a range from 2000 cm⁻¹ to 650 cm⁻¹. Nitrogen physisorption isotherms were determined at -196 °C using a Nova 2000e (Quantachrome) apparatus. Specific surface areas (SSA) were calculated by using p/p₀-values from 0.05-0.25 by the BET model. Specific total pore volumes were measured by DFT calculations (N₂ at -196 °C on silica (cylindr. pore, NLDFT equilibrium model)). Transmission electron microscopy (TEM) measurements were carried out using a LEO 9220 microscope (Zeiss, 200 kV). The samples were suspended in chloroform and sonicated for 5 min. 2 µL of the suspension were placed on a CF200-Cu-grid or a LC200-Cu-grid (Electron Microscopy Sciences) and allowed to dry. High-angle annular dark-field scanning transmission electron microscopy (HAADF-STEM) measurements were performed using a ARM200F (JEOL, 200 kV) equipped with a spherical aberration corrector (CEOS) and an energy-dispersed X-ray analysis (EDX) system (JEOL). Thermogravimetric analysis (TGA) was performed from 30 °C to 700 °C (5 °C min⁻¹) using a TGA/SDTA 851^e (Mettler) under air atmosphere. Diffuse reflectance ultraviolet-visible (UV/Vis) spectra were measured using a CARY 300 (Agilent Technologies) with an Ulbricht sphere in the range of 450 to 800 nm. UV-Vis spectra of solutions were measured using a CARY 60 (Agilent Technologies) with Scan-software and Hellma quartz glass cuvettes (12.5 mm x 12.5 mm x 45 mm). X-ray powder diffraction (XRD) analysis was performed using a XPERT-PRO diffractometer (Panalytical) (CuK_α radiation, 1.54178 Å). The reference card numbers for comparison are 00-021-1272 for TiO₂ and 00-033-0664 for Fe₂O₃.

Synthesis of MIL-101

MIL-101 was synthesized according to a previous work in order to maintain an average crystallite size of 300 nm.^[S1] chromium(III) nitrate nonahydrate (640 mg, 1.60 mmol), terephthalic acid (265 mg, 1.60 mmol), hydrofluoric acid 40 wt% (10 µL, 0.228 mmol) and deionized H₂O (8.00 mL) were sealed in a 23 mL Teflon-lined hydrothermal autoclave. The mixture was heated for 1 h at 80 °C (heating rate: 1.7 °C min⁻¹) and for

7.45 h at 220 °C (4.7 °C min⁻¹). The reaction mixture was cooled down fast to 160 °C and slowly to 30 °C (cooling rate: 5.4 °C h⁻¹). Excessively crystallized H₂BDC was removed by filtration over a pore 3 filter. The product was separated from the aqueous solution by centrifugation (2000 rpm, 45 min), refluxed in ethanol/water (90/10 vol.-%) for 15 h, and centrifugalized (1800 rpm, 45 min) to remove the α -CrOOH impurities and to separate the MIL-101 crystals with different size distribution. The green MIL-101 was dried under vacuum (10⁻⁴ mbar, 85 °C) (BET: 2840 m² g⁻¹).

Synthesis of TiO₂@MIL-101

TiO₂@MIL-101 was synthesized according to our previous work.^[S2] MIL-101 (400 mg) was placed in a two-chamber-tube with titanium(IV) isopropoxide (0.64 mL) separated by a glass frit. The gas phase infiltration of the TiO₂ precursor occurred at 32 °C in dynamic vacuum (10⁻⁴ mbar) for 20 h. The resulting bright green powder was processed in hydrolysis by thermal treatment under H₂O atmosphere at 80 °C. The material was evacuated (10⁻⁴ mbar) at 85 °C for 20 h, transferred into a 125 mL Teflon-lined hydrothermal autoclave with 50 mL of deionized water and heated at 150 °C for 10 h (heating rate: 2.0 °C min⁻¹). After cooling down to room temperature, the material was dried under vacuum (10⁻⁴ mbar, 85 °C). The Ti precursor infiltration, hydrolysis and hydrothermal treatment described was performed two times to yield TiO₂@MIL-101.

Synthesis of Fe₂O₃/TiO₂@MIL-101, Fe₂O₃/TiO₂, and Fe₂O₃@MIL-101

200 mg TiO₂@MIL-101, TiO₂ (anatase, AlfaAesar), or MIL-101 were placed in a two-chamber-tube with iron(0) pentacarbonyl (40 μ L) separated by a glass frit. The Fe precursor was frozen in liquid nitrogen and the tube was evacuated to 10⁻⁴ mbar. The gas phase infiltration of the Fe precursor occurred at 25 °C (room temperature) in static vacuum (10⁻⁴ mbar) for 2 h. The material was exposed to air for 24 h, transferred into a 125 mL Teflon-lined hydrothermal autoclave with 50 mL of deionized water and heated at 150 °C for 10 h (heating rate: 2.0 °C min⁻¹). After cooling down to room temperature, the material was dried under vacuum (10⁻⁴ mbar, 85 °C).

General procedure for the photocatalytic degradation experiments

A 100 mL glass tube was charged with a magnetic stir bar, Fe₂O₃/TiO₂@MIL-101 catalyst (9 mg) and aqueous antibiotic/dye solution (30 mL, 5·10⁻⁵ mol L⁻¹) under air atmosphere. The suspensions were stirred for 2 h under exclusion of light at room temperature (25 °C) in order to achieve the adsorption/desorption equilibrium. The pH measured was 7-8. The degradation experiments were performed in front of a 50 W blue LED (470 nm, distance 5 cm). The reaction temperature was maintained by a fan (Supporting Information Figure S10) and measured to be 27 °C. At given irradiation intervals, 1.00 mL of the suspension was taken out and the catalyst was separated by centrifugation at 9000 rpm for 9 min. UV/Vis spectra were measured from the supernatant solutions to determine the concentration of the antibiotic/dye based on the absorption maximum. The reusability of Fe₂O₃/TiO₂@MIL-101 was investigated using 2.5 mg of catalyst and aqueous ciprofloxacin solution (8 mL, 5·10⁻⁵ mol L⁻¹). The catalyst was purified with water between the runs.

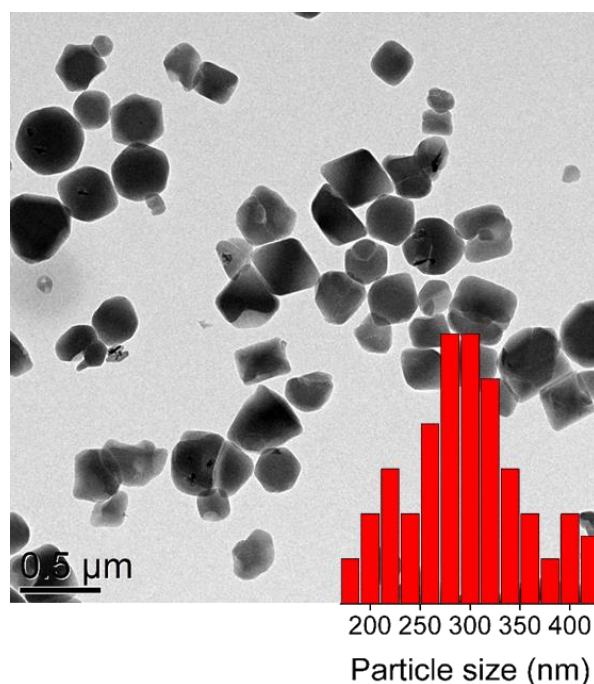


Figure S1. TEM analysis of the MIL-101 crystallites with an average crystallite size of about 300 nm.

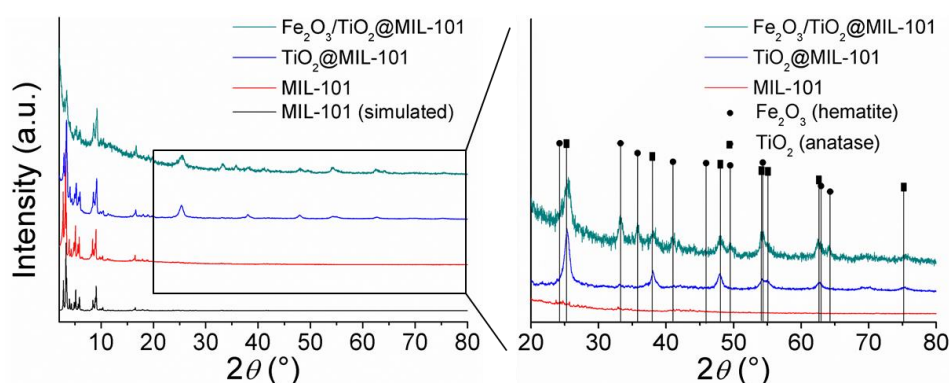


Figure S2. XRD analysis of MIL-101, TiO₂@MIL-101, and Fe₂O₃/TiO₂@MIL-101 with the characteristic reflexes of MIL-101, hematite Fe₂O₃ (Ref. 00-033-0664) and anatase TiO₂ (Ref. 00-021-1272).

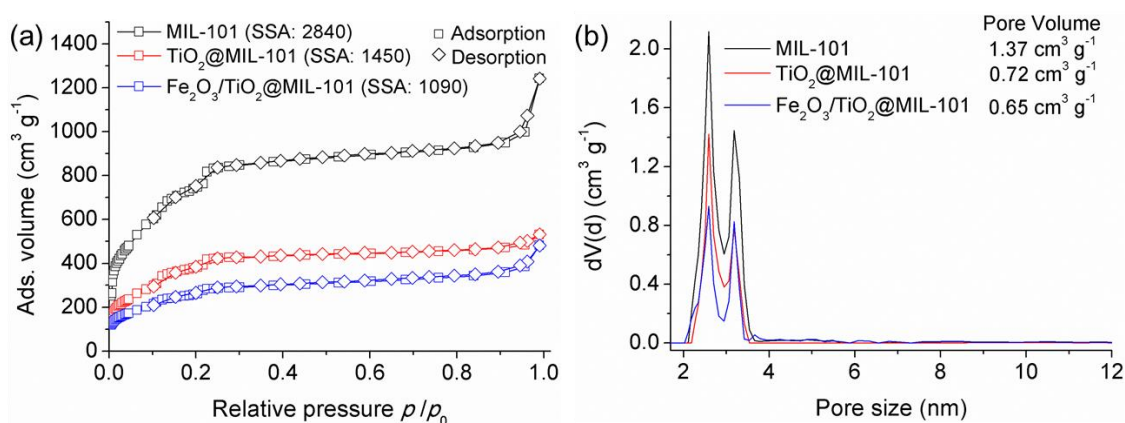


Figure S3. Nitrogen physisorption isotherms of MIL-101, TiO₂@MIL-101, and Fe₂O₃/TiO₂@MIL-101 with the respective specific surface areas (SSA given in m² g⁻¹) determined by the BET model. The normalized SSAs considering the MIL-101 content of the respective material (SSA g⁻¹ MIL-101) are 2480 cm³ g⁻¹ for TiO₂@MIL-101 and 2130 cm³ g⁻¹ for Fe₂O₃/TiO₂@MIL-101 indicating a partial filling of the pores (a). Pore size distributions and pore volumes of the materials determined by DFT calculations (b).

Table S1. ICP-OES analysis of TiO₂@MIL-101 and Fe₂O₃/TiO₂@MIL-101 with contents given in wt%.

| Material | Cr | Ti | TiO ₂ ^[a] | Fe | Fe ₂ O ₃ ^[a] |
|---|------|------|---------------------------------|-----|---|
| TiO ₂ @MIL-101 | 11.2 | 25.0 | 41.7 | - | - |
| Fe ₂ O ₃ /TiO ₂ @MIL-101 | 10.3 | 23.9 | 38.9 | 6.8 | 9.7 |

[a] Calculated on the basis of the Ti and Fe content.

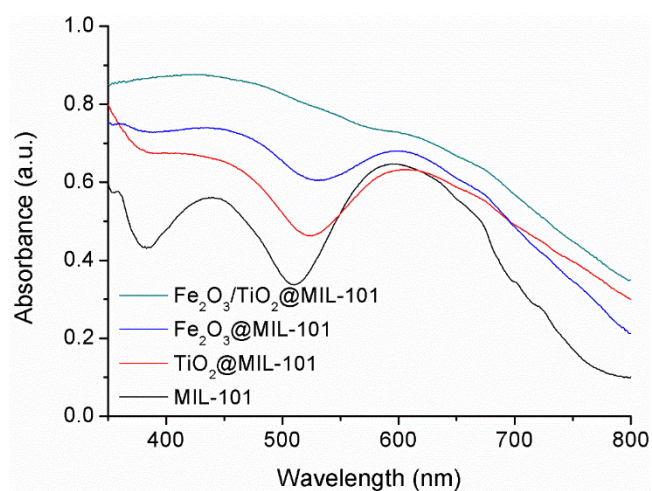


Figure S4. Diffuse reflectance UV/Vis spectra of MIL-101, TiO₂@MIL-101, Fe₂O₃@MIL-101, and Fe₂O₃/TiO₂@MIL-101.

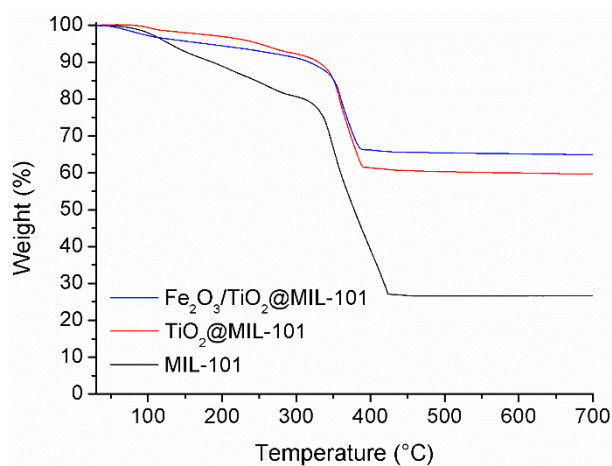


Figure S5. TGA measurements of MIL-101, TiO₂@MIL-101, and Fe₂O₃/TiO₂@MIL-101.

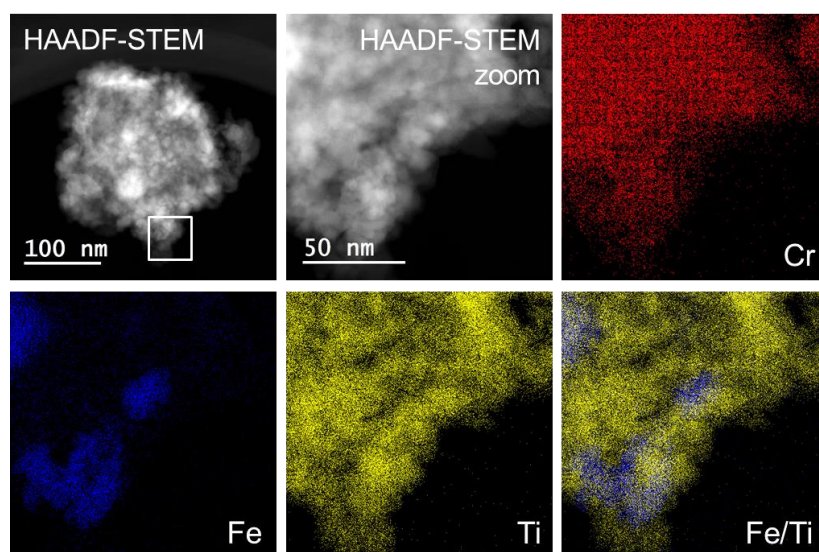


Figure S6. HAADF-STEM analysis of $\text{Fe}_2\text{O}_3/\text{TiO}_2@\text{MIL-101}$ with additional representative EDX element maps at higher magnification.

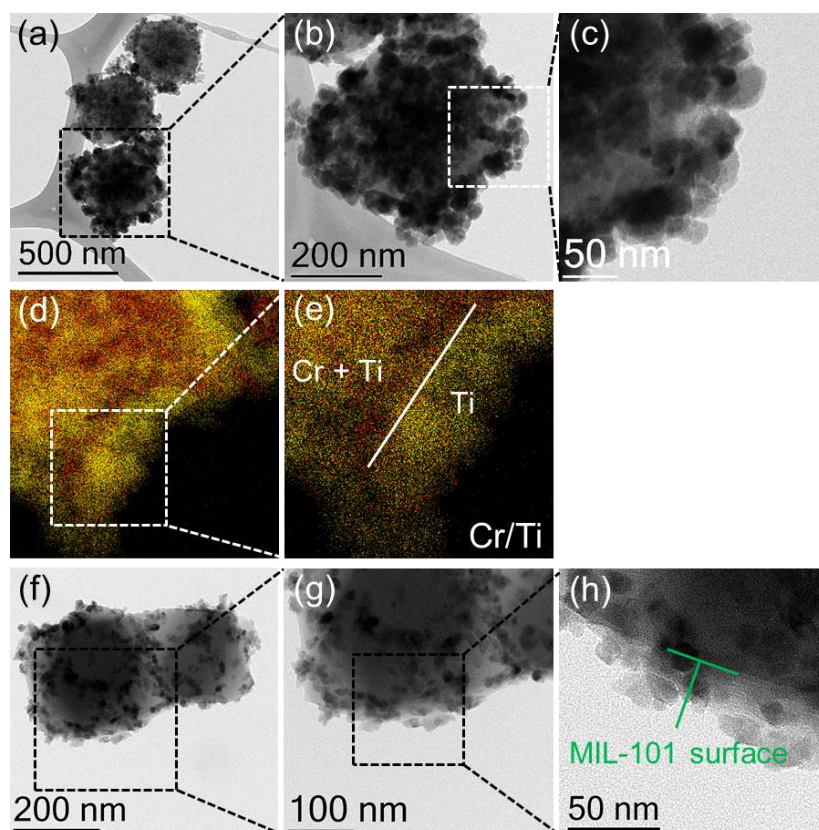


Figure S7. TEM and micrographs of the $\text{Fe}_2\text{O}_3/\text{TiO}_2@\text{MIL-101}$ material in a core-shell morphology (a-c). The HAADF-STEM analysis with the overlaying element maps of Cr (red) and Ti (yellow) additionally confirms the formation of a TiO_2 shell on the surface of the MIL-101 crystallites (d,e). TEM micrographs of $\text{TiO}_2@\text{MIL-101}$ after the synthesis protocol of TiO_2 preformed for one time showing the arrangement of the TiO_2 particles on the surface of the MIL-101 crystallites (f-h).

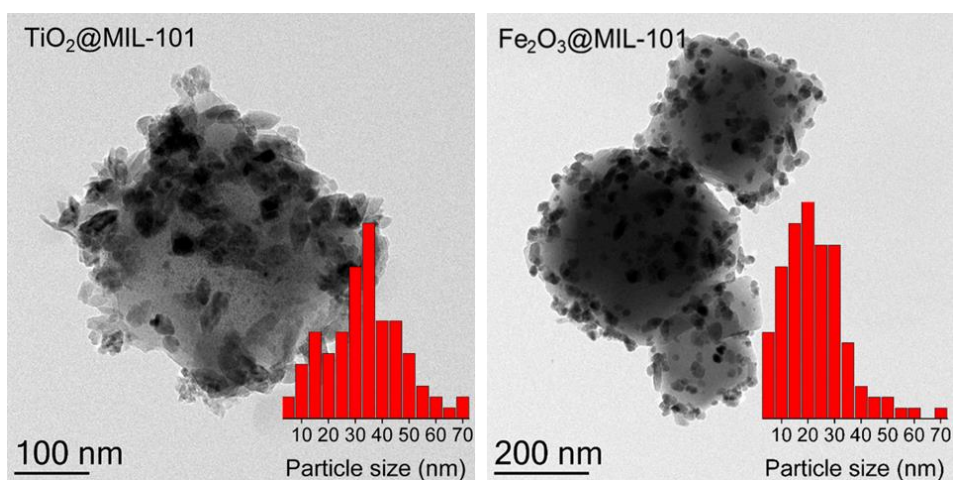


Figure S8. TEM micrographs of TiO₂@MIL-101 and Fe₂O₃@MIL-101 with the respective particle size distribution.

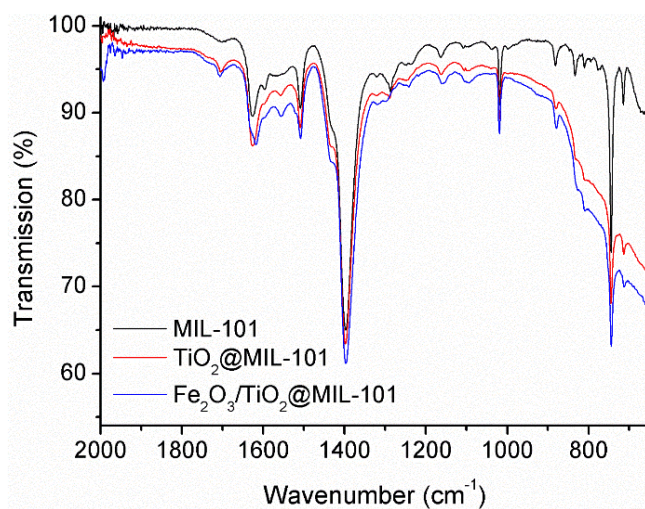


Figure S9. FTIR spectra of MIL-101, TiO₂@MIL-101, and Fe₂O₃/TiO₂@MIL-101.

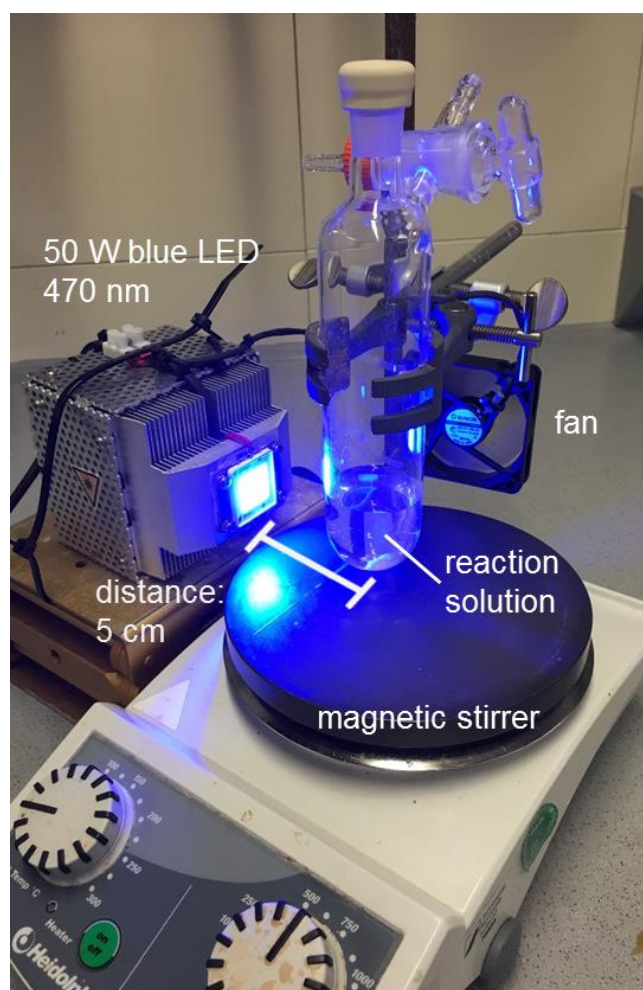


Figure S10. Experimental setup for the photocatalytic degradation experiments. The reaction vial was illuminated by a 50 W blue LED (470 nm, distance 5 cm, ~15000 lx), stirred magnetically, and cooled by a fan.

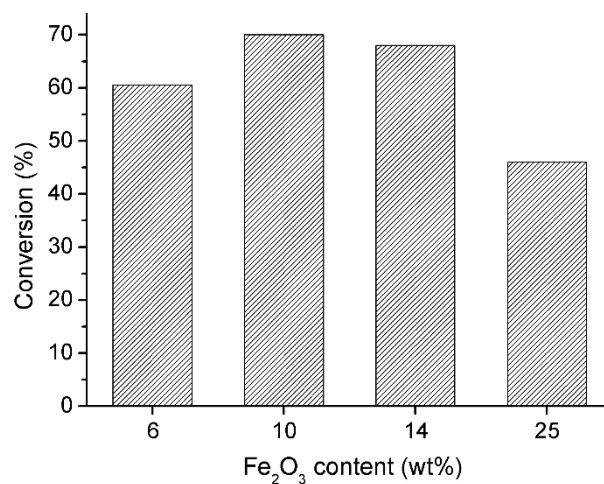


Figure S11. Screening of the Fe₂O₃ amount of the Fe₂O₃/TiO₂@MIL-101 material for the photocatalytic degradation of ciprofloxacin.

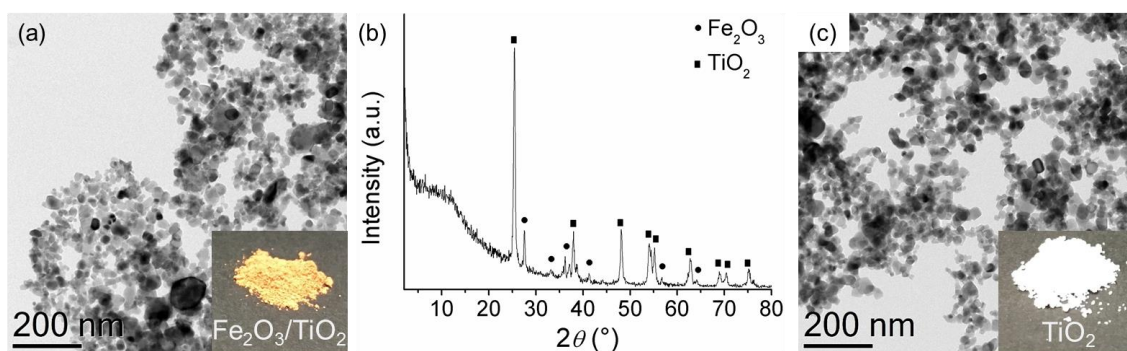


Figure S12. TEM and XRD analysis of $\text{Fe}_2\text{O}_3/\text{TiO}_2$ (a-b). TEM analysis of the commercial anatase TiO_2 (c).

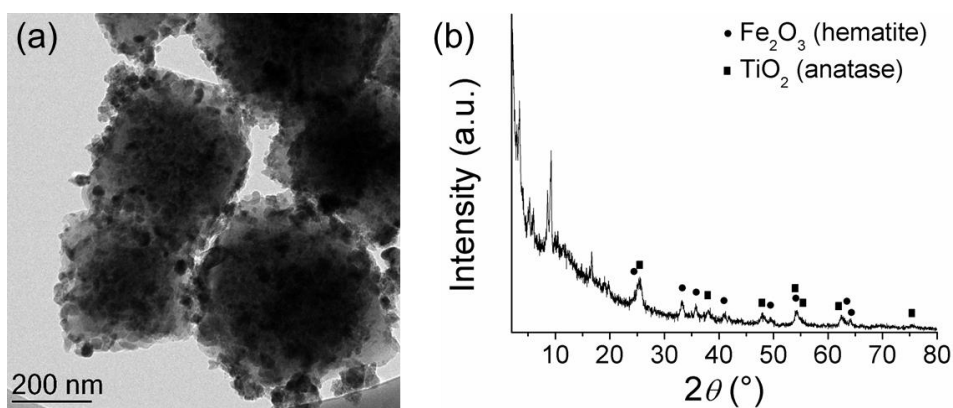


Figure S13. TEM micrograph of the $\text{Fe}_2\text{O}_3/\text{TiO}_2@\text{MIL-101}$ catalyst reused for the photocatalytic degradation of ciprofloxacin for five runs (a). XRD analysis of the reused catalyst (b).

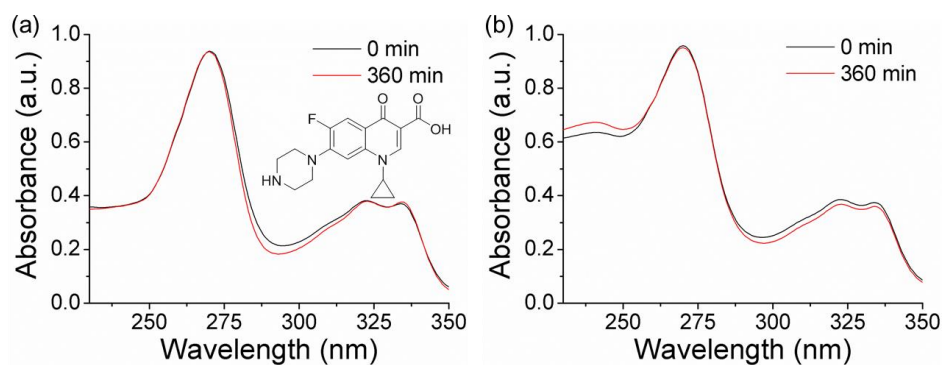


Figure S14. Stability of the ciprofloxacin concentration under visible light illumination in absence of catalyst (a) and in presence of catalyst without light (b).

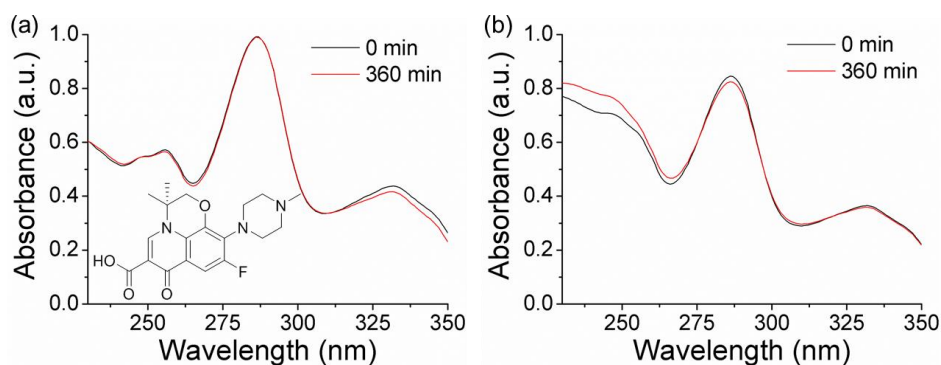


Figure S15. Stability of the levofloxacin concentration under visible light illumination in absence of catalyst (a) and in presence of catalyst without light (b).

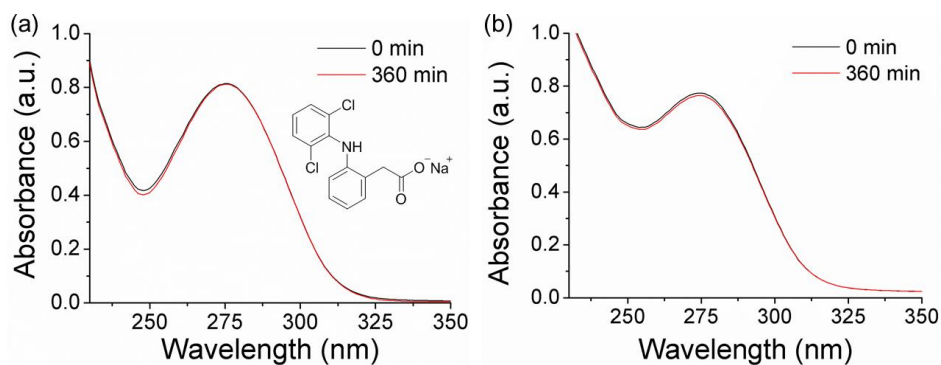


Figure S16. Stability of the diclofenac concentration under visible light illumination in absence of catalyst (a) and in presence of catalyst without light (b).

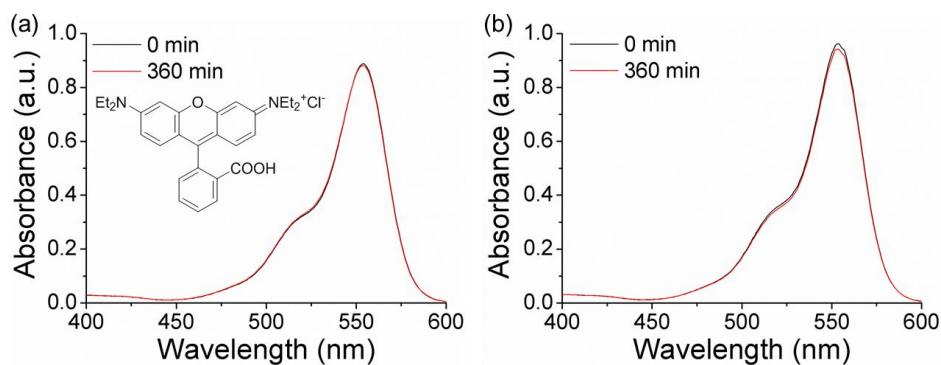


Figure S17. Stability of the rhodamine B concentration under visible light illumination in absence of catalyst (a) and in presence of catalyst without light (b).

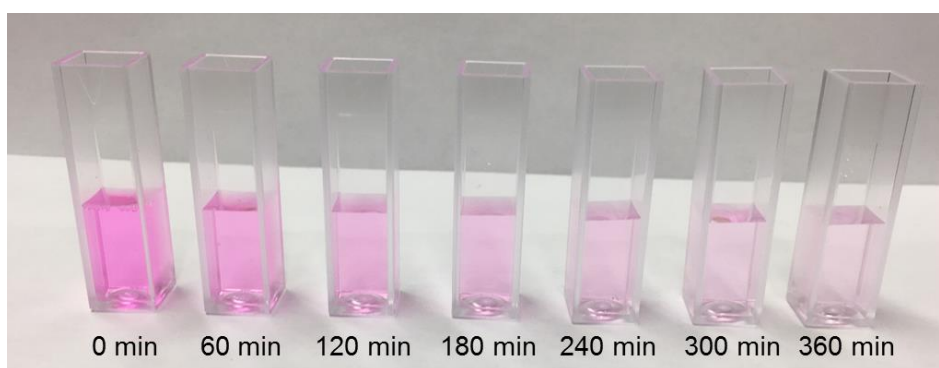


Figure S18. Time dependent samples of the rhodamine B solution during the photocatalytic degradation with $\text{Fe}_2\text{O}_3/\text{TiO}_2@\text{MIL-101}$.

References

- [S1] J. Hermannsdörfer, M. Friedrich, R. Kempe, *Chem. Eur. J.* **2013**, *19*, 13652–13657.
- [S2] D. Tilgner, R. Kempe, *Chem. Eur. J.* **2017**, *23*, 3184–3190.

8 List of Publications

The following publications were published, are submitted, or are to be submitted during the work on this thesis:

1. D. Tilgner, M. Friedrich, J. Hermannsdörfer, R. Kempe, *ChemCatChem* **2015**, *7*, 3916–3922.
“Titanium Dioxide Reinforced Metal-Organic Framework Pd Catalysts: Activity and Reusability Enhancement in Alcohol Dehydrogenation Reactions and Improved Photocatalytic Performance”
2. G. Hahn, J.-K. Ewert, C. Denner, D. Tilgner, R. Kempe, *ChemCatChem* **2016**, *8*, 2461–2465.
“A Reusable Mesoporous Nickel Nanocomposite Catalyst for the Selective Hydrogenation of Nitroarenes in the Presence of Sensitive Functional Groups”
3. D. Tilgner, R. Kempe, *Chem. Eur. J.* **2017**, *23*, 3184–3190.
“A Plasmonic Colloidal Photocatalyst Composed of a Metal–Organic Framework Core and a Gold/Anatase Shell for Visible- Light-Driven Wastewater Purification from Antibiotics and Hydrogen Evolution”
4. D. Tilgner, M. Friedrich, A. Verch, N. de Jonge, R. Kempe, to be submitted.
“Visible Light-Driven Hydrogen Generation from Alcohols for C-N Multiple Bond Formation by a Metal-Organic Framework-Based Noble Metal-Free Photocatalyst”
5. D. Tilgner, M. Friedrich, A. Verch, N. de Jonge, R. Kempe, submitted to *ChemPhotoChem*.
“A Metal-Organic Framework-Supported Nonprecious Metal Photocatalyst for Visible Light-Driven Wastewater Treatment”
Now this work is published as:
D. Tilgner, M. Friedrich, A. Verch, N. de Jonge, R. Kempe, *ChemPhotoChem* **2018**, *2*, 349–352.

9 Acknowledgements / Danksagung

9.1 Acknowledgements

I would like to thank my academic supervisor

Prof. Dr. Rhett Kempe

for the admission in his research group and for giving me the opportunity to work on this extremely interesting topic. I am grateful for his constant interest on the progress of this work, the great working conditions, and the liberties granted to me.

A special thanks goes to Martin Friedrich for the numerous scientific discussions, the HRTEM and the TGA measurements, the IT support, and for the great time in the lab. I appreciate the help of Dr. Wolfgang Milius and Florian Puchtler for the XRD measurements, Dr. Christine Denner for the SEM measurements, Dr. Jürgen Seidel for the XPS measurements, and the BayCeer institute for the ICP-OES measurements.

Special thanks to my students Konstantin Dieterle, Florian Pachel, Franziska Eger, Dominik Gränz, Anja Fickentscher, and Mara Klarner for their assistance in the laboratory.

I appreciate the great cooperation with Prof. Dr. Niels de Jonge and Dr. Andreas Verch. Thank you, for the scientific discussions and the extensive help regarding the electron microscopic material characterization.

A great thanks goes to Heidi Maisel, Simone Hoch, Sandra Keller, Anna-Maria Dietel, Christine Fell, and Marlies Schilling for their assistance and support in the daily laboratory life and to Dr. Torsten Irrgang for the proofreading of this thesis.

I appreciate the help of the employees of the central materials and consumables distribution, the electronics workshop, the metal workshop, and the glassblowing workshop for their excellent work.

I would like to thank the SFB 840 and the Bayreuth-Melbourne Colloid/Polymer Network for the financial support.

A warm thanks goes to my further lab colleges Dr. Justus Herrmannsdörfer, Dr. Adam Sobaczynski, Dr. Johannes Obenauf, Thomas Dietel, and Andreas Gollwitzer for the great time in the lab, their support and the wonderful working atmosphere. Moreover, I would like to thank my colleagues Dr. Sina Rösler, Dr. Susanne Ruch, Dr. Daniel Forberg, Dr. Sonja Fehn, Dr. Toni Hille, Dr. Muhammad Zaheer, Dr. Sadaf Qayyum, Dr. Awal Noor, Dr. Winfried Kretschmer, Stefan Schwarz, Gabriela Hahn, Tobias Schwob, Christoph Bäumler, Frederik Freitag, and Fabian Kallmeier, for the nice time in the last years.

My sincere thanks goes to my parents, my brother, Uschi, Hans, and Dirk for their support in every possible way, their love and motivation.

Last but not least, I am endlessly thankful to my Juli for her indescribable support and for her love.

9.2 Danksagung

Mein besonderer Dank gilt meinem akademischen Lehrer

Prof. Dr. Rhett Kempe

für die Aufnahme in seine Arbeitsgruppe und für die Möglichkeit, auf diesem sehr interessanten Forschungsgebiet zu arbeiten. Für sein permanentes Interesse am dem Vorschritt dieser Arbeit, die großartigen Arbeitsbedingungen und die mir gewährten Freiheiten bi ich sehr dankbar.

Besonderer Dank gilt Martin Friedrich für die zahlreichen wissenschaftlichen Diskussionen, HRTEM und TGA Messungen, der Unterstützung bezüglich IT-Fragen und der großartigen Zeit im Labor. Ich bin dankbar für die Hilfe von Dr. Wolfgang Milius und Florian Puchtler für XRD Messungen, Dr. Christine Denner für REM Messungen, Dr. Jürgen Seidel für XPS Messungen und dem BayCeer Institut für ICP-OES Messungen.

Besonderer Dank gilt meinen Studenten Konstantin Dieterle, Florian Pachel, Franziska Eger, Dominik Gränz, Anja Fickentscher und Mara Klarner für ihre unterstützende Arbeit im Labor.

Ich bin dankbar für die großartige Kooperation mit Prof. Dr. Niels de Jonge und Dr. Andreas Verch. Vielen Dank für die vielen wissenschaftlichen Diskussionen und die umfangreiche Hilfe bei der elektronenmikroskopischen Materialcharakterisierung.

Ein großer Dank gilt Heidi Maisel, Simone Hoch, Sandra Keller, Anna-Maria Dietel, Christine Fell und Marlies Schilling für ihre Unterstützung im täglichen Laborleben und Torsten Irrgang für das Korrekturlesen dieser Arbeit.

Ich bin dankbar für die Hilfe der Mitarbeiter der Chemikalienausgabe, der Elektronikwerkstatt, der Metallwerkstatt und der Glasbläserei für ihre exzellente Arbeit.

Ich möchte mich bei dem Sonderforschungsbereich SFB 840 und dem Bayreuth-Melbourne Colloid/Polymer Network für die finanzielle Unterstützung bedanken.

Ein großes Dankeschön geht an meine früheren Laborkollegen Dr. Justus Herrmannsdörfer, Dr. Adam Sobaczynski, Dr. Johannes Obenauf, Thomas Dietel und Andreas Gollwitzer für die großartige Zeit im Labor, ihre Unterstützung und die wunderbare Arbeitsatmosphäre. Des Weiteren möchte ich mich bei meinen Kollegen Dr. Sina Rösler, Dr. Susanne Ruch, Dr. Daniel Forberg, Dr. Sonja Fehn, Dr. Toni Hille, Dr. Muhammad Zaheer, Dr. Sadaf Qayyum, Dr. Awal Noor, Dr. Winfried Kretschmer, Stefan Schwarz, Gabriela Hahn, Tobias Schwob, Christoph Bäumler, Frederik Freitag und Fabian Kallmeier für die tolle Zeit in den letzten Jahren bedanken.

Mein aufrichtiger Dank gilt meinen Eltern, meinem Bruder, Uschi, Hans und Dirk für ihre Unterstützung in jedweder Weise, für ihre Liebe und Motivation.

Zuletzt bin ich meiner Juli unendlich dankbar für ihre unbeschreibliche Unterstützung und ihre Liebe.

.

10 (Eidesstattliche) Versicherungen und Erklärungen

(§ 8 Satz 2 Nr. 3 PromO Fakultät)

Hiermit versichere ich eidesstattlich, dass ich die Arbeit selbständig verfasst und keine anderen als die von mir angegebenen Quellen und Hilfsmittel benutzt habe (vgl. Art. 64 Abs. 1 Satz 6 BayHSchG).

(§ 8 Satz 2 Nr. 3 PromO Fakultät)

Hiermit erkläre ich, dass ich die Dissertation nicht bereits zur Erlangung eines akademischen Grades eingereicht habe und dass ich nicht bereits diese oder eine gleichartige Doktorprüfung endgültig nicht bestanden habe.

(§ 8 Satz 2 Nr. 4 PromO Fakultät)

Hiermit erkläre ich, dass ich Hilfe von gewerblichen Promotionsberatern bzw. –vermittlern oder ähnlichen Dienstleistern weder bisher in Anspruch genommen habe noch künftig in Anspruch nehmen werde.

(§ 8 Satz 2 Nr. 7 PromO Fakultät)

Hiermit erkläre ich mein Einverständnis, dass die elektronische Fassung der Dissertation unter Wahrung meiner Urheberrechte und des Datenschutzes einer gesonderten Überprüfung unterzogen werden kann.

(§ 8 Satz 2 Nr. 8 PromO Fakultät)

Hiermit erkläre ich mein Einverständnis, dass bei Verdacht wissenschaftlichen Fehlverhaltens Ermittlungen durch universitätsinterne Organe der wissenschaftlichen Selbstkontrolle stattfinden können.

Bayreuth, den 07.12.2017

Dominic Tilgner